



**National Library  
of Canada**

**Bibliothèque nationale  
du Canada**

**Canadian Theses Service**

**Service des thèses canadiennes**

**Ottawa, Canada  
K1A 0N4**

## **NOTICE**

**The quality of this microform is heavily dependent upon the quality of the original thesis submitted for microfilming. Every effort has been made to ensure the highest quality of reproduction possible.**

**If pages are missing, contact the university which granted the degree.**

**Some pages may have indistinct print especially if the original pages were typed with a poor typewriter ribbon or if the university sent us an inferior photocopy.**

**Reproduction in full or in part of this microform is governed by the Canadian Copyright Act, R.S.C. 1970, c. C-30, and subsequent amendments.**

## **AVIS**

**La qualité de cette microforme dépend grandement de la qualité de la thèse soumise au microfilmage. Nous avons tout fait pour assurer une qualité supérieure de reproduction.**

**S'il manque des pages, veuillez communiquer avec l'université qui a conféré le grade.**

**La qualité d'impression de certaines pages peut laisser à désirer, surtout si les pages originales ont été dactylographiées à l'aide d'un ruban usé ou si l'université nous a fait parvenir une photocopie de qualité inférieure.**

**La reproduction, même partielle, de cette microforme est soumise à la Loi canadienne sur le droit d'auteur, SAC 1970, c. C-30, et ses amendements subséquents.**

**THE UNIVERSITY OF ALBERTA**

**CONSTRUCTION OF A BROADBAND 10X10  
OPTOELECTRONIC SWITCHING MATRIX**

**BY**

**MARC VILLEUX**



**A THESIS**

**SUBMITTED TO THE FACULTY OF GRADUATE STUDIES AND RESEARCH IN  
PARTIAL FULFILLMENT OF THE REQUIREMENTS FOR THE DEGREE OF  
MASTER OF SCIENCE.**

**DEPARTMENT OF ELECTRICAL ENGINEERING**

**EDMONTON, ALBERTA**

**FALL, 1990**



**National Library  
of Canada**

**Bibliothèque nationale  
du Canada**

**Canadian Theses Service    Service des thèses canadiennes**

**Ottawa, Canada  
K1A 0N4**

**The author has granted an irrevocable non-exclusive licence allowing the National Library of Canada to reproduce, loan, distribute or sell copies of his/her thesis by any means and in any form or format, making this thesis available to interested persons.**

**The author retains ownership of the copyright in his/her thesis. Neither the thesis nor substantial extracts from it may be printed or otherwise reproduced without his/her permission.**

**L'auteur a accordé une licence irrévocable et non exclusive permettant à la Bibliothèque nationale du Canada de reproduire, prêter, distribuer ou vendre des copies de sa thèse de quelque manière et sous quelque forme que ce soit pour mettre des exemplaires de cette thèse à la disposition des personnes intéressées.**

**L'auteur conserve la propriété du droit d'auteur qui protège sa thèse. Ni la thèse ni des extraits substantiels de celle-ci ne doivent être imprimés ou autrement reproduits sans son autorisation.**

**ISBN 0-315-64947-X**

**THE UNIVERSITY OF ALBERTA  
RELEASE FORM**

**NAME OF AUTHOR: MARC VILLEUX**

**TITLE OF THESIS: CONSTRUCTION OF A BROADBAND 10X10  
OPTOELECTRONIC SWITCHING MATRIX**

**DEGREE: MASTER OF SCIENCE**

**YEAR THIS DEGREE GRANTED: 1990**

Permission is hereby granted to THE UNIVERSITY OF ALBERTA LIBRARY to reproduce single copies of this thesis and to lend or sell such copies for private, scholarly, or scientific research purposes only.

The author reserves other publication rights, and neither the thesis nor extensive extracts from it may be printed or otherwise reproduced without the author's written permission.

  
\_\_\_\_\_  
Marc Veilleux

2, 8730 Whyte Avenue

Edmonton, Alberta

T6C 0Z1

Sept. 11<sup>th</sup> 1990  
Date


**"Ce que les hommes veulent en fait, ce n'est pas la connaissance, c'est la certitude."**


**-Bertrand Russell**

**THE UNIVERSITY OF ALBERTA  
FACULTY OF GRADUATE STUDIES AND RESEARCH**

The undersigned certify that they have read, and recommend to the Faculty of Graduate Studies and Research for acceptance, a thesis entitled Construction of a Broadband 10X10 Optoelectronic Switching Matrix by Marc Velleux in partial fulfillment of the requirements for the degree of Master of Science.

  
\_\_\_\_\_  
Dr. R.I. MacDonald, Supervisor

  
\_\_\_\_\_  
Dr. J.M. McMullin

  
\_\_\_\_\_  
Dr. F. Welchman

10/19/90  
\_\_\_\_\_  
Date

## ABSTRACT

The goal of this project was to develop an optoelectronic switching matrix of dimension 10X10, designed for a bandwidth per channel greater than 1 GHz, isolation greater than 60 dB, throughput loss of 0 dB and a large signal to noise ratio (>30 dB in a 1 GHz bandwidth). Such a switching matrix will have unique capabilities, with applications in computing and signal processing as well as communications. The project required the development of new GaAs optoelectronic photoconductor switches, integration of both optical and electronic components, and the development of transmitter and receiver arrays. The functional modules forming the matrix were built and successfully demonstrated but severe packaging difficulties delayed their integration into a complete working unit.

## **REMERCIEMENTS**

**Je voudrais tout d'abord prendre cette occasion pour sincèrement remercier le docteur R.I. MacDonald pour avoir eu confiance en moi et au projet tout au long du laborieux cheminement qui a mené à la conclusion de ma maîtrise. Son enthousiasme et son honnêteté intellectuelle furent pour moi des constantes sources d'inspiration. J'aimerais également remercier les autres membres de mon comité d'évaluation, les docteurs J.N. McMullin et F. Weichman, ainsi que G. Fraser pour avoir accepté de lire ma thèse et d'y apporter des améliorations. De plus, j'aimerais exprimer ma gratitude envers le docteur G. Cormack qui m'a convaincu, il y a déjà 3 ans de cela, de me lancer tête première dans l'aventure du ATRC.**

**Un projet de maîtrise ne se réalise jamais sans l'appui moral et technique de plusieurs personnes. Je suis tout particulièrement reconnaissant à George Fraser et Darrell Barabesh pour leurs suggestions et leur encouragement constant. De plus j'aimerais remercier mes confrères étudiants du ATRC pour leur solidarité tout au long de mon séjour au centre de recherche. Je suis grandement redevable à Kevin Jacobson pour les nombreuses heures de discussions (techniques et non-techniques) que nous avons eues, et à Richard Kusyk pour ses talents en informatique et son sens de l'humour "Monty Pythonnesque".**

**Par ailleurs, je voudrais remercier le ATRC et l'université de l'Alberta pour leur aide financière lors des deux premières années de ma maîtrise. La conclusion de mon projet fut rendue possible par le soutien financier du docteur R.I. MacDonald et je lui en suis reconnaissant.**



La réalisation de ce projet fut grandement facilitée par l'aide exceptionnelle d'un groupe de gens travaillant à l'extérieur du ATRC. Il s'agit de Herb Gans et de son équipe à l'université de l'Alberta, ainsi que de Graham McKinnon et de Yan Loke du AMC. Sans leur précieuse collaboration, le projet n'aurait jamais abouti.

Les photodétecteurs utilisés dans ce projet furent fabriqués au CRC à Ottawa dans le cadre d'une entente de collaboration entre le ATRC et le département des communications. Plusieurs membres du personnel du CRC, dont plus particulièrement J. Noad et F. Gouin, furent impliqués dans ce projet et leur participation fut des plus pertinentes.

En tout dernier lieu, j'aimerais offrir cette thèse à mes parents. Leur support discret mais constant tout au long de mes études fut pour moi une source d'inspiration qui m'a permis de franchir bien des difficultés.

## TABLE OF CONTENTS

CHAPTER	PAGE
<b>1 INTRODUCTION</b>	<b>1</b>
<b>1.1 SWITCHING MATRICES</b>	<b>1</b>
<b>1.2 PRINCIPLES OF OPERATION OF AN OPTOELECTRONIC SWITCH</b>	<b>2</b>
<b>1.3 APPLICATIONS OF AN OE SWITCHING MATRIX</b>	<b>5</b>
1.3.1 Communications Switching	5
1.3.2 Delay Line Processors	6
1.3.3 Look-up table for residue arithmetic	7
1.3.4 Optoelectronic Neural Networks	9
1.3.5 Optoelectronic Maser Arrays	11
<b>1.4 PROJECT GOALS</b>	<b>11</b>
<b>2 TRANSMITTER MODULE</b>	<b>14</b>
<b>2.1 OPTICAL SOURCES</b>	<b>14</b>
2.1.1 Design considerations	14
2.1.2 Mitsubishi ML60X1 laser family	17
<b>2.2 BIASING CIRCUIT</b>	<b>22</b>
<b>2.3 TRANSMITTER HOUSING</b>	<b>27</b>
<b>3 OPTOELECTRONIC CROSSPOINTS (SWITCHING MODULE)</b>	<b>31</b>
<b>3.1 CROSSPOINT REQUIREMENTS</b>	<b>31</b>
<b>3.2 CROSSPOINT SELECTION</b>	<b>32</b>
3.2.1 Homojunction crosspoints	32
3.2.2 Heterojunction crosspoints	33
3.2.3 Metal-Semiconductor-Metal Photodetectors	34
3.2.4 Photoconductors	37
<b>3.3 PERFORMANCE OF SURFACE DEPLETED PHOTOCONDUCTORS</b>	<b>43</b>
3.3.1 Bandwidth	43
3.3.2 Responsivity	49
3.3.3 Isolation	51
3.3.4 Noise	52
3.3.5 Conclusion	56
<b>4 OPTICAL POWER DISTRIBUTION MODULE</b>	<b>57</b>
<b>4.1 TYPES OF OPTICAL DIVISION</b>	<b>57</b>
<b>4.2 SPECKLE NOISE</b>	<b>59</b>
<b>4.3 MECHANICAL ASSEMBLY</b>	<b>61</b>
<b>5 RECEIVER MODULE</b>	<b>66</b>
<b>5.1 RECEIVER REQUIREMENTS</b>	<b>66</b>
<b>5.2 RECEIVER LAYOUT</b>	<b>69</b>
<b>5.3 RECEIVER PERFORMANCE</b>	<b>78</b>
<b>5.4 RECEIVER HOUSING</b>	<b>84</b>
<b>6 INTEGRATION OF THE FUNCTIONAL MODULES</b>	<b>86</b>
<b>6.1 HOUSING OF THE FUNCTIONAL MODULES</b>	<b>86</b>
<b>6.2 MODIFICATIONS TO THE RECEIVERS</b>	<b>88</b>
<b>6.3 PERFORMANCE OF A COMPLETE 10X1 RECEIVER</b>	<b>93</b>
<b>6.4 PREMATURE BREAKDOWN OF OE RECEIVERS</b>	<b>100</b>

<b>CHAPTER</b>		<b>PAGE</b>
<b>REFERENCES</b>		<b>107</b>
<b>APPENDIX A</b>	<b>COMPONENT SELECTION FOR LASER BIAS CIRCUIT</b>	<b>112</b>
<b>APPENDIX B</b>	<b>SI V-GROOVE FABRICATION STEPS</b>	<b>114</b>
<b>APPENDIX C</b>	<b>RECEIVER SIMULATION MODEL</b>	<b>116</b>
<b>APPENDIX D</b>	<b>DRAWINGS</b>	<b>118</b>
<b>APPENDIX E</b>	<b>PRINTED CIRCUIT BOARDS</b>	<b>133</b>
<b>APPENDIX F</b>	<b>DEVICE DATA SHEETS</b>	<b>137</b>

## LIST OF FIGURES

FIGURES	PAGE
Figure 1.1	1
Figure 1.2	3
Figure 1.3	7
Figure 1.4	8
Figure 1.5	10
Figure 1.6	12
Figure 2.1	14
Figure 2.2	18
Figure 2.3	19
Figure 2.3	20
Figure 2.4	20
Figure 2.5	22
Figure 2.6	23
Figure 2.7	24
Figure 2.8	26
Figure 2.9	26
Figure 2.10	27
Figure 2.11	28
Figure 2.12	29
Figure 3.1	36

<b>FIGURES</b>	<b>PAGE</b>
Figure 3.2 Photoconductive detector (PC) .....	39
Figure 3.3 Interdigitated Photoconductor .....	41
Figure 3.4 Monolithically integrated Photoconductors.....	42
Figure 3.5 Frequency response of an array crosspoint for different optical power levels .....	44
Figure 3.6 DC photocurrent against optical power level for different finger spacings.....	45
Figure 3.7 Current amplitude against optical power level at 3 different frequencies (DC, 10 MHz, 100 MHz) .....	48
Figure 3.8 Crosspoint responsivity versus optical power level at 3 different frequencies (DC, 10 MHz, 100 MHz).....	49
Figure 3.9 Responsivity versus applied bias for a 5 $\mu\text{m}$ channel length photoconductor at 3 different frequencies (DC, 10 MHz, 100 MHz).....	50
Figure 3.10 Isolation levels for different biases .....	52
Figure 3.11 Photoconductor noise equivalent circuit.....	53
Figure 3.12 Photoconductor total noise power for a 5 $\mu\text{m}$ array crosspoint at an optical power level of 0.4 mW.....	55
Figure 4.1 Noise peaks due to the reflections back into the waveguide at the fibre-detector interface.....	61
Figure 4.2 Biconical-taper star couplers mounted on a card .....	62
Figure 4.3 (a) Etched grooves in a silicon wafer .....	63
Figure 4.3 (b) Schematic of the fibre's position in a groove.....	64
Figure 4.4 V-groove alignment set-up .....	64
Figure 5.1 Photoconductor response using a splitter output at different bias voltages.....	68
Figure 5.2 Receiver block diagram.....	68
Figure 5.3 (a) Receiver circuit.....	70
Figure 5.3 (b) Receiver printed circuit board .....	70
Figure 5.4 Photoconductor chip mounted on board.....	71
Figure 5.5 Photoconductor biasing circuit for grounded off-state.....	72

Figure 5.6	Simulated response of the S21 parameter of the amplifier & equalizer module's functional blocks terminated in a 50 $\Omega$ load driven by a flat broadband current source.....	74
Figure 5.7	Final OE line receiver .....	78
Figure 5.8	Frequency response of an OE matrix channel with only one crosspoint illuminated.....	79
Figure 5.9	Receiver response with one crosspoint illuminated measured at two different moments in time .....	80
Figure 5.10	Receiver noise with one crosspoint illuminated as measured in a 100 kHz bandwidth .....	81
Figure 5.11	Receiver's SNR with one crosspoint illuminated .....	82
Figure 5.12	Receiver frequency response with one crosspoint illuminated by different incident optical power levels.....	84
Figure 5.13	Two receivers mounted on a receiver card.....	85
Figure 6.1	Housing rack for an OE switching matrix.....	86
Figure 6.2	Receiver box with the U shaped bracket .....	87
Figure 6.3	(a) Receiver frequency response with 10 fibres mounted .....	88
Figure 6.3	(b) Receiver frequency response with only one fibre mounted.....	89
Figure 6.4	Simulated response of the amplifier & equalizer module driven by a flat broadband current source and considering the photoconductor's dynamic resistance .....	90
Figure 6.5	(a) Simulated response of the modified amplifier & equalizer module driven by a flat broadband current source and considering the photoconductor's dynamic resistance.....	91
Figure 6.5	(b) Crosspoint frequency response illuminated with one output from a biconal-taper power splitter .....	92
Figure 6.5	(c) Receiver frequency response using the modified amplifier & equalizer module. 8 crosspoints are illuminated .....	92
Figure 6.6	Frequency response of a complete 10X1 receiver with all the crosspoints illuminated.....	93
Figure 6.7	Optical crosstalk measurement between adjacent crosspoints.....	95
Figure 6.8	Crosstalk measurement between adjacent receivers .....	95

<b>FIGURES</b>	<b>PAGE</b>
<b>Figure 6.9</b>	<b>Receiver noise level..... 97</b>
<b>Figure 6.10</b>	<b>Receiver response to a 10 kHz pulsed bias..... 98</b>
<b>Figure 6.11</b>	<b>Arithmetic functions generated by the receiver ..... 99</b>
<b>Figure 6.12</b>	<b>Receiver response with a non depleted photoconductor..... 101</b>
<b>Figure A.1</b>	<b>Transmitter biasing circuit..... 112</b>
<b>Figure B.1</b>	<b>Fabrication steps of Si V-grooves ..... 115</b>
<b>Figure C.1</b>	<b>Model circuit for receiver simulations..... 116</b>
<b>Figure D.1</b>	<b>OE Switch Receiver Assembly Mechanical Design..... 119</b>
<b>Figure D.2</b>	<b>OE Switch Receiver Box Mechanical Design ..... 120</b>
<b>Figure D.3</b>	<b>OE Switch Receiver Box Mechanical Design ..... 121</b>
<b>Figure D.4</b>	<b>OE Switch Receiver Box..... 122</b>
<b>Figure D.5</b>	<b>OE Switch Receiver Box Shielding Wall ..... 123</b>
<b>Figure D.6</b>	<b>OE Switch Receiver Box Top Lids ..... 124</b>
<b>Figure D.7</b>	<b>OE Switch Receiver Bottom Lid..... 125</b>
<b>Figure D.8</b>	<b>OE Switch Receiver Box Rails..... 126</b>
<b>Figure D.9</b>	<b>OE Switch Receiver Box Fibre Support Bar ..... 127</b>
<b>Figure D.10</b>	<b>OE Switch Receiver Fibre Support Bracket..... 128</b>
<b>Figure D.11</b>	<b>OE Switch Receiver Motherboard..... 129</b>
<b>Figure D.12</b>	<b>OE Switch Receiver Backplane Layout..... 130</b>
<b>Figure D.13</b>	<b>OE Switch Rack Layout..... 131</b>
<b>Figure D.14</b>	<b>OE Switch Rack Layout..... 132</b>
<b>Figure E.1</b>	<b>Receiver printed circuit board..... 133</b>
<b>Figure E.2</b>	<b>Receiver module printed circuit board ..... 134</b>
<b>Figure E.3</b>	<b>Transmitter module printed circuit board (front plane)..... 135</b>
<b>Figure E.4</b>	<b>Transmitter module printed circuit board (back plane) ..... 136</b>

## LIST OF ABBREVIATIONS

ABBREVIATION	DESCRIPTION
AC.....	Alternating Current
AGC.....	Automatic Gain Control
AMC.....	Alberta Microelectronic Centre
APD .....	Avalanche PhotoDiode
ATRC .....	Alberta Telecommunications Research Centre
BER .....	Bit Error Rate
BW.....	Bandwidth
CRC.....	Communications Research Centre
CW.....	Continuous Wave
DC .....	Direct Current
DEMUX.....	Demultiplexer
DOC.....	Department of Communications
EM .....	Electromagnetic
Eq. Range.....	Equalization Range
FET.....	Field Effect Transistor
Fon .....	Roll on Frequency
GC.....	1 dB gain compression
LED.....	Light Emitting Diode
MESFET .....	Metal-Semiconductor Field Effect Transistor
MMIC.....	Monolithic Microwave Integrated Circuit
MSM .....	Metal-Semiconductor-Metal
MUX.....	Multiplexer
NF.....	Noise figure
OE .....	Optoelectronic



<b>ABBREVIATION</b>	<b>DESCRIPTION</b>
<b>OP AMP</b> .....	<b>Operational amplifier</b>
<b>PC</b> .....	<b>Photoconductor</b>
<b>Q</b> .....	<b>Quality Factor</b>
<b>RF</b> .....	<b>Radio frequency</b>
<b>ROSM</b> .....	<b>Reflex Optoelectronic Switch Matrix</b>
<b>TTL</b> .....	<b>Transistor-Transistor-Logic</b>
<b>SNR</b> .....	<b>Signal to Noise Ratio</b>
<b>UV</b> .....	<b>Ultraviolet</b>
<b>VLSI</b> .....	<b>Very Large Scale Integration</b>

## LIST OF SYMBOLS

SYMBOL	DESCRIPTION
$A$ .....	Detector's photosensitive area
$B$ .....	Bandwidth
$c$ .....	Speed of light
$C$ .....	Capacitance
$F_{\phi}$ .....	Photon flux density
$g$ .....	Amplifier gain
$G$ .....	Conductance
$G_d$ .....	Photoconductor's dark conductance
$G_p$ .....	Photoconductor's photo-induced conductance
$h$ .....	Planck's constant
$I$ .....	Current
$I_{amp}$ .....	Receiver noise current
$I_{DC}$ .....	Photoconductor DC current
$I_{GN}$ .....	Shot noise current
$I_A$ .....	Set of signals in neural networks
$I_J$ .....	Johnson noise current
$I_{LASER}$ .....	DC laser current in laser driver
$I_{FC}$ .....	Photoconductor AC current
$I_t$ .....	Total noise current
$I_{th}$ .....	Laser threshold current
$J$ .....	Current density
$J_{th}$ .....	Threshold current density
$k$ .....	Boltzmann's constant
$L$ .....	Inductance

SYMBOL	DESCRIPTION
$m$ .....	Modulation depth
$M$ .....	Average number of times a hole is trapped
$m^*$ .....	Effective mass
$M_c(\tau)$ .....	Excess noise factor
$N_d$ .....	Donor density
$P_{o1}$ .....	Electrical power drive level
$P_o$ .....	DC optical power
$q$ .....	Electronic charge
$R$ .....	Resistance
$R$ .....	Responsivity
$R_c$ .....	Specific contact resistance
$R_L$ .....	Load resistance
$R_t$ .....	Maximum bit rate
$R_{VAR}$ .....	Laser driver's variable resistor
$S_{ij}$ .....	Scattering parameters
$S_o$ .....	Noise optical power
$T$ .....	Absolute ambient temperature
$T_o$ .....	Threshold temperature coefficient
$t_r$ .....	Rise time
$T_r$ .....	Electron transit time
$V$ .....	Voltage
$V^*$ .....	Reference voltage of laser driver
$V_{BIAS}$ .....	Photodiode voltage of laser driver
$V_j$ .....	Neural state
$V_{sig}$ .....	Signal drive level
$V_{OPAMP}$ .....	OP AMP voltage of laser driver
$w_{ij}$ .....	Interaction matrix

<b>SYMBOL</b>	<b>DESCRIPTION</b>
$Z_0$ .....	Reference impedance
$\beta$ .....	Feedback reverse transmission factor
$\Gamma_{out}$ .....	Output reflection coefficient
$\Gamma_s$ .....	Source reflection coefficient
$\epsilon_0$ .....	Permittivity in vacuum
$\epsilon_s$ .....	Semiconductor permittivity
$\eta$ .....	Quantum efficiency
$\mu_0$ .....	Permeability in vacuum
$\tau$ .....	Mean hole lifetime
$\tau_t$ .....	Lifetime due to trapping
$\phi_{Bn}$ .....	Schottky barrier height
$\omega$ .....	Signal angular frequency

**CHAPTER 1**  
**INTRODUCTION**

**1.1 SWITCHING MATRICES**

In a switching matrix, two sets of orthogonal lines meet at crosspoints where connections can be made or broken at will. The first set of lines represents the accessible channel input lines while the second set represents the subscriber output lines as illustrated in figure 1.1 . The switching operation can be accomplished in many ways.

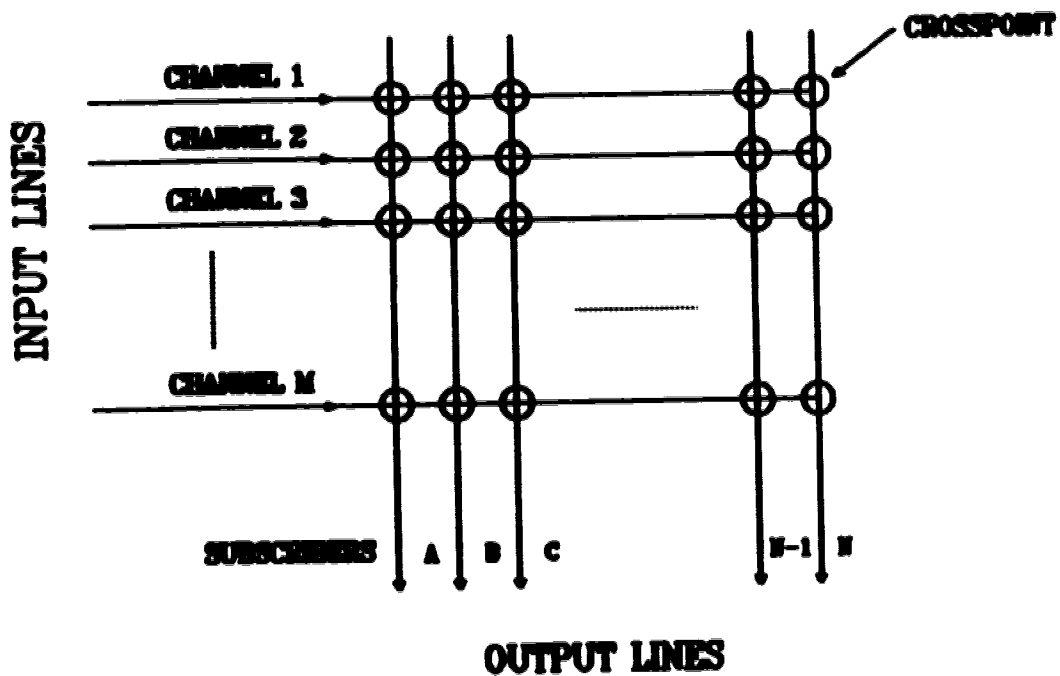


**Figure 1.1 Switching Matrix.**

Electronic switching is currently used in systems that operate at frequencies in the hundreds of MHz. However, the development of very high

speed data transmission and broadband services places a requirement for switching signals of considerably higher frequencies. Electronic techniques are being developed for this capability and an integrated unit suitable for digital signals up to 2.6 Gbits/s was recently announced [1]. At high frequencies, electromagnetic coupling can arise among each set of lines and through the crosspoints. Methods such as photonic switching may become competitive at those frequencies.

In the past few years, optical switching has been extensively investigated as an alternative for high frequency signals because of the excellent signal confinement it offers. Electro-optic switches made of LiNbO<sub>3</sub>, optical-directional-couplers, where the light is directed from the input to the appropriate output, offer a good isolation and very low losses for small systems. However, at present, there are severe problems in making practical optical matrix switches of a large size (i.e. > 16X16) [2].

A hybrid of optical and electronic switching was proposed in the late 1970's [3]. This hybrid switching matrix takes advantage of the light confinement in optical paths to achieve low crosstalk levels while retaining many advantages of the mature electronics technology. In this switching technique, the input signal to the switching element is optical while the output provided from the crosspoint is electrical, thus the term optoelectronic (OE) is used to denote the operation of the switch.

## **1.2 PRINCIPLES OF OPERATION OF AN OPTOELECTRONIC SWITCH**

In an optoelectronic switching matrix, the information signal is distributed in the form of light to the various crosspoints by means of passive optical distribution devices. There, the information signal is switched by means of photodetectors which generate electrical signals at their output and whose

sensitivity to light is turned on and off [4]. It is noteworthy that only the information signal is switched and not the carrier, in contrast to the function of an optical switching matrix. The optoelectronic conversion enables the handling of the electrical information signals, after switching, by means of conventional broadband electronic devices. Several optoelectronic (OE) switches with different performances have been demonstrated in the past few years. In 1985, MacDonald and Lam built a 3X3 OE switch that had a 1 GHz bandwidth and over 50 dB of isolation [5]. More recently, Forrest *et al* successfully constructed an 8X8 matrix that handles a data throughput rate of 200 Mbit/s and has a reconfiguration time in the order of 100 ns [6].

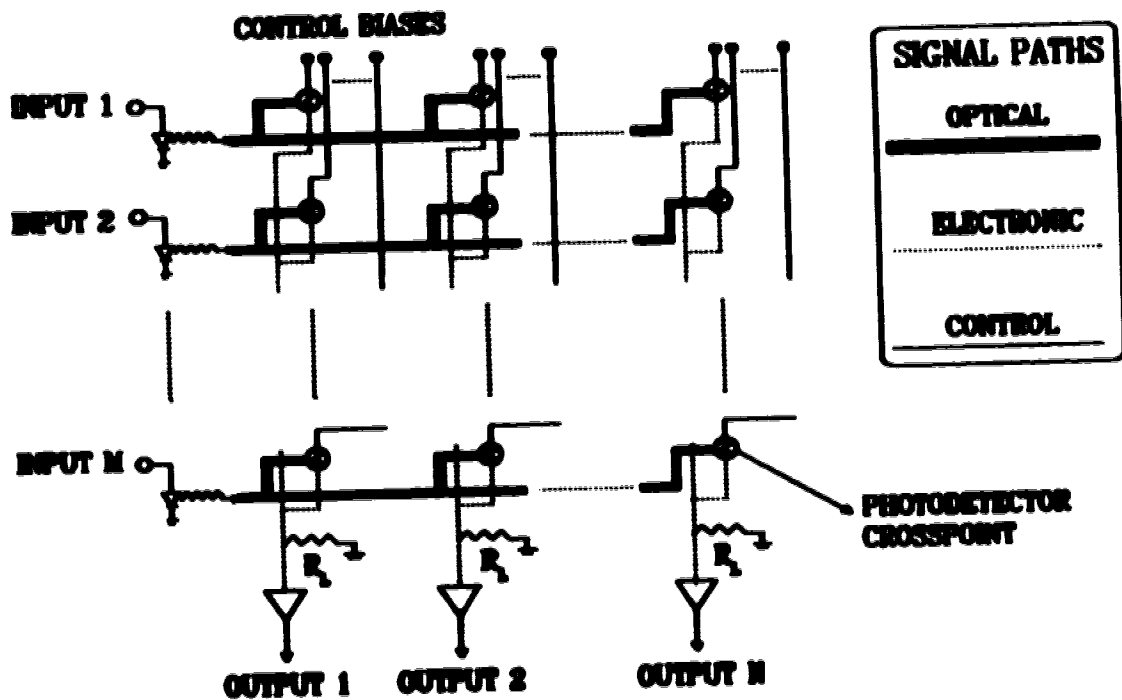


Figure 1.2 Schematic diagram of an Optoelectronic switch matrix.

An optoelectronic switching matrix is shown schematically in figure 1.2 . The information signal to be switched is impressed on an optical carrier by means of current modulation of a laser or of a Light Emitting Diode (LED). The intensity modulated light is then distributed to the "n" crosspoints through passive optical waveguides which have low crosstalk levels. At the crosspoints, the switching function is accomplished, as described above, by rendering the photodetectors sensitive or insensitive. The electrical signals generated at the output of the detectors dedicated to a single subscriber channel are then summed. This summation can be easily achieved if photoconductors or Metal-Semiconductor-Metal (MSM) photodiodes are used as crosspoints, by connecting to a common point one terminal of each of the crosspoints assigned to a specific output. The summation can thus be realized as an integrated function of a monolithic array of photodetectors [7]. It is noteworthy that from the switching point of view the optoelectronic switch can be viewed as a black box with electrical inputs and outputs, where the use of an optical carrier is internal to the matrix. This arrangement seems amenable to extensive integration [8] using both integrated optics and integrated electronic techniques that are already well developed.

Since the detectors are the only active switching elements of the optoelectronic matrix, the noise and isolation properties of the matrix will be determined by the immunity to noise and the isolation of the photodetectors as well as the isolation of the output lines [5]. The isolation between the input and output lines is essentially infinite. Light can couple into the electrical lines only through the photodetectors. The isolation of the photodetectors therefore determines the input/output crosstalk. The only leakage that can occur at the photodetectors is due to residual photoresponse in the off-state. Such photoresponse depends on the photodetecting device used. With most



semiconductor photodetectors, it can be less than the leakage measured in other types of photonic switching matrices proposed up to now.

There exists also the possibility of coupling between the outputs of the photodetectors. The output signal lines are electrical and, at high frequencies, electromagnetic effects can be important. Because the output lines are interconnected only by optical paths, this problem can be solved by physically isolating the crosspoints. Such a solution would reduce the possibility of integration of the elements, and thus a trade-off has to be made between isolation performance and integration [9].

### **1.3 APPLICATIONS OF AN OE SWITCHING MATRIX**

#### **1.3.1 Communications Switching**

The simplicity, the reliability and the small size achieved by integrated optoelectronic fabrication techniques make the optoelectronic matrix quite attractive for many applications [10]. The most obvious one is unequivocally the centrally switched distribution of signals where the signal paths between the inputs and the outputs are completed as requested.

MacDonald [5] and Tangonan [8] have demonstrated that the crosspoints used in an OE matrix enjoy sufficient speed and isolation to form non-blocking matrix units that could perform the switching of analog as well as digital signals. This results in the possibility of routing high data rate signals as well as FM or wideband video signals [11].

The maximum possible size of the matrix unit is determined by the amount of optical power required at the crosspoints to achieve the desired performance, i.e. Signal to Noise Ratio (SNR) or Bit Error Rate (BER), as well as the total emission of light by the emitter. The matrix units can also be assembled together to result in large scale matrix switches that could perform, for example, the

interconnection of computers for parallel processing of digital signals [12] where the units are essentially Multiplexers (MUX) and Demultiplexers (DEMUX).

### 1.3.2 Delay Line Processors

Many signal processing functions, including coded sequence generation, convolution, correlation, matrix-vector multiplication and frequency filtering [13,14], can be accomplished with the optoelectronic switch matrix by making delayed connections between the outputs and the inputs to form what has been called a Reflex Optoelectronic Switch Matrix (ROSM) as shown in figure 1.3 [15,16]. In this case, all the outputs but one are fed back to the same number of inputs via delay lines of differing lengths. In an  $N \times N$  crosspoint matrix,  $2^{N-1}$  different delays can be obtained if  $N-1$  connections of different lengths are made. These delays can be selected either in parallel or in series and can be made electrically or optically depending on whether the location in the matrix that is chosen to implement them is before or after the laser transmitters. Optical delays offer better precision and stability, insensitivity to electromagnetic interference and wideband operation [17]. The utilization of optical fibre delay paths in an OE matrix as part of the signal distribution network thus allows for wideband, precise and rapidly selectable delays which could be used by subsequent phase sensitive stages as, for example, a phased array antenna [10,18].

One unique feature of the ROSM is the directionality which is imposed by the optical-to-electronic conversion at the crosspoints. This directionality permits regeneration of the signal in the loops so that a ring resonator can be constructed [19]. Ring resonators can be combined in parallel to create complex comb filters which can be tuned rapidly if the loop lengths can be quickly altered by means of fast crosspoints. Ring resonators obtained by the ROSM are hybrid devices employing electronic stages which correspond to repeater stages.

Optoelectronic conversion in the loop degrades its dynamic range and noise performance. On the other hand, these repeater stages give control over the loop loss and thus over the quality factor ( $Q$ ) of the filter [15].

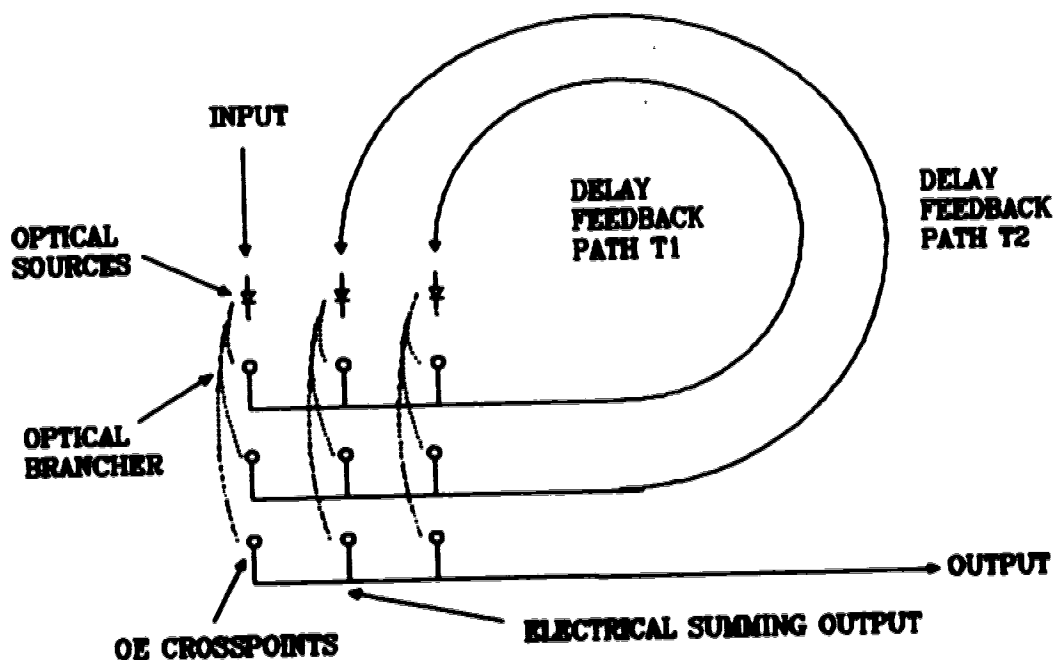


Figure 1.3 3X3 Reflex Optoelectronic Switch Matrix (ROSM).

Lam et al., in [15], have obtained experimentally, using a ROSM, a tunable comb filter with a filter envelope extending to 1 GHz, with a  $Q$  value of 300 and a dynamic range of 25 dB.

### 1.3.3 Look-up table for residue arithmetic

Arithmetic in residue number systems does not involve carries. Operations such as sums or products can therefore be obtained rapidly by means of look-up tables of prestored answers for each digit [20]. The required look-up table for residue processing is fundamentally an array of "AND" gates that identify signals

from two orthogonal position-coded inputs. Along one axis of the array, the outputs of these gates are connected to multiple-input "OR" units that generate a position-coded output [21].

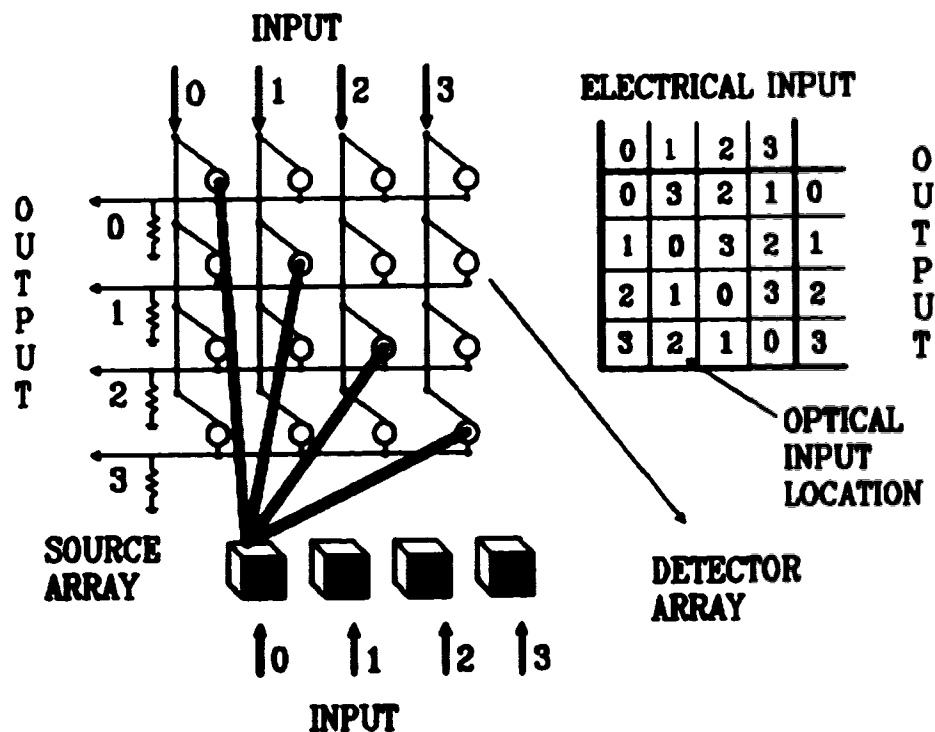


**Figure 1.4** Optoelectronic look-up table. The detector array receives one input in the form of a bias on one of the position-coded wires lying in the y direction. The position-coded wires in the orthogonal direction are the output lines. Therefore only the x axis of the array is labeled input. The other input to the array comes from the one-dimensional array of sources. The entries in the table indicate which source is associated with the detector at each location.

This arithmetic can be easily achieved by means of a particular and specific configuration of an OE switching matrix where the light from the transmitters is position-coded [21]. The look-up table as well as the particular matrix configuration are shown in figure 1.4. The crosspoints in the OE matrix play the

role of the "AND" gates whose two orthogonal position-coded inputs are the light from a transmitter and the photodetector bias. The "OR" function is naturally accomplished by the current summation in the detector array of the OE matrix. The entries in the table found in figure 1.4 indicate which source is associated with the detector at each location.

While optical residue processing will not be discussed extensively in this thesis, it is noted that there is an alternative to the optical position coded inputs originally proposed for optoelectronic residue processing. The standard OE matrix configuration shown in figure 1.2 can be used in conjunction with a controller that generates the required biasing voltage to each individual crosspoint. In this form, the optical inputs and electrical inputs are respectively represented as a column and a diagonal in the matrix. The main advantage of this proposal is that no special configuration of the matrix is required for this particular application. However, the speed of the look-up table is determined by the speed at which the crosspoints associated to the appropriate matrix diagonal can be biased by the controller.

#### 1.3.4 Optoelectronic Neural Networks

The vector product

$$I_i = \sum_j w_{ij} V_j$$

equation 1.1

required in a neural network can be performed by an OE switching matrix as shown in figure 1.5. In an OE switching matrix, the on-state crosspoint switches generate electrical signals that are combined at the output lines, thus providing the required vector product to compose a new set of signals  $I_i$  which forms the input to a learning process that updates the state of the original signal set.

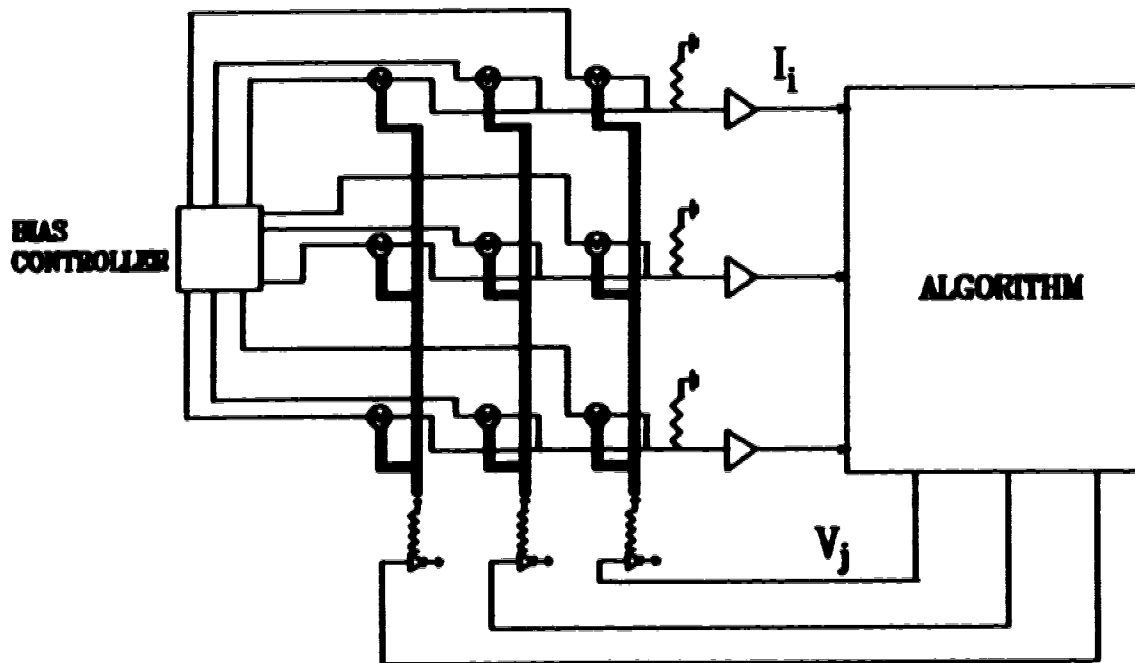


Figure 1.5 3x3 Optoelectronic Neural Network.

The neural state  $V_j$  is distributed optically to the synapses whose weights are electrically determined. The interaction matrix  $[w_{ij}]$ , which consists of the states of the switches in the matrix, is established by modulating the photoreponse of their crosspoints by means of their bias [22]. This configuration where  $w_{ij}$  is electrically controlled allows many advantages that are intrinsic to the OE switching matrix. First, if the crosspoints can be rapidly modulated, a very fast processor could be realized. Second, the very high isolation found in the OE configuration due to the use of optically distributed neural states enables the operation of very high throughput trained networks. Finally, a unique feature of this configuration is the versatility of the synapses that permits for the wide synaptic dynamic range (50 - 70 dB) that is sometimes required in these networks.

### **1.3.5 Optoelectronic Mixer Arrays**

In an OE matrix, the crosspoints are used to switch the signals on and off. It has been shown in mixing experiments that the sensitivity of photoconductor crosspoints can be switched in approximately 250 ps [23] which indicates that optoelectronic crosspoints can be utilized efficiently as chopper modulators to mix wideband signals. In this optoelectronic mixer, one signal is an intensity-modulated optical signal while the other one is a modulated electrical bias which combine to result in a mixed electrical signal at the output.

If one applies local oscillator signals to the crosspoints of an optoelectronic switching array, an array of tuners is then obtained. Two independent types of switching can be achieved at the same location by the transmission of frequency division multiplexed optical signals. An optimum use of the OE switch bandwidth is thus accomplished by providing matrix switching of a very large number of moderate bandwidth signals [24].

## **1.4 PROJECT GOALS**

This MSc. project consists in the design and construction of 10X10 optoelectronic (OE) switching matrix with the following design goals: bandwidth per channel in excess of 1 GHz, 0 dB throughput loss, an isolation level greater than 60 dB and a large SNR (>30 dB in a 1 GHz bandwidth). The matrix is intended as a testbed for many of the applications presented above.

The design philosophy for this project was to break up the construction of the matrix into 4 modules that could be designed, built and tested independently. The four functional modules composing an OE matrix are the transmitter module, the optical power distribution module, the switching module and the amplifier & equalizer module. The last two modules can be seen as a split of a larger module known as the receiver module. A block diagram is shown in figure 1.6 where the

four functional modules are assembled together to form the final 10X10 OE switching matrix.

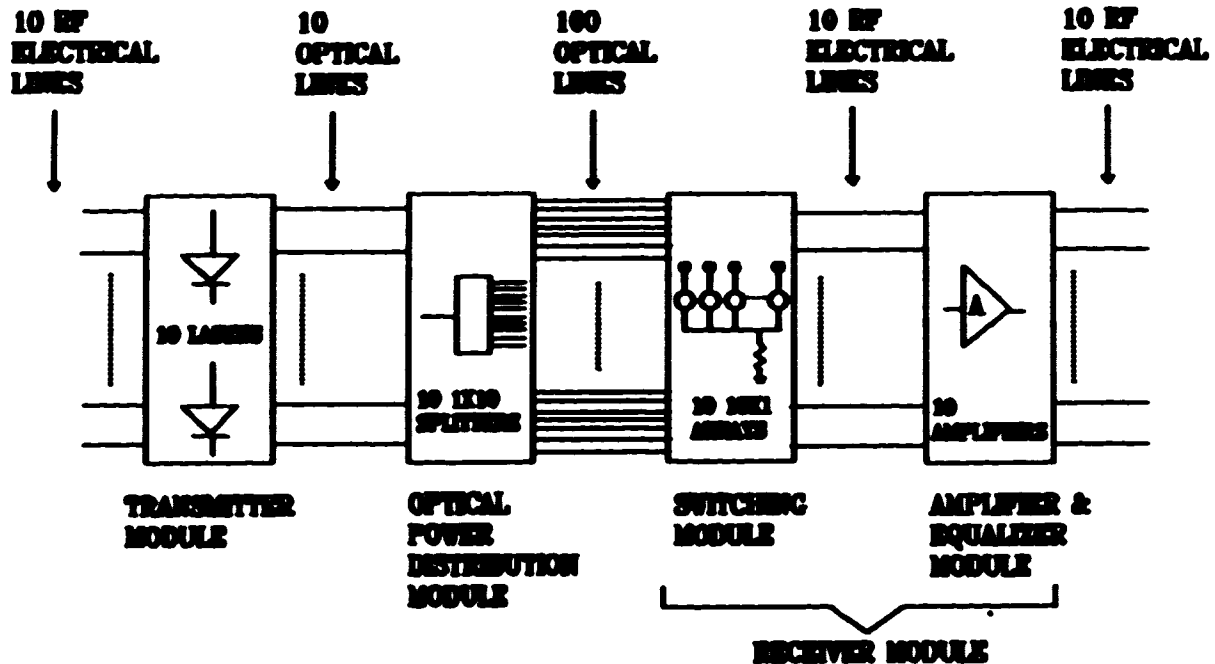


Figure 1.6 Block Diagram of an Optoelectronic Switching Matrix.

The design approach was to utilize commercially available electronic parts, along with novel custom made photodetectors for the crosspoint arrays, to build each functional module and to then assemble them into a self-contained unit. It was intended to use multi-mode lasers with a common biasing circuit for the transmitter module, multi-mode fibres and multi-mode fused biconical power splitters for the optical power distribution network and Monolithic Microwave Integrated Circuit (MMIC) gain blocks for the receiver module.

The custom made photodetector devices used as the crosspoint arrays are surface-depleted GaAs photoconductors and were fabricated by the Communications Research Centre as part of a Memorandum of Understanding



between the Department of Communications (DOC) and the Alberta Telecommunications Research Centre (ATRC). These photoconductors were studied in the context of their utilization as crosspoints in a OE switching matrix and it was not intended to characterize the behavior of the devices fully nor to model them completely since the devices are novel and are at present made with a non-optimized process.

This thesis reports the design and construction of the complete 10X10 switch matrix and its characterization. This thesis is organized as follows. In the following four chapters, the design and construction of the functional modules of the OE switching matrix are described. Thereafter, in chapter 6, the integration of the functional modules is discussed and then the overall performance of the matrix is analyzed. Finally, conclusions are drawn from the obtained results and recommendations are proposed to improve future works.

## CHAPTER 2 TRANSMITTER MODULE

### 2.1 OPTICAL SOURCES

#### 2.1.1 Design considerations

In optical communication systems such as an OE switching matrix, the optical source is often considered as the sole active element. Its main function is the conversion of an electrical signal to an optical signal that must be launched into an optical fibre. A typical curve of light output against current is illustrated in figure 2.1 for a LED and a semiconductor injection laser. The first criterion in the source selection is its compatibility with the chosen fibre waveguide. This requires that the source fulfils the following four requirements [25,27]:

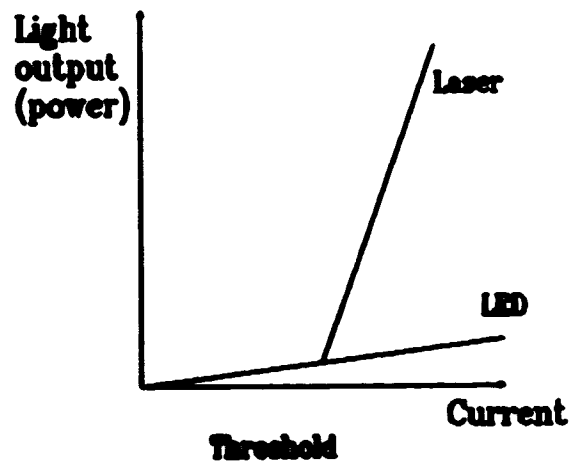


Figure 2.1 Typical light output for luminescent sources.

- (a) Small emitting surface area and good spatial coherence to permit focusing of the light to a spot size smaller than the core.

- (b) High directionality to launch light within numerical aperture of the fibre
- (c) Emitted wavelength in one of the fibre's low attenuation windows.
- (d) Narrow spectral bandwidth to minimize dispersion in the fibre.

On top of the aforementioned requirements, the optical source must also meet other stringent specifications such as [25,26]:

- (e) Good linearity to incoming electrical signals.
- (f) High optical power to obtain a good SNR at the receiver output.
- (g) Large bandwidth and fast response time to achieve simple intensity modulation.
- (h) High reliability and low cost.
- (i) Low electrical power consumption.
- (j) Poor time coherence to minimize modal noise.

Only luminescent sources can fulfill most or all of these requirements. The most common luminescent sources are the Light Emitting Diodes and the Semiconductor Injection Lasers. Until recently, LEDs have been the logical choice for applications where the cost, reliability, simplicity and linearity of the devices were the critical criteria. However, in recent years, technological advancements as well as mass production have allowed lasers to meet these last specifications in an adequate fashion. On the other hand, lasers have major advantages over LEDs in the applications that are foreseen for the OE matrix. These advantages include [25]:

- 1) High emitted optical power.

- 2) **Narrow linewidth (This property involves a trade-off between dispersion and modal noise).**
- 3) **Large modulation bandwidth.**
- 4) **Spatial coherence.**

**In the light of what has just been mentioned, semiconductor injection lasers seem to be the logical choice in the selection of optical sources in an OE switching matrix.**

**The next step involves the choice of the laser source itself. The critical parameters that must be considered in the selection of the laser source are the wavelength, the emitted optical power, the modulation frequency response, the threshold current, the temperature stability, the signal-to-noise ratio and the cost.**

**In a hybrid OE switching matrix, the length of the waveguides does not exceed a few meters and therefore the optical attenuation as well as the pulse dispersion are not major considerations. This allows the use of short wavelength lasers (780-840 nm) and multimode fibers. Short wavelength lasers are inexpensive and reliable due mostly to their extensive development and production for use in commercial products such as compact disc players, optical video disc players, thermo-magneto-optic disks and laser printers [27]. The use of short wavelength devices such as GaAlAs lasers in the transmitters also allows the use of GaAs photodetectors which could lead, in the future, to an all GaAs Integrated Optoelectronic Switching matrix [28]. The various design considerations have led to the selection of the Mitsubishi ML60X1 laser family as our optical sources. Their characteristics are discussed in the following section.**

### 2.1.2 Mitsubishi ML60X1 laser family

The ML60X1 lasers are high power laser diodes emitting light at a wavelength of 780 nm. They emit 10 mW of optical power with a forward bias current in the order of 65 mA, approximately 25 mA above the threshold current  $I_{th}$ . A high power laser is required due to the necessity of delivering a few hundred microwatts at each crosspoint to achieve a good frequency response as well as a good SNR at the receiver in the required 1 GHz bandwidth. This point will be elaborated in more detail in a subsequent chapter. The lasers can also operate in either a continuous wave (CW) or pulsed mode up to a case temperature of 60°C [29].

The SNR of the laser beam is defined as:

$$SNR = \left( \frac{P_s}{S_n} \right)^2 \quad \text{equation 2.1}$$

where  $P_s$  is the average optical power and  $S_n$  is the noise optical power [27]. For the ML60X1 family this parameter is rated at approximately 85 dB electrical in a 300 kHz bandwidth centered about 10 MHz for an operating optical power of 10 mW. This can be extrapolated to a SNR of 50 dB in a 1 GHz bandwidth which shows that the optical source is probably not the component that limits the 30 dB signal-to-noise ratio targeted in this project. On the other hand, this SNR value decreases as the average optical power decreases from the specified operating point. This is caused by the dependence of the emission spectrum on the average optical power. The emission has a single mode spectrum at high radiance and a multimode spectrum at low radiance. It has been shown that single mode lasers have a greater immunity to intensity noise than their multimode counterparts [30].

The emission spectrum for a ML6101A laser, at room temperature, for a bias current of 66 mA is shown in figure 2.2. It can be seen that the optical emission is not perfectly confined to a single mode at this operating point. The main peak and secondary peak on the graph correspond to wavelength of 772.8 nm and 773.7 nm respectively. Lau *et al.* [31] have shown that the longitudinal mode spectrum of single mode semiconductor lasers is locked for optical modulation depth up to ~80%. This indicates that the modulation of the laser should not affect appreciably the intensity noise level of the device.

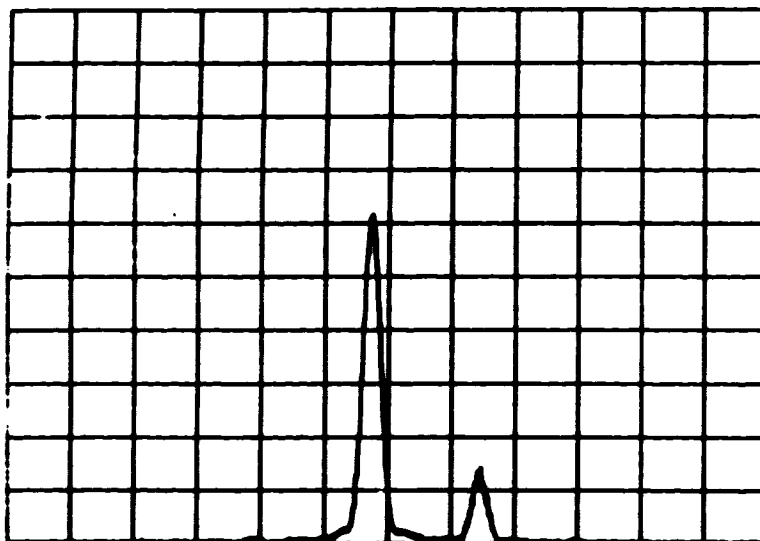


**Figure 2.2** Emission spectrum for a ML6101A laser diode for a bias current of 66 mA as measured with a McPherson model 270 monochromator. The 2 peaks are emitted at 772.8 nm and 773.7 nm.

An essential pre-requisite to the design of a broadband OE switching matrix is the use of high speed optical sources. The modulation frequency response of a ML6101A laser is illustrated in figure 2.3(a) for two different

modulation depths. It can be observed that the response is flat up to 2 GHz where the curve starts to roll off. The ripples are due to a slight mismatch between the test analyzer 50 ohm output impedance and the laser circuit input impedance. The 2 GHz bandwidth in this set-up is limited by the bandwidth of the detector. This assertion is confirmed in figure 2.3(b) where a different detector is used. In this figure, it can be seen that the response is flat from 1 GHz to 3 GHz. The rise in the response at lower frequencies is explained by a diffusion process of electrical carriers from the undepleted intrinsic region to the photodetector's depletion region. These results are obtained for a modulation index varying from 10% to 80%. It can then be concluded that the ML6XX1 laser family has an analog bandwidth greater than 3 GHz.

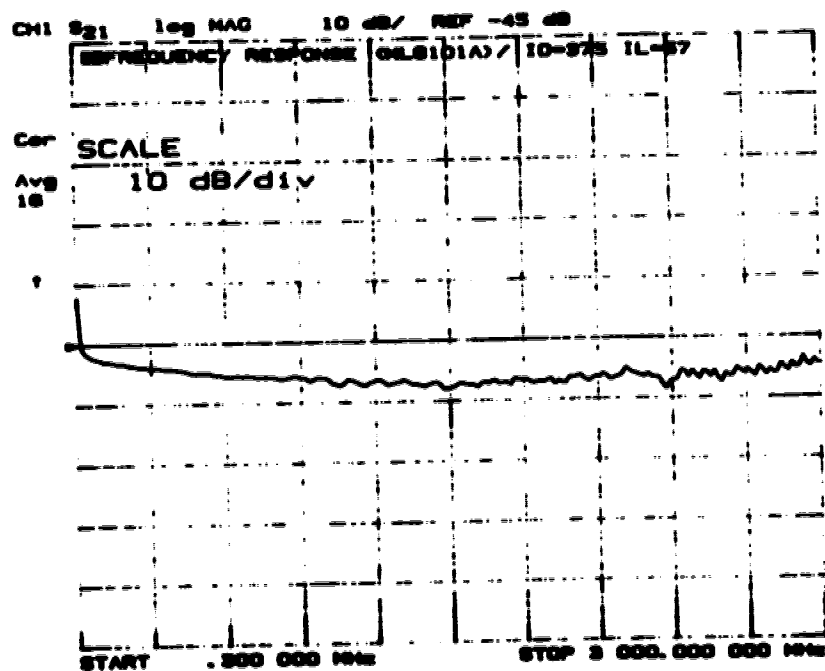


Figure 2.3 (a) Modulation frequency response of a ML6101A laser diode using a InGaAs p-n detector.

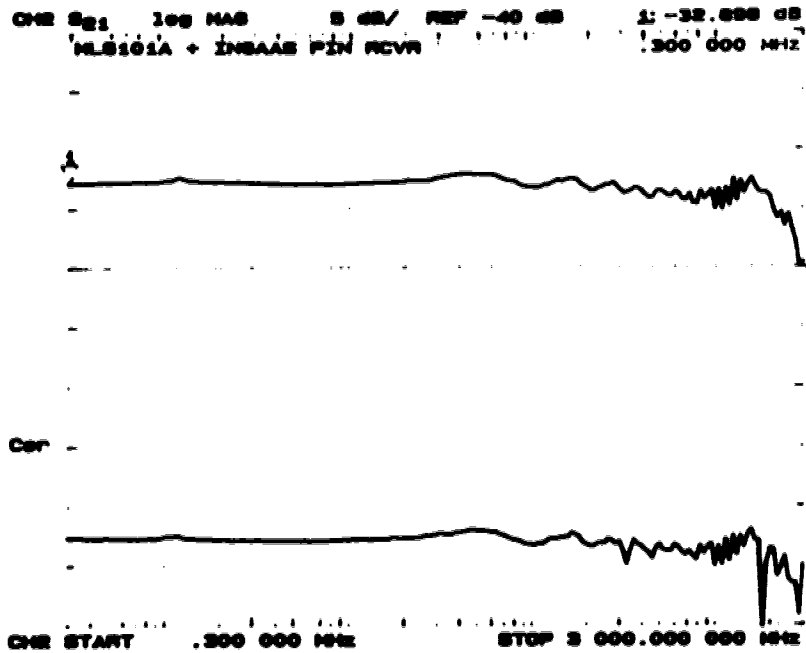


Figure 2.3 (b) Modulation frequency response of a ML6101A laser diode using a Si p-i-n detector.

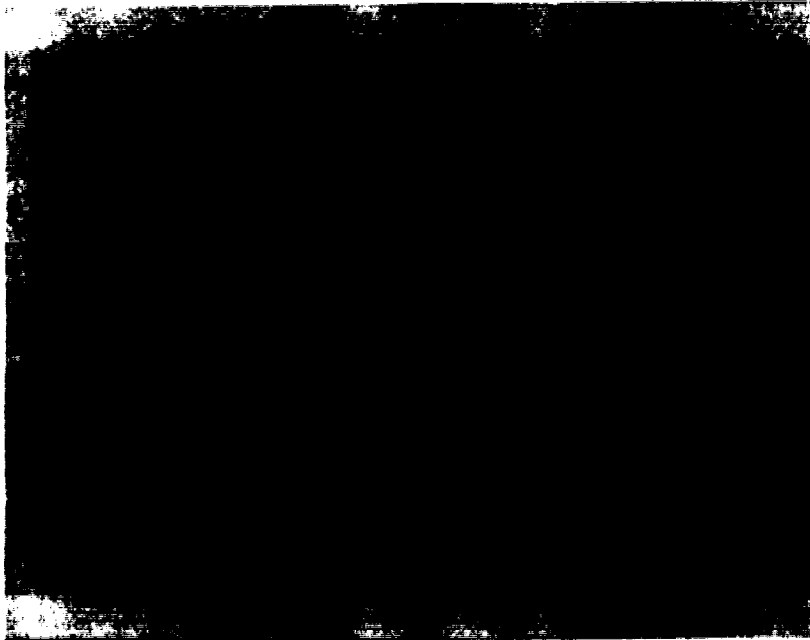


Figure 2.4 Impulse response of a ML611C laser using a Si p-i-n detector (courtesy of N. Vethanayagam).



Figure 2.4 shows a typical impulse response for the ML6XX1 laser family. The 10-90% raise time and fall time are measured and found to be 0.4 and 0.8 ns respectively. These values are rated by the manufacturer as 0.3 and 0.4 ns. The discrepancy between the two fall times seems to be caused by the different detectors used in the experiments. The rise time  $\tau_r$  of a device can be estimated as a function of the bandwidth  $B$  by using equation 2.2 [25]:

$$\tau_r = 0.35/B \quad \text{equation 2.2}$$

If the 3 GHz bandwidth is used in equation 2.2, this leads to a calculated value for the rise time of the order of 100 ns. For a non-return to zero format (NRZ), the maximum bit rate  $R_b$  is related to the rise time in the following fashion [25]:

$$R_b = 0.7/\tau_r = 2*B \quad \text{equation 2.3}$$

Equation 2.3 shows that 6 Gbit signal rates could theoretically be achieved by the ML6XX1 laser family. However, a more conservative value of 2 Gbit/s is obtained if a rise time value of 0.3 ns is assumed. Nevertheless, this confirms that these lasers are more than adequate as broadband optical sources for an OE switching matrix whose bandwidth is aimed at 1 GHz.

The threshold current density for an injection laser tends to increase with temperature, as the threshold current density obeys approximately an exponential relationship of the following form [29]:

$$J_{th} \propto \exp(T/T_0) \quad \text{equation 2.4}$$

where  $T$  is the absolute temperature and  $T_0$  is the threshold temperature coefficient which is a characteristic temperature describing the quality of the material, but which is also affected by the structure of the device [25]. This temperature dependence is illustrated in figure 2.5. For GaAlAs devices,  $T_0$  is usually in the range 120-180 °K [32]. This coefficient is rated as 180 °K for the ML6XX1 laser family which demonstrates that these optical sources are as temperature stable as is possible for a GaAlAs laser. Nevertheless, the high bias current flowing in the device increases the laser junction temperature sufficiently to change the threshold current and a control feedback loop is required in the laser biasing circuitry if a constant optical output is desired.

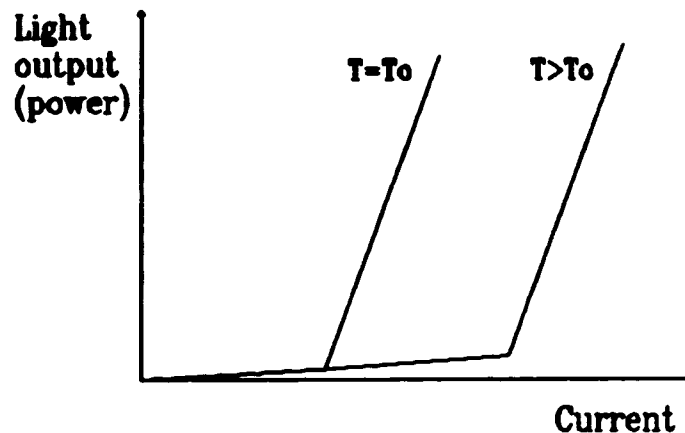


Figure 2.5 Typical variation in laser output with junction temperature

## 2.2 BIASING CIRCUIT

It was established in the previous section that the threshold current and hence the DC optical power emitted from the transmitter is very sensitive to the

laser junction temperature. To obtain a steady optical output, one can either maintain the junction temperature constant, or control the device bias current.

The laser junction temperature can be kept constant by using a Peltier effect cooler. However, this method has the disadvantage that Peltier effect coolers require large currents and thus cause important power dissipation problems [26].

The laser bias current can be adjusted by monitoring the optical output and comparing it to a reference level. The simplest and perhaps the most common form of laser drive circuit incorporating optical feedback is the mean power control circuit which is schematically shown in figure 2.6. A monitor photodiode, positioned next to the rear of the laser package, records the average optical output. The detected signal is integrated and compared with a reference voltage by an operational amplifier which is used to servo-control the DC bias current flowing through the laser. Thus the mean optical power is held constant by varying the DC bias current level. This technique has the advantage that it is suitable for both digital and analog transmission systems [25].

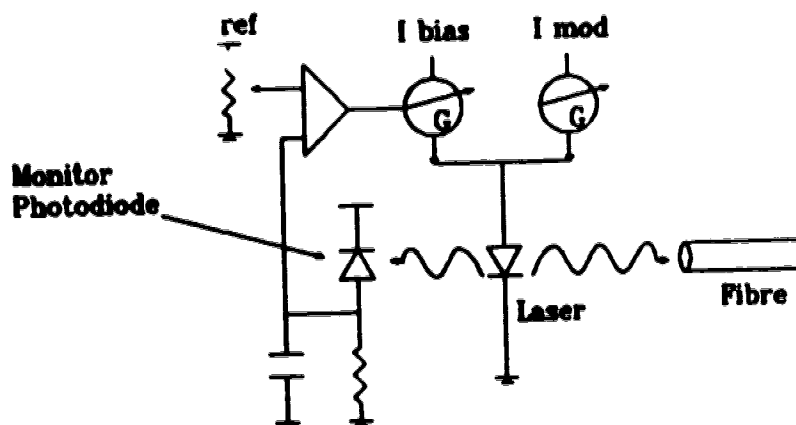


Figure 2.6 Mean power feedback circuit for control of the laser bias current.

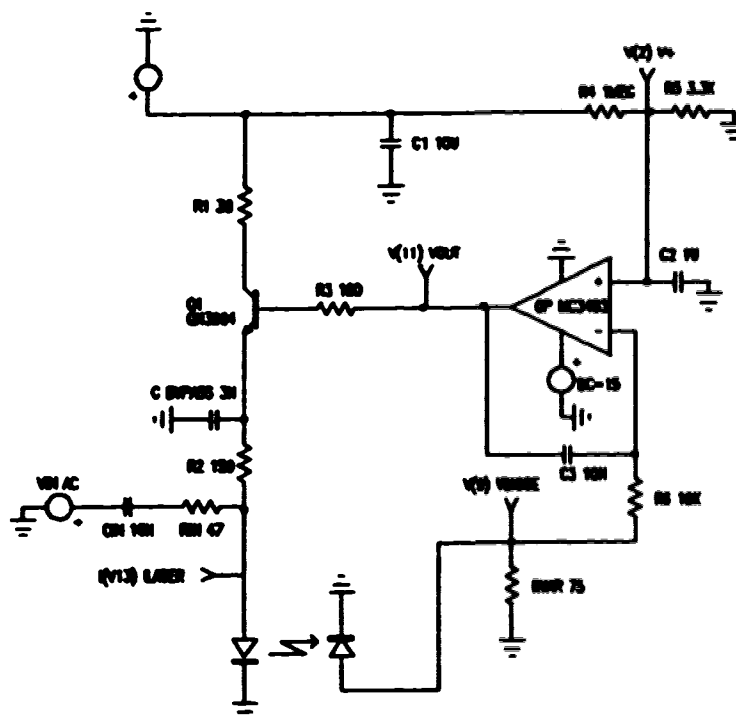


Figure 2.7 Analog laser driver circuit.

The analog laser biasing circuit used in this project is illustrated in figure 2.7. The negative feedback loop tracks and attenuates low frequency changes in the laser output while allowing high frequency variations to pass through unimpeded. The circuit operates as following. The current flowing through the laser diode also flows through the n-p-n transistor, which is controlled by the operational amplifier (OP AMP) output voltage which in turn is set by the relationship between the monitoring photodiode current and the reference voltage generated by  $R_4$  and  $R_5$ . A variation in the emitted optical power would result in a different current at the photodiode which would then force a correction at the OP AMP's output. The speed at which the circuit can respond to changes in the laser's output power is determined by the time constant of the feedback loop.

The variable resistor  $R_{VAR}$  is used to set the average optical power at the laser diode's operating point. The optical power from the laser generates a photocurrent in the photodiode which produces a proportional voltage across  $R_{VAR}$ . The OP AMP controls the current through the laser to maintain  $V_{DIODE}$  equal to the reference voltage  $v^*$

Figure 2.8 illustrates the start-up operation of the laser driver at four different points in the circuit at a fixed temperature. It can be seen that the reference voltage  $v^*$  is the first point to reach steady state. Thereafter, the OP AMP's control voltage  $v_{OP}$  rises continuously and smoothly to its constant value. As the OP AMP's voltage exceeds approximately 2 Volts, the laser current  $I_{LASER}$  starts to flow. Once the laser bias current goes beyond threshold, the light output varies rapidly with current (lasing) and the voltage across the photodiode  $V_{DIODE}$  rises. The whole circuit reaches electrical equilibrium in about 40 msec. However, due to the slow increase in the laser junction temperature, it may take, in practice, a few minutes before thermal equilibrium is reached.

In figure 2.9, it is shown how the biasing circuit behaves when an AC signal, whose frequency varies from 10 Hz to 100 kHz, is directly applied to the laser diode once working at the operating point. It can be noticed that, for the chosen component values, the circuit ignores perturbations faster than 100 Hz.

The values of the various components in the circuit are chosen following certain guidelines which are listed in appendix A [33]:

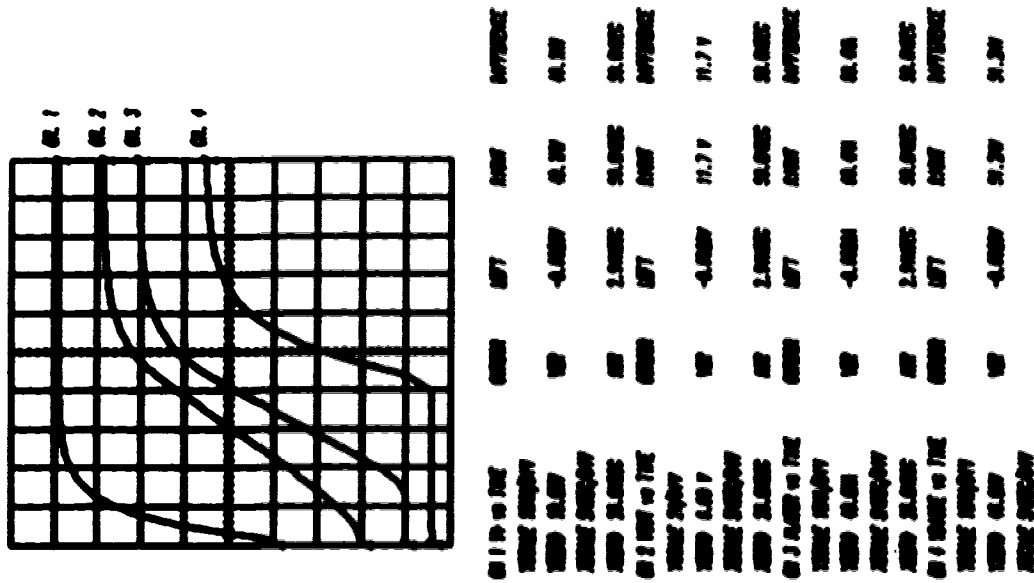


Figure 2.8 Laser driver's transient response.

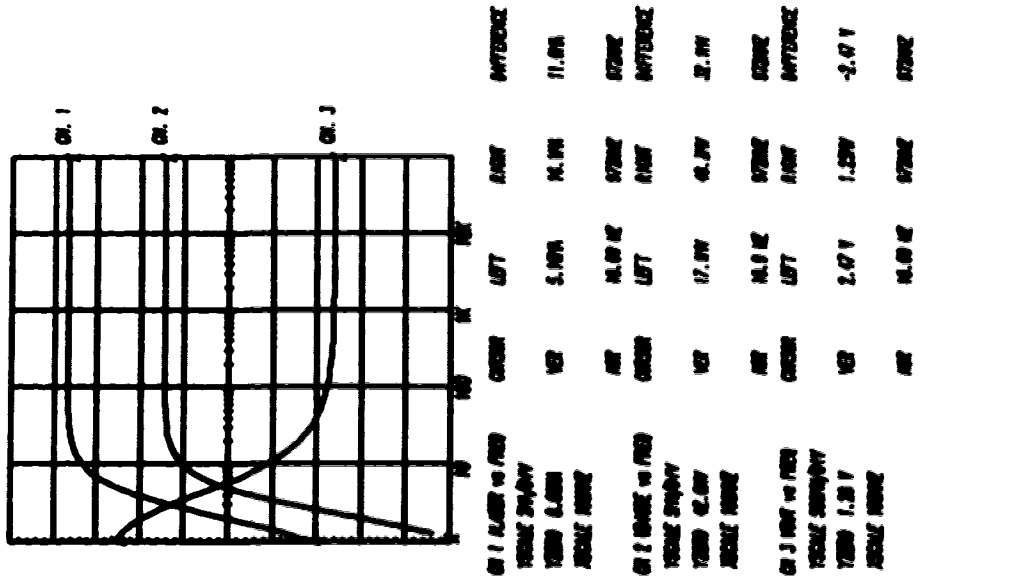


Figure 2.9 Input perturbation tracking of the laser driver.

## 2.3 TRANSMITTER HOUSING

Once the choice of the laser source is made and the design of its driver is completed, the next task is the housing of ten of these sub-units into a compact transmitter module. To facilitate the coupling of light from the transmitters to the fibre waveguides, a pigtailed version of the ML6411C laser was selected. From figure 2.10, it can be noticed that the assembling of the laser with the beam coupling optics in a sealed package does not seem to affect the high frequency performance of the transmitter. The coupling efficiency achieved with this arrangement is in the order of 50% which means that approximately 5 mW of optical power is available at the fibre outputs.

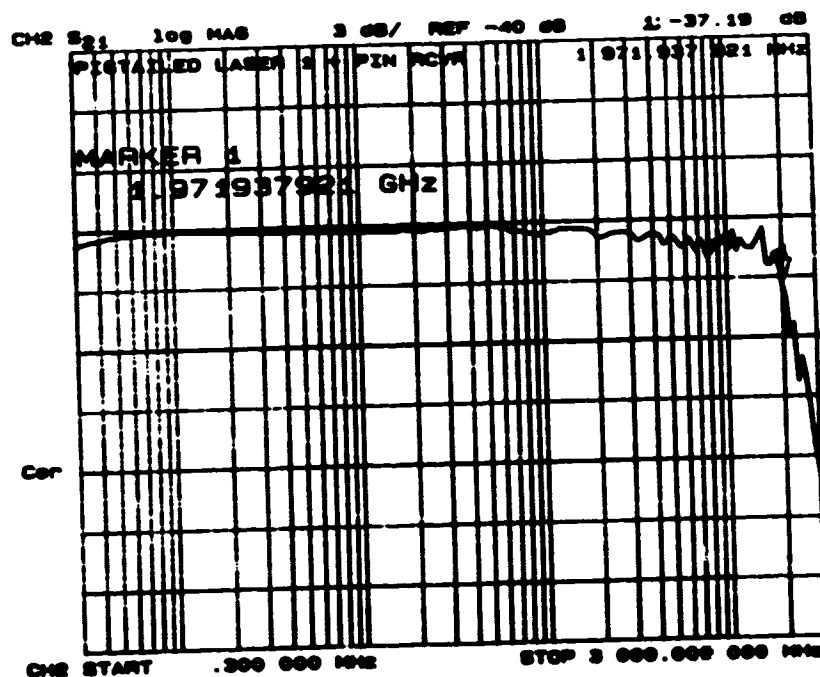


Figure 2.10 Modulation frequency response of a complete transmitter using a pigtailed ML6411C laser as measured with a InGaAs p-i-n detector.

The integration of the ten laser sources into a transmitter module is achieved by the use of two arrays of five lasers where each laser is housed in a shielded brass compartment. The housing assembly is shown in the photograph in figure 2.11. Surface mounted components are used for  $R_{L_{20}}$ ,  $C_{L_{20}}$  and  $R_2$  (see figure 2.7) to minimize the distance between the RF sensitive parts of the circuit as well as to take advantage of the low reactance of this type of component at high frequencies. A feedthrough capacitor is also used between the resistor  $R_2$  and the transistor  $Q_2$  to bypass to ground any RF leakage that could occur through  $R_2$ .



**Figure 2.11 Laser housing assembly.**

The isolation provided by  $R_2$  and this bypass feedthrough capacitor allows for the construction of the remainder of the biasing circuit at a greater distance from the housing assembly. The five laser array requires five different biasing



circuits which are mounted on a common printed circuit board. The printed circuit board, which constitutes the support for the housing assembly, is designed to slide and fit into a standard 6U card frame. The whole transmitter module is thus composed of two cards as it can be seen in figure 2.12.

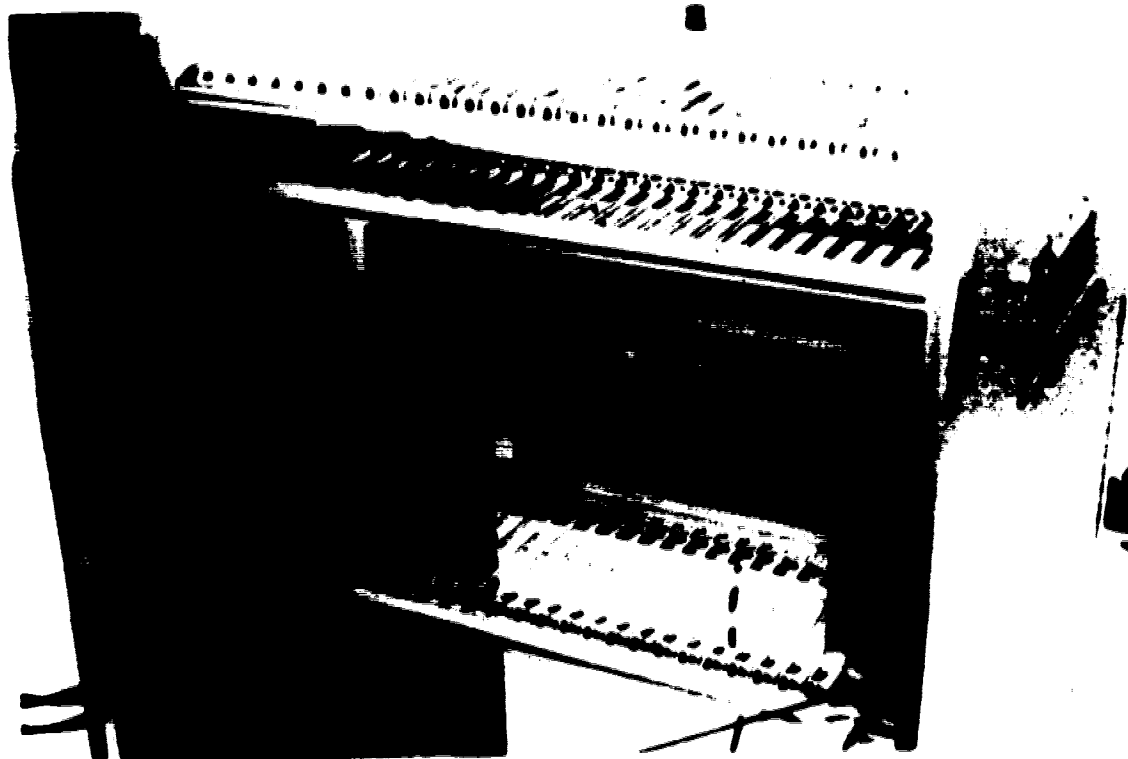


Figure 2.12 Transmitter module.

The required signal drive level at each transmitter  $v_{mod}$  can be calculated as a function of the modulation depth  $m$ :

$$\begin{aligned}
 v_{mod} &= m \cdot (I_{LAMP} - I_{th}) \cdot 500 \\
 &= m \cdot 25 \text{ mA} \cdot 500 \\
 &= 1.25 \cdot m
 \end{aligned}$$

equation 2.5

This corresponds to an electrical power drive level  $P_{e1}$  of:

$$P_{e1} = \frac{v_{rms}^2}{2 \cdot 500}$$

$$= 12 \text{ dBm} + 20 \log(m) \quad \text{equation 2.6}$$

The laser driver is designed to run from a positive 15 Volt power supply, which allows the resistance of  $r_2$  to be large enough to guarantee that the RF and DC parts of the circuit are well-isolated from each other. As underlined in section 2.1.2, the laser sources require a bias current in the order of 65 mA each. This results in a power dissipation of nearly three quarters of a Watt in  $r_2$  and the laser diode inside each chamber in the housing assembly. These components are not in direct contact with the brass walls so that good heat dissipation is hard to achieve. This problem is solved by employing a fan and forcing an air flow into the housing assembly. The fan is connected to the housing assembly through a pipe arrangement. Mesh walls are used to EM shield individual chambers and allow the circulation of the forced air flow from one end of the array to the other.

The crosstalk between adjacent laser sources was measured and it was found that it is less than -75 dB. This crosstalk is mostly due to the electromagnetic coupling through the air from the RF generator to the optical receiver used in the experiment. This demonstrates the shielding efficiency of the mesh walls and the whole housing assembly.

**CHAPTER 3**  
**OPTOELECTRONIC CROSSPOINTS**  
**(SWITCHING MODULE)**

**3.1 CROSSPOINT REQUIREMENTS**

In an OE switching matrix the photodetectors are the actual switches. They convert the received optical signal into an electrical signal, which is then amplified before further processing [28]. Isolation is a measure of the crosstalk level that is introduced by the optoelectronic crosspoint. It is therefore an important parameter that indicates the performance of the switch [34]. The isolation of an optically coupled switch is defined as the ratio of the power in the electrical response to the incoming optical signal when the photodetector is in the on-state to that when the photodetector is in the off-state. The on-state coincides with the device being photosensitive and the off-state with the device being not sensitive [35].

In addition to the necessity for good isolation, broadband performance and fabrication process compatibility impose very stringent requirements on the crosspoints. These requirements are very similar to those found for the lasers since the photodetector is the counterpart of the optical source. They include [25]:

- (a) Large responsivity at operating wavelengths.
- (b) High fidelity. The detector should be linear with regard to the optical power.
- (c) Large bandwidth.
- (d) Low noise level.

- (e) **Reliability and stability of performance characteristics.** The device characteristics should be independent of the ambient conditions.
- (f) **Easy electronic integration.**
- (g) **Small size to allow good light coupling and easy packaging.**
- (h) **Low operating voltage and low power dissipation.**
- (i) **Low cost.**

In the next subsection, different types of photodetectors in use are briefly discussed and their attributes are analyzed for suitability as crosspoints for the construction of 10X10 OE switching matrix with the specified performance.

## **3.2 CROSSPOINT SELECTION**

### **3.2.1 Homojunction crosspoints**

The first crosspoints used in an optoelectronic switching matrix were homojunction Si p+n photodiodes [3]. These p+n photodiodes were rendered sensitive by applying a reverse voltage of typically 20 Volts. The off-state, in turn, was established by forward biasing the photodiodes with a current of the order of 10 mA or larger. When the photodiode is forward biased, it is equivalent to a large capacitor that short-circuits the load resistor at the output line. The information signal then can not be extracted. The level of isolation is directly proportional to the value of the junction capacitance which, in turn, is directly proportional to the bias current. An isolation level greater than 80 dB has been reported for OE matrices using homojunction photodiodes as crosspoints [36].

It is also possible to utilize homojunction avalanche photodiodes (APD) as optoelectronic switches instead of p+n photodiodes [37], but a larger reverse bias voltage is required in the on-state. The avalanche photodiodes have an extra mechanism that allows a higher level of isolation than their p+n counterparts in

the off-state: the elimination of avalanche gain. Consequently, compared to the case of p-i-n photodiodes, a smaller forward biasing current is needed by avalanche photodiodes to obtain the same isolation level.

Homojunction p-i-n photodetectors show very good isolation results. However, these devices are extremely slow to switch and can only be used for space division switching applications. The slowness of these photodetectors is intrinsic to their homojunction structure. While in the off-state, maximum isolation level is obtained under forward biasing and a significant amount of charge is accumulated at the junction. Therefore, before the switch can be turned on, all the stored charges must be removed from the junction. This limits the switching speed of the devices to a few hundred nanoseconds [36,37]. For the fabrication of a large array of integrated optoelectronic switches, this forward bias current would also present a difficult problem of heat dissipation and complicate the design of the summing network [38].

When homojunction avalanche photodiodes are used as crossovers in an OE switching matrix, we encounter the serious technical problem of switching large bias voltages in short times. If the off-state is chosen to be a zero-bias current, the reverse bias voltage required to provide a high avalanche gain and therefore a high isolation is of the order of 100-200 Volts [37].

### 3.2.2 Heterojunction crossovers

Enhanced isolation can be attained without avalanche gain by the use of heterojunction photodiodes [39]. The heterojunction prevents the collection of photogenerated charges when the reverse bias is below the threshold level. 80 dB of isolation over a frequency range of 1-500 MHz has been recorded for an experimentally fabricated InGaAs/InP photodiode [39].

The power consumption of heterojunction photodiodes in an optoelectronic switching matrix is quite small because little current flows under reverse bias for the on-state condition and a zero bias current is used for the off-state condition. Because a zero bias current is used for the off-state condition, no charges are stored at the junction, allowing switching times of the order of 30 nanoseconds [39]. Although electrical power consumption and relatively high speed switching capabilities are major advantages for heterojunction photodiodes, the high reverse bias voltage required in the on-state condition makes this type of photodetector unsuitable for high speed switching applications.

The conventional telecommunication optical detectors mentioned in the previous sections are vertical structures and can not be easily integrated with amplifier electronics because the fabrication steps required in their integration are not compatible with existing VLSI fabrication processes. For short wavelength systems, GaAs can be used for optical detection. The very thin characteristic absorption depth of GaAs ( $1 \mu\text{m}$ ), for the radiation emitted from AlGaAs devices, allows for a planar structure which is more suitable for integration. The most common planar structure photodetectors found in the literature are photoconductors and double Schottky diodes. The latter are briefly discussed in the next section while the former structure is more thoroughly analysed in the subsequent section.

### 3.2.3 Metal-Semiconductor-Metal Photodetectors

A Metal-Semiconductor-Metal (MSM) photodetector consists of double Schottky contacts placed upon an undoped semiconductor layer as illustrated in figure 3.1. A Schottky contact is usually obtained by using a metal whose work function is larger than the semiconductor's work function. Because of its planar

structure, the MSM photodetector is intrinsically compatible with the gate fabrication process of metal-semiconductor field effect transistors (MESFET). The integration of both types of devices can be achieved without introducing any additional process steps.

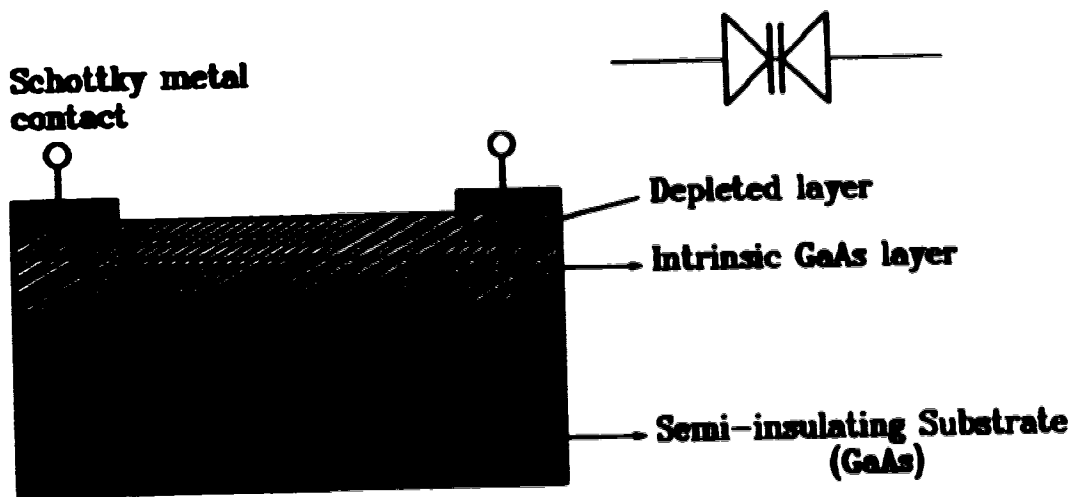


Figure 3.1 Double Schottky Photodiode (MSM).

Schottky contacts are blocking contacts which means that the photodetector can be represented as opposed diodes. This implies that the emission current is saturated. In other words, an increase in the electric field near the contact, or an increase in the conductivity of the semiconductor, does not lead to a rise in current from the contact [40]. In an OE matrix, the opposed diode structure also enables the use of an unbiased off-state which eases the summation function at the crosspoints. Furthermore, this structure allows for very low dark currents in the order of few nanoamperes [41].

As a first approximation, the depletion width at the metal-semiconductor interface is similar to that found for a standard one-sided abrupt  $p^+ - n$  junction and is proportional to  $1/\sqrt{N_d}$ , where  $N_d$  is the donor density [42]. It is advantageous to

use an intrinsic semiconductor as the channel if a large depletion layer is desired at a relatively low on-state bias. If the depletion layer under bias extends from one contact to the other, the device is called a Mott device. Typically, Mott devices can be achieved for biases of a few volts.

When a sufficient bias is applied to create a Mott device and if the depletion region extends vertically into the detector over a distance greater than the characteristic absorption depth, the photogenerated holes are swept towards the reversed biased contact where they recombine at the semiconductor-metal interface. The electrons are swept toward the forward biased contact, and recombine in the bulk material [43]. There is no reinjection of carriers from the electrodes due to the Schottky contact barrier and no gain is expected [44]. However, a low internal gain, in the order of 2 to 3, is sometimes observed. The gain mechanism is believed to be caused by a modulation of the Schottky barrier height at the anode allowing for a small reinjection of holes [41].

The bandwidth of a MSM photodetector is theoretically limited by the transit time of the carriers or the *rc* time constant of the detector, whichever is the slowest. A 10 GHz GaAs MSM, limited by its transit time, has been reported in the literature [41]. In practical devices, a falling tail is often observed in the impulse photoresponse. This can be caused by either hole trapping in the depletion layer or diffusion of photocarriers generated outside the high electrical field region. Nevertheless, this falling tail is usually low in amplitude compared to the peak pulse amplitude because of the absence of gain in the device.

Despite their large bandwidth and low noise characteristics, MSM photodetectors suffer from two major drawbacks in their utilization as crosspoints in an OE switching matrix. The first difficulty is the accumulation of charges at the metal-semiconductor junctions which limits the switching speed of the crosspoints. Forrest *et al.* [6] have measured switching speeds in the order of



100 ns for a 1X8 array. This is too slow for many signal processing applications that are foreseen for the OE switching matrix.

The second and most serious limitation of the MSM photodetectors as crosspoints is their low isolation level which is typically 50 dB [6] or lower. The isolation level is reduced by the existence of two oppositely directed junctions that extend into the channel. The symmetry of the two Schottky barriers control the level of isolation that can be obtained. Unbalanced photovoltages in the two opposed junctions can cause off-state response and hence a degradation of the isolation. The addition of off-state responses along the matrix columns could be a limiting factor in the size of an OE switch if the isolation obtained with MSM photodetectors is poor.

#### 3.2.4. Photoconductors

The structure of photoconductive detectors is very similar to the structure of MSM photodetectors, except that the Schottky contacts are replaced with ohmic contacts. An ohmic contact supplies a reservoir of carriers freely available to enter the semiconductor as needed. Good ohmic contacts should supply the required current with a voltage drop that is small compared with the drop across the active region of the photodetector. A figure of merit of an ohmic contact, as a function of the current density  $J$ , is the specific contact resistance, defined as:

$$R_c = \left( \frac{\delta J}{\delta V} \right)^{-1} \quad \text{equation 3.1}$$

For metal-semiconductor contacts with low doping concentrations, the dominant current transport process is the thermionic emission and  $R_c$  is then related to the Schottky barrier height  $\phi_{b0}$  as follows [42]:

$$R_c \propto \exp\left(\frac{q\phi_{b0}}{kT}\right) \quad \text{equation 3.2}$$

where

- q      electronic charge
- k      Boltzmann's constant
- T      ambient temperature

For contacts with higher doping concentrations, the tunneling process dominates and  $R_c$  is given as [42]:

$$R_c \propto \exp\left(\frac{4}{h} \pi \sqrt{(\epsilon_s m^*)} \frac{\phi_{Bn}}{\sqrt{N_d}}\right) \quad \text{equation 3.3}$$

where

- h      Planck's constant
- $\epsilon_s$     semiconductor permittivity
- $m^*$     effective mass

Equation 3.2 shows that ohmic contacts can be obtained by using metals with a low work function such that a low Schottky barrier is achieved. However, it is difficult to find a metal with a work function that is low enough to yield a low barrier when the contact is made on a wide-gap semiconductor. Equation 3.3 illustrates that ohmic contacts are achievable if the metal is deposited on a highly doped semiconductor. For  $N_d > 10^{18} \text{ cm}^{-3}$ , it is possible to realize "quasi-ohmic" contacts [42]. A commonly used structure for a photoconductive detector (PC) is schematically illustrated in figure 3.2.

## Ohmic contact

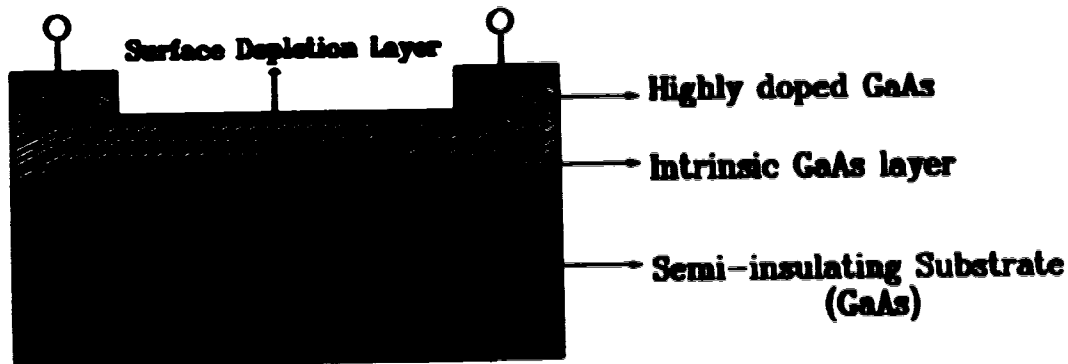


Figure 3.2 Photoconductive detector (PC).

A low work function metal is deposited on a highly doped GaAs film to achieve an ohmic contact. The photosensitive channel consists of an intrinsic GaAs layer grown on a semi-insulating GaAs substrate. It can be noticed that there exists a thin depletion layer at the surface of the photosensitive channel caused by surface charges. This point will be discussed later in this section. As with MSM photodiodes, the integration of the photoconductors with planar structure field effect transistor (FET) based amplifiers is easy to achieve due to the simplicity of the devices which are essentially FET's without gates.

The near absence of built-in electric fields in the device structure allows for an unbiased off-state. Furthermore the very thin junctions do not extend into the channel which leads to an improved isolation level. The residual response in the off-state is only caused by diffusion of the photocarriers to the electrodes. This carrier diffusion process to the electrodes is quite small, mainly due to the distance separating the channel from the contacts, and is usually symmetrical.

When light falls on the surface of the photoconductor, photocarriers are generated and create an increase in the conductivity of the channel. If an electric field is applied between the electrodes, the photo-generated carriers are swept

towards the contacts. Due to their higher mobility in GaAs, the generated electrons are swept to the anode before the holes can reach the cathode. This results in a charge imbalance in the photoconductive channel. This charge imbalance leads to the injection of electrons to the channel from the detector's ohmic cathode to maintain the charge neutrality. These injected electrons are swept to the anode, resulting in a photoconductive gain. This gain mechanism is maintained until an electron-hole recombination occurs.

It can be shown [45], that the AC current  $I_{FC}$  for a trap-free photoconductor is given by:

$$I_{FC} = \eta q n F_0 A \frac{\tau}{T_T} \frac{1}{(1+j\omega\tau)} \quad \text{equation 3.4}$$

where

- $\eta$  quantum efficiency
- $n$  modulation depth
- $F_0$  photon flux density
- $A$  detector's photosensitive area
- $\tau$  mean hole lifetime
- $T_T$  electron transit time
- $\omega$  signal angular frequency

Equation 3.4 illustrates that photoconductors have a gain that is inversely proportional to the transit time. For a field strength high enough such that the carrier velocity is in the saturation regime, the transit time is approximately a linear function of the channel length and a high gain detector is thus obtained using a short channel. On the other hand, efficient optical coupling from fibre requires a large area. A solution to these two contradictory requirements is the use of an

interdigitated structure as shown in figure 3.3. This figure shows a interdigitated photoconductor where the finger width and the channel length are 3 and 5  $\mu\text{m}$  respectively. The total area of the device is approximately 100  $\mu\text{m}$  by 100  $\mu\text{m}$ . For this photoconductor, the saturation regime is achieved for a bias of typically 1 to 2 volts [46].

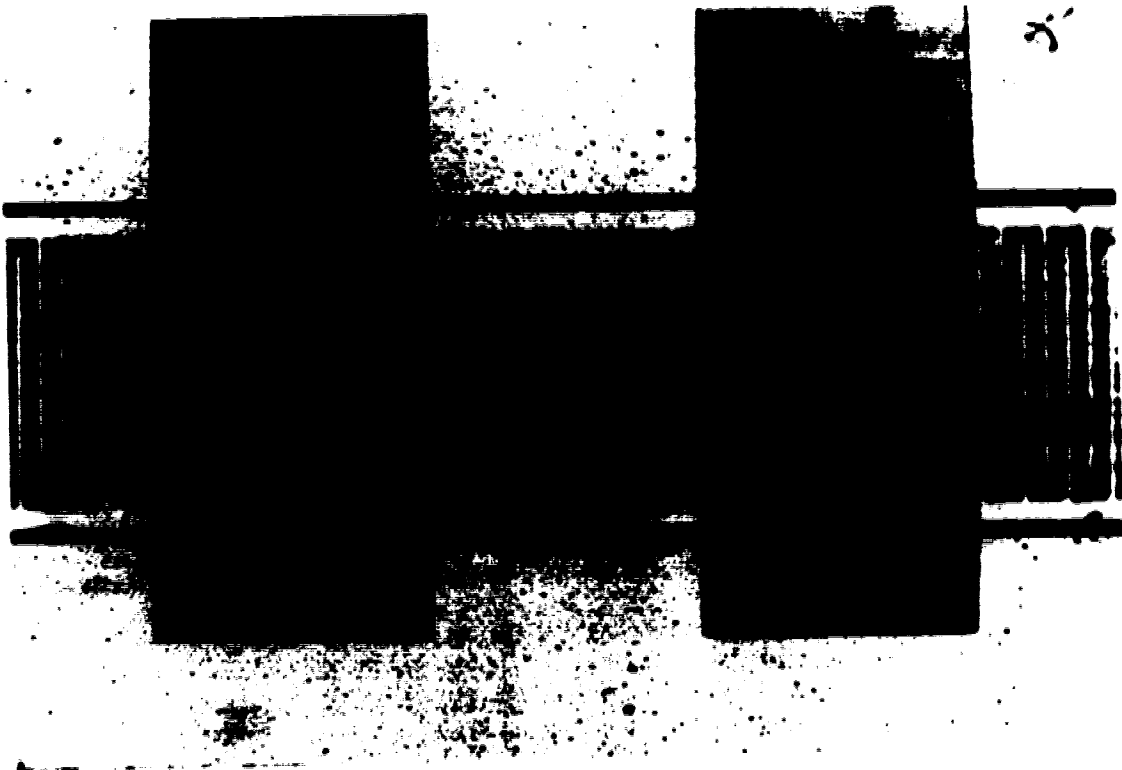


**Figure 3.3 Interdigitated Photoconductor.**

The electrical summation that occurs in an OE switch can be thought to be functionally equivalent to an "OR" logic gate whose inputs are the responses from the array crosspoints. The unbiased off-state allows the electrical summation function in a 10X1 array to be easily realized at a common point for all crosspoints, hence reducing the multiport "OR" gate into a single port "OR" gate. This function is simply obtained by monitoring the total signal across a common

load for all detectors serving a single output line [7]. An array of 10 monolithically integrated interdigitated photoconductors is illustrated in figure 3.4. This array would in principle serve as one column of a matrix, delivering any of ten incoming optical signals to the single output line.

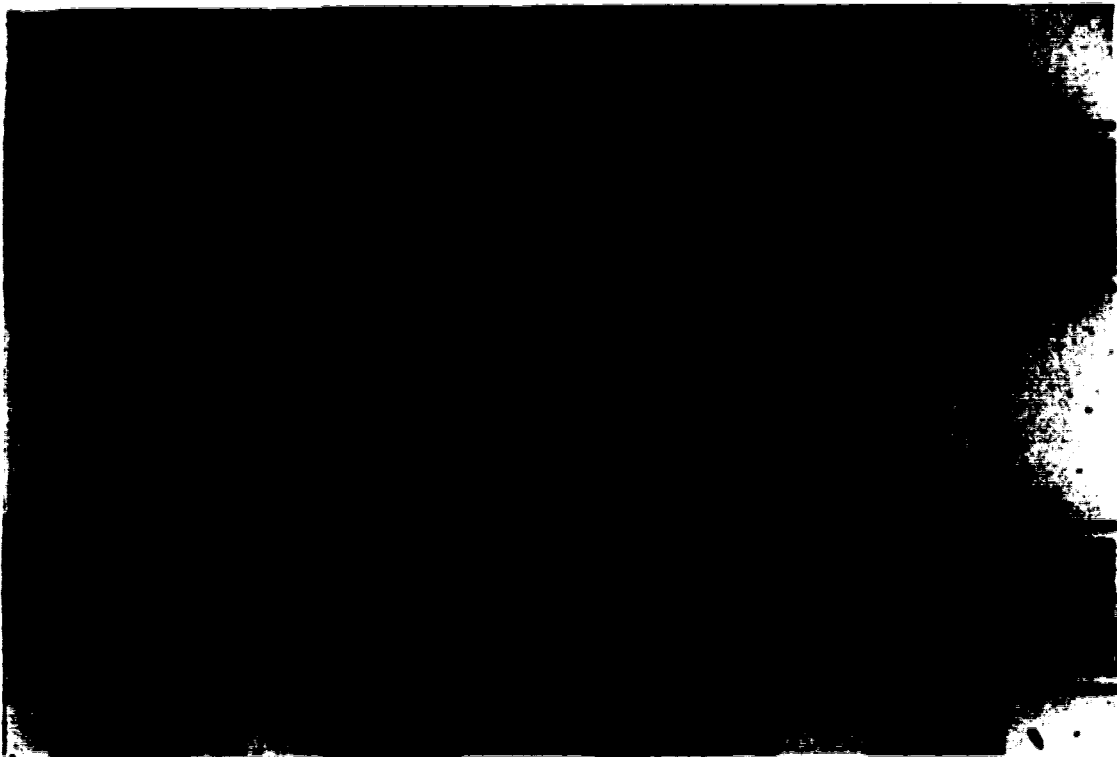


**Figure 3.4 Monolithically Integrated Photoconductors.**

The major drawback of epitaxial photoconductors is their low dark resistance which is in the order of hundreds of ohms. This low dark resistance causes serious noise problems as well as contributing to undesirable level-shifting in crosspoint switching between the on and off states. The high dark current in the on-state generates a DC signal pedestal that can be a few orders of magnitude larger than the AC signal. This high level could saturate the receiver if

the crosspoints are switched on and off at a fast rate, as well as submerging the information signal.

One way around this problem is to take advantage of the surface depletion layer. In undoped GaAs, surface charges deplete the crystal in a region that is few micrometers thick. For photoconductors with a channel thickness of 2  $\mu\text{m}$  or less, the entire channel is depleted down to the semi-insulating substrate on which it is grown [47,48]. Furthermore, the characteristic absorption depth for GaAs at a wavelength of 780 nm is in the order of 1  $\mu\text{m}$ , which indicates that most of the light is absorbed in this thin channel. A dark resistance in the tens of  $\text{M}\Omega$  is measured for surface depleted photoconductors having a channel length of 5  $\mu\text{m}$ .

The low on-state bias, the zero volt off-state bias, the ease of integration and summation, the high expected isolation level and the high dark resistance make the surface depleted photoconductors the most promising crosspoints in the construction of a 10X10 OE switching matrix. The performance of the surface depleted photoconductors is presented and analyzed in the next subsection.

### 3.3 PERFORMANCE OF SURFACE DEPLETED PHOTOCONDUCTORS

#### 3.3.1 Bandwidth

According to equation 3.4, the bandwidth of the photoconductor is limited by the minority carrier lifetime in the GaAs channel. The lifetime varies for different doping concentration but is typically of the order of  $10^{-10}$  second for lightly doped GaAs [12]. This corresponds to a bandwidth of 1.6 GHz which is well above the target for the OE switching matrix. The gain-bandwidth product is given by:

$$\frac{r}{T_r} \frac{1}{2\pi r} = \frac{1}{2\pi T_r}$$

equation 3.5

For a drift velocity of  $2.0 \times 10^7$  cm/sec [49] and an electrode spacing of  $5 \mu\text{m}$ , a gain-bandwidth of 6 GHz is expected, which indicates a gain of 4.

The frequency response of a photoconductive crosspoint as a function of the illumination level is shown in figure 3.5. The top and bottom curves correspond to power levels of 2 mW and  $10 \mu\text{W}$  respectively. It can be seen that the measured 3 dB point is strongly influenced by the optical power level. The low frequency region of the curves flattens out as the optical power level is increased. It is found experimentally that the 3 dB point approaches 100 MHz asymptotically with very high optical power. This value is one order of magnitude lower than expected and corresponds to a minority carrier lifetime of approximately 1 nanosecond. The discrepancy between the experimental 3 dB frequency and the expected value can be explained by the extreme sensitivity of the lifetime on the doping concentration.

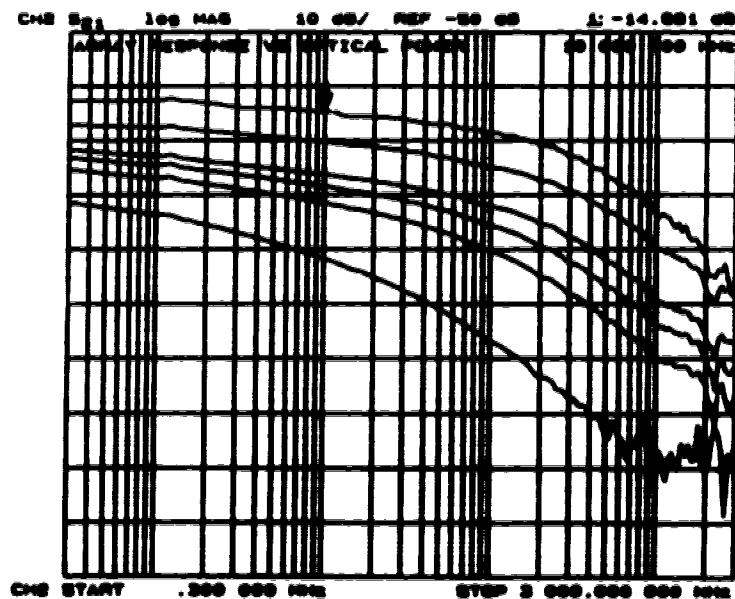


**Figure 3.5** Frequency response of an array crosspoint for different  $P_o$  ( $10 \mu\text{W}$ ,  $50 \mu\text{W}$ ,  $100 \mu\text{W}$ ,  $200 \mu\text{W}$ ,  $500 \mu\text{W}$ ,  $2 \text{ mW}$ ). The biasing voltage is 4 V.



The bandwidth is limited by the minority carrier lifetime and not the device's RC lifetime. The photoconductor's capacitance is calculated to be in the order of  $50 \times 10^{-15}$  Farad [50]. This value has been experimentally confirmed. This capacitance value leads to a RC limited bandwidth of over 60 GHz in a 50  $\Omega$  system.

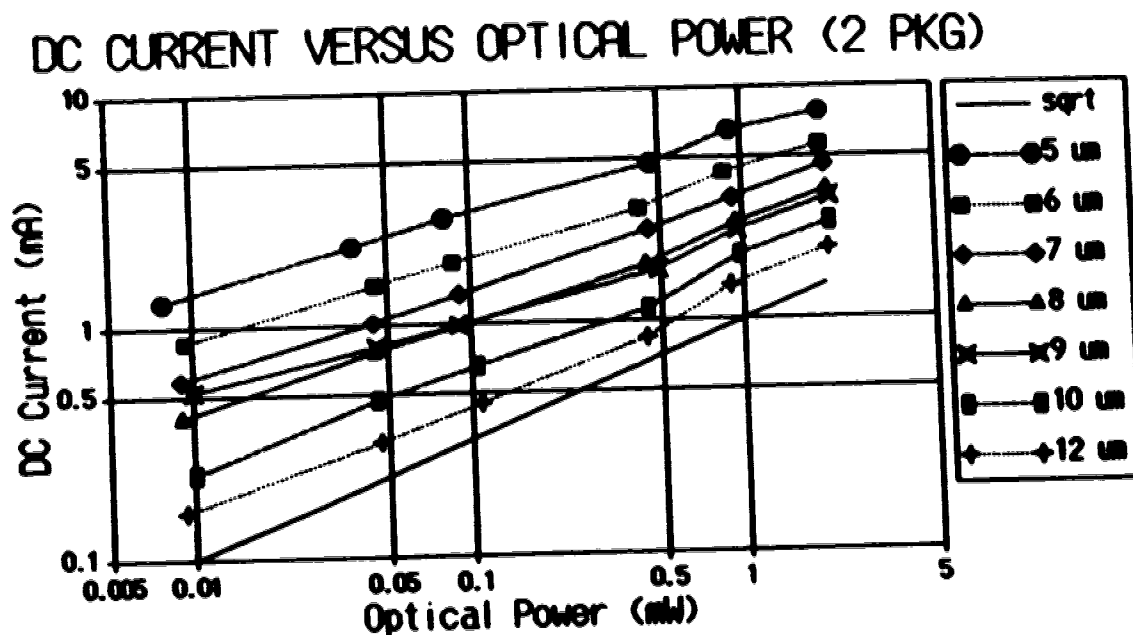


Figure 3.6 DC photocurrent against  $P_o$  for different finger spacings (5  $\mu\text{m}$ , 6  $\mu\text{m}$ , 7  $\mu\text{m}$ , 8  $\mu\text{m}$ , 9  $\mu\text{m}$ , 10  $\mu\text{m}$ , 12  $\mu\text{m}$ ). A reference  $I_{DC} \propto \sqrt{P_o}$  is also illustrated. The bias voltage is 4 V.

The DC current is plotted as a function of the optical power level in figure 3.6 for photoconductors of different electrode spacings, under a constant bias of 4 Volts. An exponential relationship of the following form seems to exist between the two parameters:

$$I_{DC} \propto P_o^2$$

equation 3.6

where

$I_{DC}$	DC current
$P_o$	Average incident optical power

From the experimental values, the value of  $x$  can be estimated to be 0.5 for most of the detectors. This value agrees with that published by Beneking in reference [51]. The square-root relationship can be explained by various trap distributions in the semiconductor's forbidden band [40,52,53] and demonstrates that bimolecular reactions are responsible for the low frequency recombination process [53,54]. This bimolecular reaction is typical of insulators or intrinsic photoconductors where the photogenerated carrier density is larger than the equilibrium carrier density.

It can also be noticed in figure 3.6 that the square-root relationship approximates more accurately photoconductors with long channels than those with shorter channels. This difference seems to indicate a field distribution related effect in the channel which is not perfectly understood. Beneking has found that a  $SiO_2$  coating layer deposited upon the channel appeared to give a closer agreement with the theoretical square-root relationship [51].

The trap distributions in the semiconductor's forbidden band could additionally be responsible for the dependence of the frequency response on the optical power level. The response speed of photoconductors is generally determined both by recombination and by trapping processes. This can be understood qualitatively by looking at the two extreme cases.

At low optical power intensities, the hole and electron quasi-Fermi levels are close to their equilibrium positions and, in a n-type channel, most energy states in the forbidden gap act as hole trapping centers [40] which then leads to a

slow response time. The slow response is due to the fact that a trapped hole will probably be re-emitted to the valence band before recombining with a free electron and the recombination process will mostly involve band-to-band transitions which are unlikely because of the multi-phonon process involved [53]. This explains the large low frequency response.

On the other hand, at high optical power levels, the hole quasi-Fermi level is now close to the valence band, making most energy states in the forbidden band recombination centers for both electrons and holes [40,51]. These recombination centers have a larger capture cross section than the free carriers, and the recombination process will involve recombinations through recombination centers. This phenomenon is equivalent to filling all the trapping centers and making their presence unperceived [54].

The total analysis of the photoconductor behavior for moderate power intensities is quite complex and involves many coupled nonlinear differential equations as well as the knowledge of the state distribution in the forbidden gap.

The relationship between the current amplitudes and the optical power levels are illustrated in figure 3.7 for 3 different frequencies. The gain at low frequencies is high because of the long minority carrier lifetime due to traps. At high frequencies, however, slow recombination processes do not contribute to the response and the gain is determined by the fast component of the carrier lifetime. This lifetime is governed by fast recombinations through recombination centers as it can be seen by the linear relationship at 100 MHz.

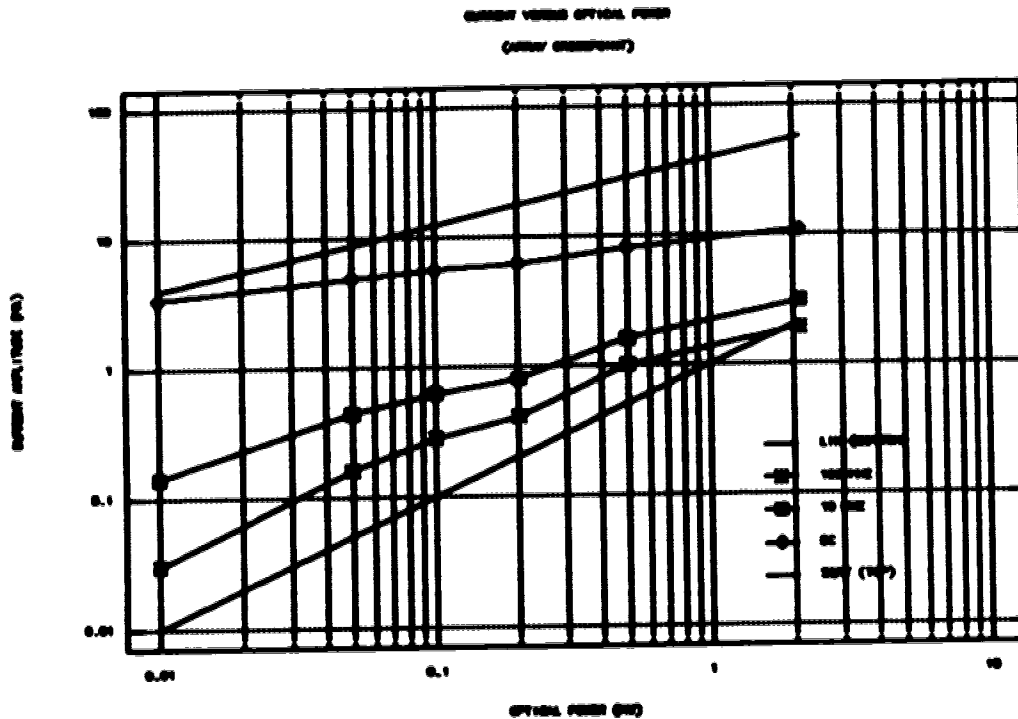


**Figure 3.7** Current amplitude against  $P_0$  at 3 different frequencies (DC, 10 MHz, 100 MHz). The reference curves  $I \propto \sqrt{P_0}$  and  $I \propto P_0$  are also plotted.

Figure 3.5 shows that the photoconductor response must be equalized. The effect of slow trapping centres is less predominant for optical power levels greater than hundreds of microwatts where there are enough recombination centres to reduce the low frequency components to approximately the same level as the high frequency components. At incident optical power levels above 500  $\mu\text{W}$ , the photoconductor frequency response can be represented approximately by a first order system having a pole at 100 MHz and can then be easily equalized up to 1 GHz. The slow slope observed at lower frequencies is harder to equalize but some tailoring is possible. The optical power requirement at the

photodetector for achieving an acceptable equalization necessitates a high power transmitter.

### 3.3.2 Responsivity

Before an attempt at equalizing the frequency response was undertaken, the responsivity  $r$  of the photoconductor was evaluated to guarantee that the value was high enough to be satisfactory after equalization. The responsivity curves for two different sets of parameters at three different frequencies (DC, 10 MHz, 100 MHz) are shown in figures 3.8 and 3.9.

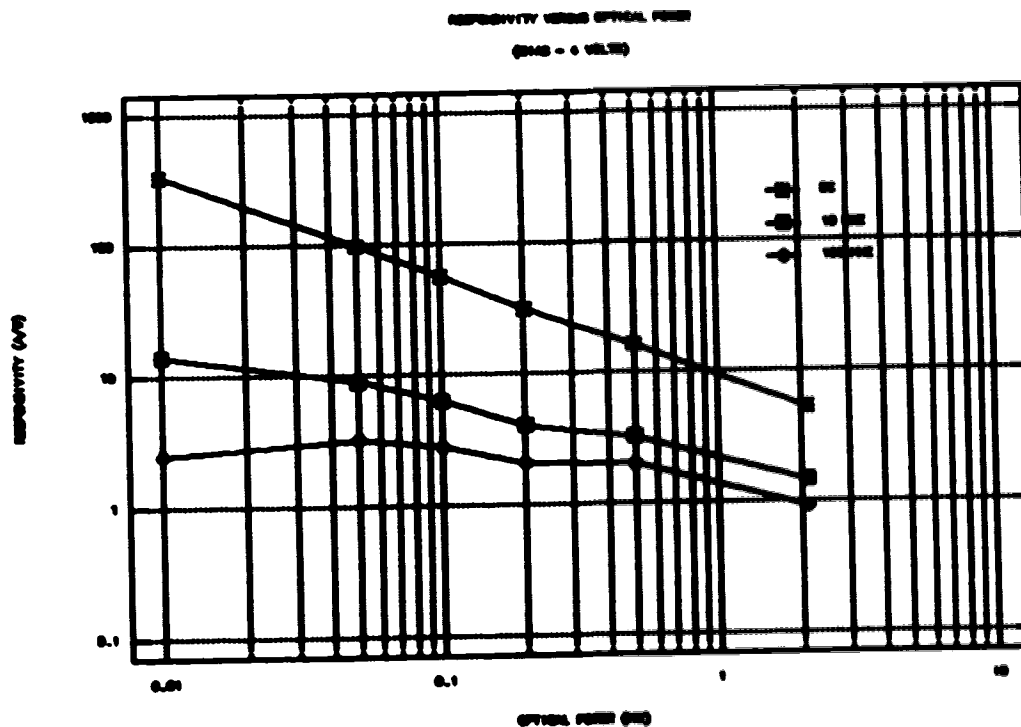
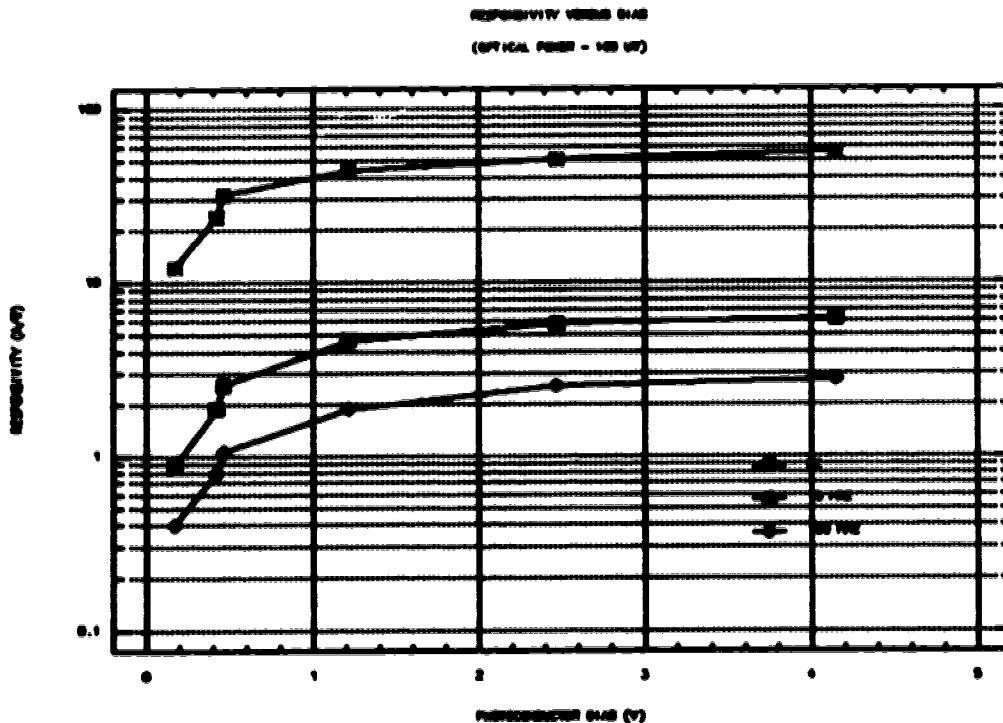


Figure 3.8 Crosspoint responsivity versus optical power level at 3 different frequencies (DC, 10 MHz, 100 MHz). The bias voltage is 4 V.

Figure 3.8 indicates that, in the carrier velocity saturation regime, the responsivity at 100 MHz varies between 2 and 3 amperes per watt in the optical power range covering  $100 \mu\text{W}$  to  $500 \mu\text{W}$ . This signifies that the responsivity after equalization would be between 0.2 and 0.3 A/W up to 1 GHz. This value is high enough to justify the use of the photoconductors with an equalization stage as our crosspoints. Figure 3.9 shows that the carrier velocity saturation regime is reached for a bias of roughly 1 volt.



**Figure 3.9** Responsivity versus applied bias for a  $5 \mu\text{m}$  channel length photoconductor at 3 different frequencies (DC, 10 MHz, 100 MHz). The optical power level is  $100 \mu\text{W}$ .

The photoconductor's dynamic resistance can be evaluated from the tangent of the I-V curve at the operating bias, where the current is given by the product of the responsivity and the optical power. The dynamic resistance was found to vary from 5 k $\Omega$  to 14 k $\Omega$ , for a 4 volt bias, and from 500  $\Omega$  to 3 k $\Omega$  at low bias. The device's dynamic resistance should be as high as possible since the resulting dynamic resistance in an OE switching matrix is the parallel combination of the crosspoints of a single array.

### 3.3.3 Isolation

The main reason photoconductors have been chosen over the MSM photodetectors as the matrix crosspoints is because of their expected high isolation. The isolation level obtained for the photoconductors is illustrated in figure 3.10 for different biasing points. It can be seen that an isolation level of more than 65 dB is achieved up to 100 MHz. The lower isolation level past this frequency is due to the instrument noise that becomes more important than the off-state response that is rolling off. This confirms the initial expectation about the device's high level of isolation. There are two factors that must be considered to achieve such a high level of isolation.

The first one is the prevention of a residual bias due to ground loops or other current loops. A residual bias of even few millivolts can reduce the level of isolation by as much as 30 dB. There are many ways to insure that the residual bias is as low as possible. These methods will be discussed in a subsequent chapter. The second factor that can degrade the isolation level is the electromagnetic coupling from the transmitters to the crosspoints at high frequencies. To eliminate this problem, shielding of the crosspoint arrays is required.

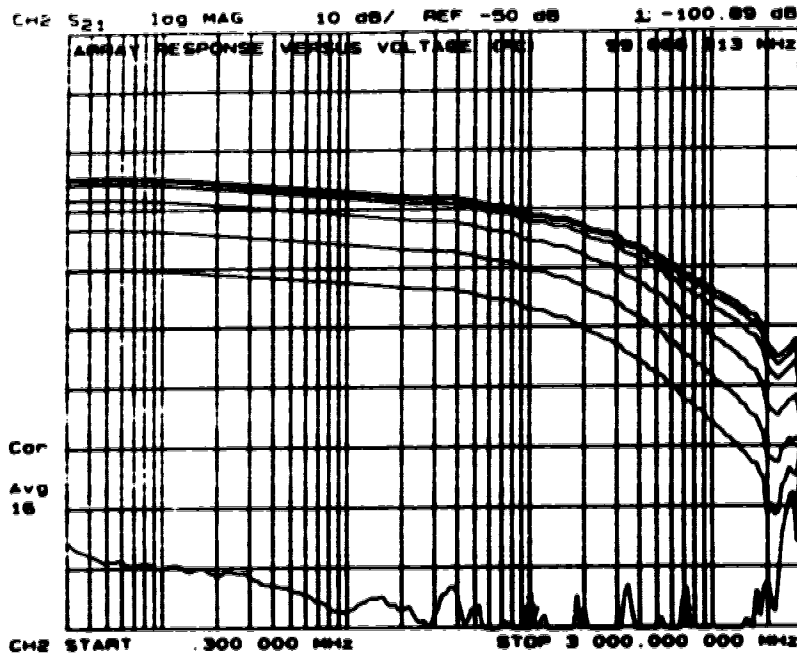


Figure 3.10 Isolation levels for different biases (0.024 V, 0.14 V, 0.48 V, 1.35 V, 2.69 V, 4.19 V). The optical power level is 0.25 mW.

Based on crosstalk alone, the extra level of isolation found with the photoconductors would potentially lead to the construction of OE switching matrices 30 to 100 times larger than what could be achieved if MSM photodetectors were used.

### 3.3.4 Noise

In a photoconductor, the most significant sources of noise are Johnson noise and photoconductor shot noise due to the recombination of photogenerated carriers. The noise equivalent circuit for a photoconductor is illustrated in figure 3.11 [54,55].  $g_d$  and  $g_p$  are the photoconductor's dark and photo-induced conductances respectively and  $c$  is the device's capacitance. In a surface-depleted photoconductor, the dark conductance is quite low and can be neglected.  $g_p$  is the inverse of the device's dynamic resistance and, as it was mentioned in section 3.3.1, is in the order of  $10^{-4}$  S.  $L_s$  and  $R_s$  are parasitic



elements and can be made negligible in a good design or can be incorporated into an equivalent load impedance. The various rms noise currents are defined below.

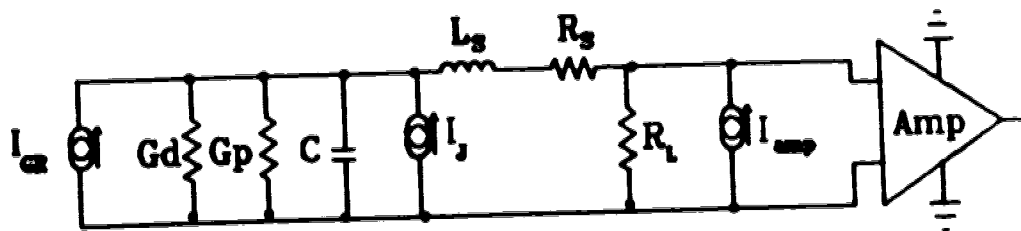


Figure 3.11 Photoconductor noise equivalent circuit.

The Johnson noise mean square current  $I_J^2$  is given by [42]:

$$I_J^2 = 4kTGB \quad \text{equation 3.7}$$

where  $G$  is the total conductance resulting from the parallel combination of  $R_L$ ,  $G_d$  and  $G_p$ . In a  $50 \Omega$  system, this value is equal to  $3.3 \times 10^{-13} \text{ A}^2$  if measured in a 1 GHz bandwidth.

The shot noise mean square current  $I_{sn}^2$  due to the generation of carriers in a trap-free photoconductor has been shown to be [45]:

$$I_{sn}^2 = 4q \frac{r}{T_r} \frac{qgF_0AB}{(1+\omega^2\tau^2)} \quad \text{equation 3.8}$$

This equation differs from the standard shot noise equation in two important ways. First, it can be noticed that at low frequencies, the shot noise is twice as important. This is due to the randomness in both generation and recombination processes which are usually assumed uncorrelated [54]. Equation

3.8 also shows that the shot noise or generation-recombination noise is frequency limited. The noise rolloff at higher frequencies is caused by emission and capture of carriers by energy states in the forbidden gap [55].

The noise properties of a photoconductor in which trapping is important are considerably more complex. In this case the noise is made up not only of the two uncorrelated generation and recombination currents, but also of the excess noise contributed by the trapping levels. Van Vliet [56] has shown that under certain conditions where only one trap level is important, the mean square current is given by:

$$I_{\text{cm}}^2 = 4 \frac{r}{T_d} \frac{qgF_0A}{(1+\omega^2\tau^2)} N_t(r) \quad \text{equation 3.9}$$

where

$$N_t(r) = N \left[ 1 + \frac{\tau_t^2}{\tau^2} \frac{(1+\omega^2\tau^2)}{(1+\omega^2\tau_t^2)} \right]$$

Equation 3.9 shows that the noise, at high frequencies, is larger in a photoconductor with traps than in a trap-free photoconductor by a factor varying from  $N$  to  $2^*N$  depending on the value of  $\tau_t$ , where  $N$  is the average number of times a hole is trapped. Furthermore, the low frequency noise is enhanced by a trapping term  $\tau_t/\tau$  where  $\tau_t$  is the lifetime due to trapping. Physically,  $\tau_t$  can be thought of as the average time a carrier spends in a trap and depends, among other things, on the density of traps and the probability of excitation out of a trap [54]. It is noteworthy that if  $\tau_t$  and  $\tau$  are of the same order,  $N_t(r)$  is then approximately equal to  $2^*N$  and the shot noise is increased by twice the number of times a hole is trapped. It is also important to note that because the trapping

kinetics depend strongly on carrier densities,  $N_c(r)$  is expected to depend on the light level.

The total noise mean square current  $I_t^2$  is given as the sum of equations 3.7 and 3.9 plus the receiver mean square current  $I_{imp}^2$ . If the trapping effects are eliminated by an optical power level that is high enough, equation 3.9 can be replaced by equation 3.8:

$$I_t^2 = I_J^2 + I_{en}^2 + I_{imp}^2 \quad \text{equation 3.10}$$

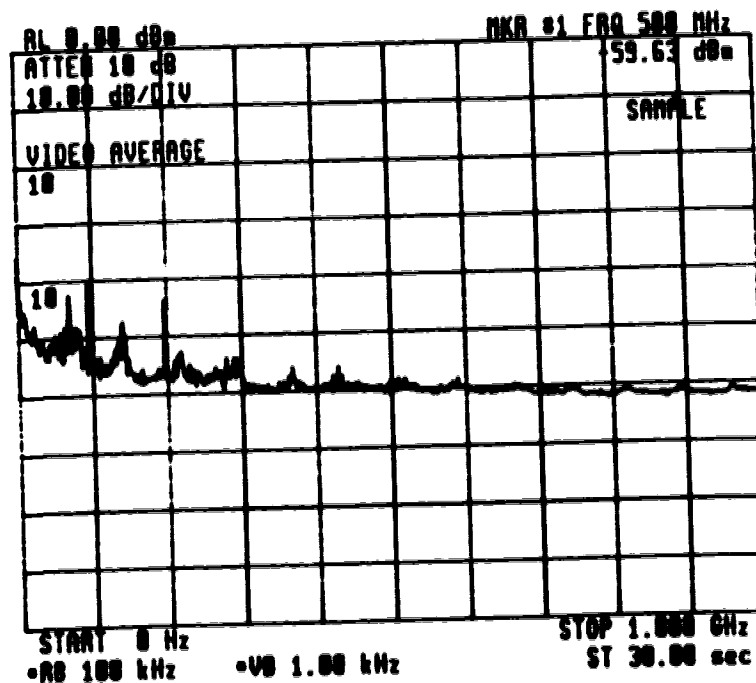


Figure 3.12 Photoconductor total noise power for a  $5 \mu\text{m}$  array crosspoint at an optical power level of  $0.4 \text{ mW}$ . The bias is  $4 \text{ V}$ .

The noise measurement of a  $5 \mu\text{m}$  photoconductive crosspoint was made at an optical power level of  $400 \mu\text{W}$  and is illustrated in figure 3.12. A wideband

amplifier was used to raise the noise level above the noise floor of the spectrum analyser, whose filter bandwidth was set at 100 kHz. It can be noticed that the noise curve is composed of two regions that correspond to the noise terms in equation 3.10. At frequencies lower than 300 MHz, the generation-recombination noise dominates and is frequency dependent. At higher frequencies, the frequency independent Johnson noise and receiver noise take over and dominate the noise processes.

It is important to note at this point that the frequency dependence for the shot noise mean square current is of the same form as the signal power frequency dependence. This will result in a noise level, after equalization, that will be mostly controlled by the Johnson noise and the amplifier noise. Assuming an effective responsivity of 0.2 A/W after equalization, a 400  $\mu$ W optical power level, a 50% modulation index and a 6 dB receiver noise figure, the SNR for a matched 50  $\Omega$  impedance ( $Z_0$ ) system in a 1 GHz bandwidth can be estimated to be:

$$10 \log \left[ \frac{1/2 Z_0 (mRP_m/2)^2}{4kTB} \right] - 28 \text{ dB} \quad \text{equation 3.11}$$

This shows that the receiver will require either a front end with a lower noise figure or a higher load resistor to achieve the desired signal-to-noise ratio.

### 3.3.5 Conclusion

The surface-depleted photoconductor seems to combine, after equalization, all the necessary crosspoint requirements for the realization of a 10X10 OE switching matrix with the desired performance. It seems to offer, after equalization, a bandwidth in excess of 1 GHz, a responsivity between 0.2 and 0.3 A/W, an isolation level greater than 65 dB and a signal-to-noise ratio in the order of 30 dB.

## CHAPTER 4

### OPTICAL POWER DISTRIBUTION MODULE

#### 4.1 TYPES OF OPTICAL DIVISION

At present the optical transmitters are high cost items in an OE switch matrix. The lowest cost per crosspoint is obtained with the largest possible matrix dimension, and therefore the optical power supplied from a single light source must be distributed efficiently to the crosspoints. The available transmitter power and the minimum optical power required at the individual crosspoints to achieve the specified performance are the factors determining the maximum number of columns in the matrix. As mentioned in chapter 3, at least a few hundred microwatts are necessary at each photoconductor to achieve the desired performance. The two main factors that limit the amount of optical power at the photodetectors are the emitted power from the lasers and the splitting and excess losses of the power division. Thus, for a fixed emitted optical power, the optical division is the critical factor.

There are two methods of distributing the optical power from the sources to the crosspoint arrays. The first employs optical waveguides and waveguide power dividing devices while the other spatially divides the emitted wavefront.

The second approach could be realized either by allowing the radiation to fall upon a specially designed array of detectors or by using holographic optical elements. EM coupling problems become serious if the light falls upon an array of detectors where each of them is associated to a different electrical output and the layout of the wires is difficult. The use of the third dimension for signal distribution with holographic elements might ultimately provide a simple method of assembly. However, with available techniques, it is not practical to consider holographic

elements because they must be set above the photodetectors [57] and do not exactly constitute mechanically stable units. This prevents the construction of a compact and mechanically stable OE switching matrix.

In the guided-wave type of power division, the optical signal is transmitted and distributed from the laser to the photodetector crosspoints via optical fibres or integrated waveguides. This method is more compact and more mechanically stable than free-space division methods and has a higher coupling efficiency to the photodetector sensitive area. For these reasons, this method is chosen to split and distribute the optical power to the crosspoints of the OE switching matrix.

It is often proposed [58,59] to integrate the detectors and the waveguides into a planar integrated waveguide-detector coupler. However, this approach does not seem promising for large OE matrix using III-V material crosspoints that are sensitive at short wavelengths, such as GaAs photoconductors. It is very difficult to fabricate optical waveguides using III-V materials [60] and they are usually limited to operation as single mode components. This makes the optical coupling from the pigtailed lasers to the waveguides very inefficient. Furthermore, a good uniformity in the optical coupling from the planar waveguides to the photodetector crosspoints is hard to achieve for splitting ratios larger than two.

MacDonald *et al.* have proposed [60,61] an hybrid integration of optical and semiconductor optoelectronic elements where the photodetectors are mounted face down on an ion-exchanged glass circuit board which is used for both optical and electrical interconnections. This approach offers the advantage that both the detectors and the waveguides can be optimized independently and it solves the compatibility problem caused by the different fabrication processes. However, there exist still many difficulties in the fabrication techniques to create the perturbations required with this approach, and efficient and uniform light tapping becomes a non trivial task.

Although the full potential of an OE matrix can only be attained by an integrated optical signal distribution, multimode fibres and biconical-taper star couplers were chosen in this project, to transmit and divide the light to the crosspoint arrays. This decision was justified by the availability of the components, the good uniformity, and the low excess loss of this type of optical splitter, as well as the ease with which the components can be spliced efficiently together. The excess loss for the 1X10 biconical couplers used in this project is typically lower than 1 dB and the uniformity is usually within 0.5 dB. This leads to better results than can be realised with mixing rod optical splitters [62]. The data sheet for the biconical-taper star couplers can be found in appendix F.

#### **4.2 SPECKLE NOISE**

When coherent light sources are used in optical communication systems such as an OE matrix, the performance of passive networks can be limited by the generation of modal noise at the connecting elements. Modal noise is sensitive to the speckle pattern that is formed by the interference of the optical modes carried in a waveguide. This interference pattern takes place when the coherence time of the source is greater than the intermodal dispersion time within the waveguide [25]. Changes in the speckle pattern in the presence of mode-dependent losses lead to modal noise [63]. Devices such as biconical splitters that operate by sampling a portion of the guided modes can generate significant modal noise [64].

Speckle patterns are sensitive to temperature changes, external forces, changes in emission wavelength and the laser's coherence time. The mechanical or thermal disturbances usually occur at low frequencies while the laser's spectral fluctuations are mainly responsible for high frequency modal noise [65]. A short coherent time implies a short coherence length and this results in a reduced

fluctuation in the speckle pattern caused by interference of the coherent optical modes [25]. Modal noise considerations suggest that a multimode laser should be used as the optical source in an OE matrix where the optical paths are short. On the other hand, other considerations (optical power & spatial coherence) have led to the selection of a quasi single mode laser as the transmitter. It is thus important to verify that this choice of laser does not limit the performance of the switching matrix because of the generated modal noise.

Kawasaki *et al.* found experimentally [64] that in the case of a 1X8 biconical-taper star couplers, the signal to modal noise ratio is approximately 32 dB in the worst experimental conditions using a single longitudinal and transverse mode laser. The use of less coherent light sources such as the ones employed in this project, and a more favourable environment such as the mechanically stable cabinet in which the matrix sits, should lead to lower levels of modal noise than the value found by Kawasaki.

There is also another noise consideration that can arise with the use of biconical-taper star couplers. It is the effect of the optical reflections at the fibre-detector interface back into the fibre. This can result in an optical interference phenomenon that takes place between the splitters and the interface. Figure 4.1 illustrates the noise level of a crosspoint after equalization and the peaks occurring at harmonics of 80 MHz are due to the reflections back into the fibres. This was confirmed by the disappearance of the peaks when the fibre was angled above the crosspoint. The power splitters used for this project are highly directional with a directionality of over 45 dB and the observed reflection noise peaks are buried in the overall noise, when measured in a 1 GHz bandwidth.



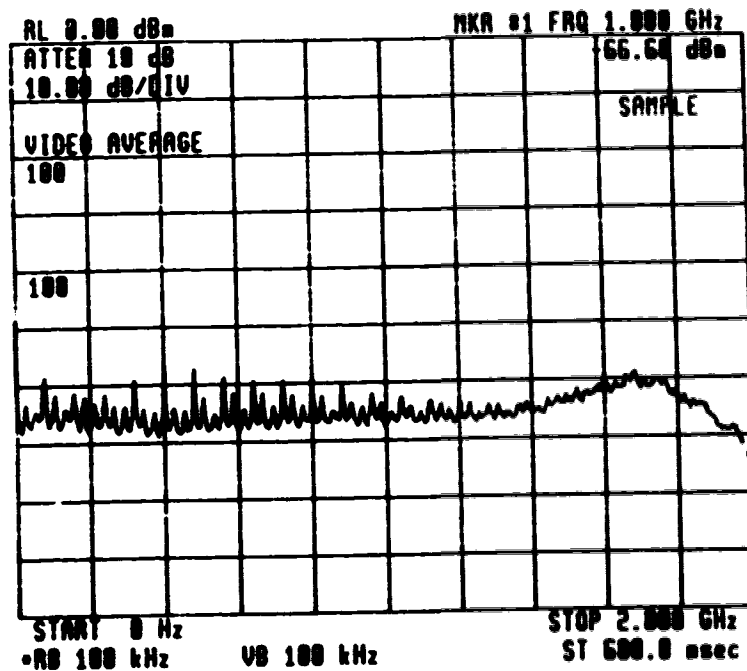


Figure 4.1 Noise peaks due to the reflections back into the waveguide at the fibre-detector interface.

#### 4.3 MECHANICAL ASSEMBLY

The connection between the pigtailed lasers and the input of the biconical-taper star couplers was realized by splicing the two fibres using a Norland UV cured optical splice tube. This splice tube allows for an easy alignment with low losses, typically 0.3-0.5 dB, and protects the brittle connection by acting as a shield. From the 5 mW of optical power available at the pigtailed laser outputs, the power levels obtained at the splitter outputs with such an arrangement are in the order of 400  $\mu$ W, which illustrates the low losses that can be achieved at the splice and at the splitter.

To ease the mechanical integration of the biconical-taper star couplers in the OE switching matrix, the power splitting devices were mounted on a 6U size card in two groups of five and installed in the transmitter card frame. This arrangement is shown in figure 4.2.



**Figure 4.2** Biconical-taper star couplers mounted on a card.

With the use of biconical-taper star couplers as optical splitting elements, the alignment of the resulting one hundred fibres with the crosspoints becomes a difficult task. This problem was solved by attaching the fibres to the detector arrays in groups of 10. The fibres were pre-aligned in Si V-groove arrays with a spacing equal to the distance between the crosspoints where one fibre from each coupler is mounted in each of the 10 V-grooves. The short bonding pads designed for the crosspoint array shown in figure 3.4 prohibit the simultaneous use of two Si V-grooves on the same array. This forced the use of two sets of detector arrays where only half of the crosspoints are actually used on each chip. The capacitance of each array (0.5 pF) is low enough to permit this non-optimized configuration without seriously penalizing the desired 1 GHz bandwidth if the load

resistance is lowered. This approach degrades somewhat the noise performance of the matrix.

The fabrication steps for the realization of the Si V-grooves are described in appendix B and the resulting product is illustrated in figure 4.3. The grooves are  $150\ \mu\text{m}$  wide and spaced  $200\ \mu\text{m}$  apart so that the fibres are contained within the grooves up to their midpoints. The Si wafer used is typically  $400\ \mu\text{m}$  thick and is diced to make chips that are 2 mm by 3 mm. This size of chip allows for easy alignment of the fibres into the grooves as well as structural strength.

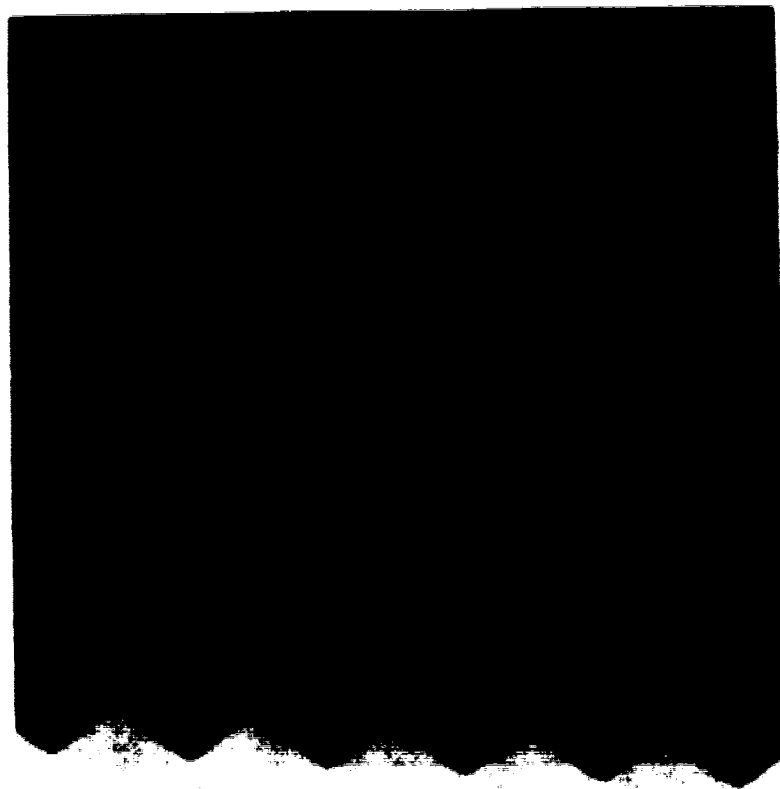


**Figure 4.3 (a) Etched grooves in a silicon wafer.**

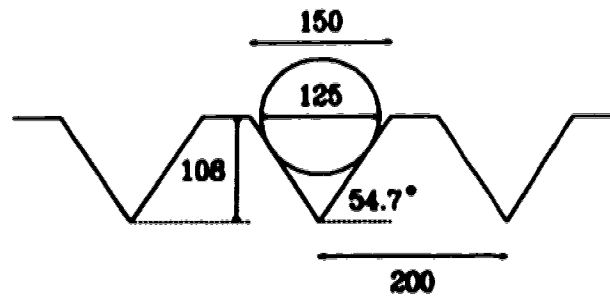


Figure 4.3 (b) Schematic of the fibre's position in a groove (distances are in  $\mu\text{m}$ ).

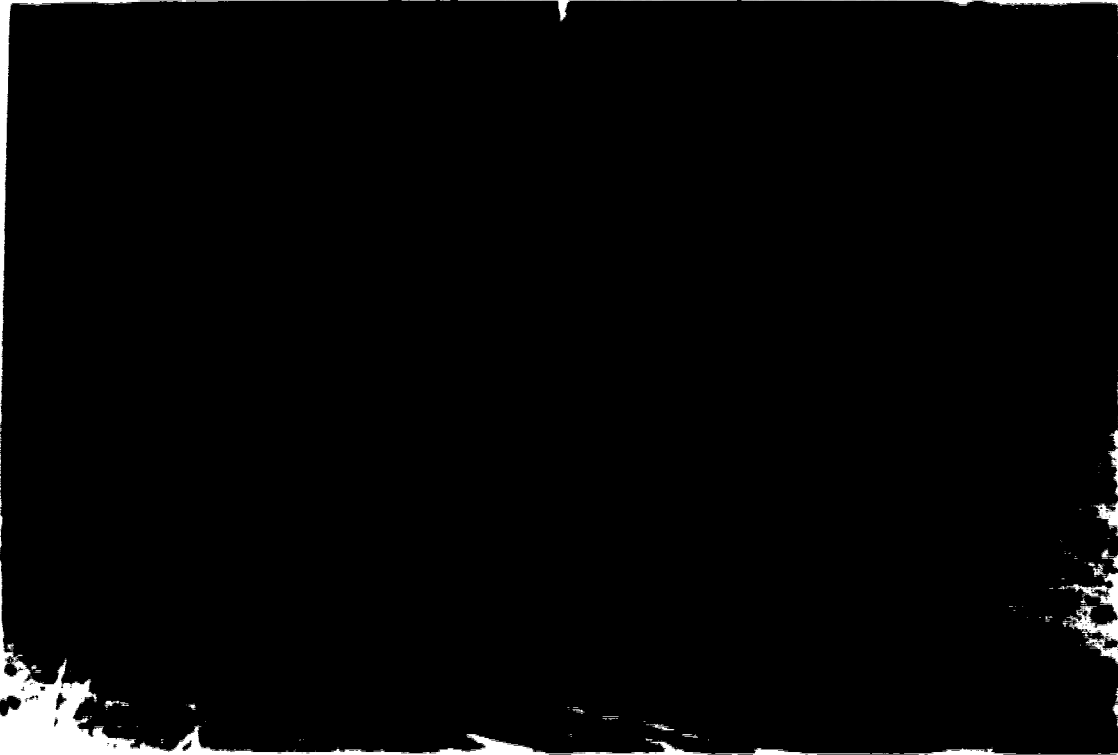


Figure 4.4 V-groove alignment set-up.

The V-grooves are mounted directly in a vertical position onto the photodetector arrays. The positioning of the chip is achieved by using the mounting jig shown in figure 4.4, which is connected to a vacuum pump and

attached to a micropositioner. The micropositioner and a goniometer, supporting the detector array, are used to align the chip. The chip alignment is monitored by optimizing the level of reference signals at two different frequencies that are injected into the two end fibres by modulating the corresponding transmitters. The monitoring was done with an RF spectrum analyser. Once the signal coupling of the reference tones is optimized, the chip is secured in place using a transparent low shrinkage UV cured epoxy. The optical uniformity at the crosspoints of a single array was measured to be typically within 1 dB.

The epoxy is also used to encapsulate the array/chip assembly to form a relatively strong unit, in which the wire bonds connecting the crosspoints to the outside world are also protected. In addition, the transparent epoxy allows for better optical coupling to the crosspoints by forming an index matching layer which lowers the Fresnel reflection coefficient at the epoxy-GaAs interface. The Fresnel reflection coefficient is expected to be reduced from 0.32 to 0.17.

## CHAPTER 5

### RECEIVER MODULE

#### 5.1 RECEIVER REQUIREMENTS

Since the frequency response of the photodetectors is dependent on the incident average optical power, the design of the amplifier & equalizer module depends on the optical power distribution network. The frequency response of an array crosspoint for different biasing voltages, using the optical output from one of the biconal-taper star couplers, is illustrated in figure 5.1. The response is relatively flat in the frequency region covering 1 MHz to 100 MHz and rolls off approximately as a first order system for frequency greater than 100 MHz.

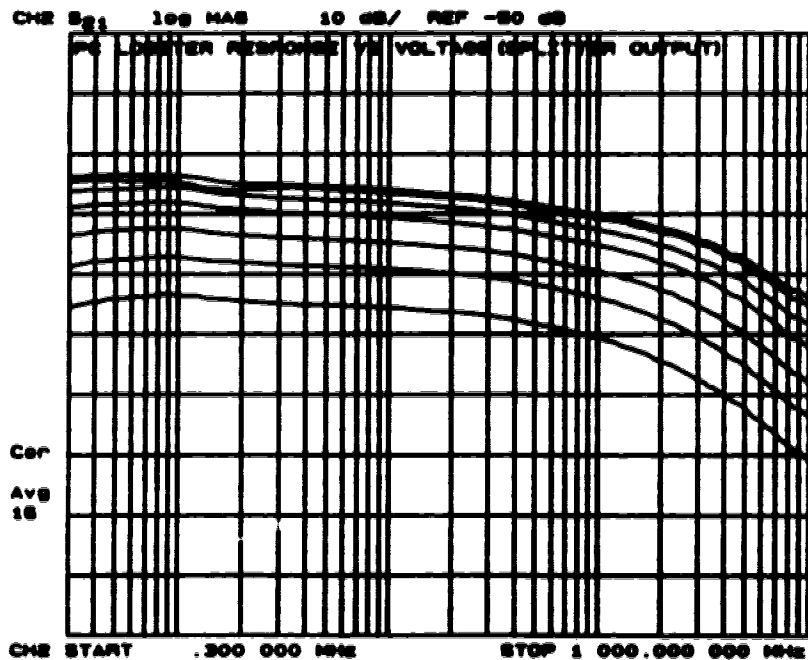


Figure 5.1 Photoconductor response using a splitter output at different bias voltages (0.12 V, 0.33 V, 0.45 V, 1.05 V, 1.56 V, 3.04 V and 4.61 V).  $P_o$  is roughly 0.4 - 0.5 mW.

The required equalization stage is essentially a differentiator that operates between 100 MHz and 1 GHz and whose equalization range is approximately 15-16 dB. Furthermore, to bring the 1 GHz signal back to its original power level requires amplification by more than 45 dB. To allow for a safety margin as well as the variations in the uniformity of the optical power, a gain of roughly 50 dB is established for in the design of the amplifier & equalizer module.

Three different types of optical receiver structures were investigated to meet the bandwidth and noise requirements: the low impedance front end; the high impedance (integrating) front end; and the transimpedance front end [25]. As mentioned in chapter 3, the capacitance of the two GaAs chips in parallel that form a crosspoint array is roughly 1 pF. If a typical amplifier stray capacitance of 0.5 pF is added to this value, the 1 GHz bandwidth requirement leads to the selection of a 100  $\Omega$  input impedance for the preamplifier. The integrating front end is eliminated because an extra differentiator is required in addition to the equalization stage that is already needed. Stable broadband transimpedance amplifiers with high gains and low phase shifts are very difficult to build up to the 1 - 2 GHz frequency region. The stability constraints of a transimpedance amplifier in this frequency would limit its gain to very low values. For this reason and because of the availability of commercial high gain-low noise low impedance amplifiers, the preamplifier was designed for a low input impedance.

Certain receiver design criteria have to be considered in the component selection of the low impedance front end and the subsequent stages. These include the bandwidth, the device stability, the dynamic range, an adequate gain and low noise characteristics. The block diagram of the receiver used in this project is illustrated in figure 5.2. The power levels at the block outputs were calculated at 100 MHz and 1 GHz from simulated curves and are justified later in this chapter.

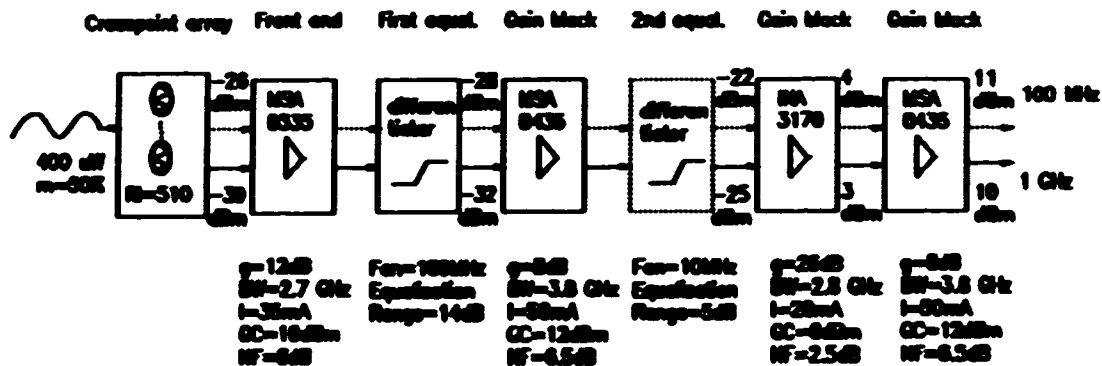


Figure 5.2 Receiver block diagram.

The abbreviations in figure 5.2 are defined as follows:

<b>g:</b>	Gain in a 50 $\Omega$ system
<b>BW:</b>	Bandwidth
<b>I:</b>	Biasing current
<b>GC:</b>	1 dB gain compression
<b>NF:</b>	Noise figure
<b>F<sub>on</sub>:</b>	Roll on frequency
<b>Eq. Range:</b>	Equalization range

The front end consists of a silicon bipolar Monolithic Microwave Integrated Circuit amplifier (MMIC) model MSA-0335. This component has a gain of 12 dB, a 50  $\Omega$  input impedance, a 50  $\Omega$  noise figure of 6 dB and a 3 dB bandwidth of 2.7 GHz. The equalizer stage follows the front-end amplifier and consists of a first-order  $RC$  differentiator with the appropriate equalization range. The following stages are 50  $\Omega$  input and output impedance MMIC amplifiers to bring the detected signal to zero dB throughput gain. It is found experimentally that a second equalization stage is required to tailor the crosspoint response in the 10-



100 MHz frequency region. This equalizer is also a differentiator but with a equalization range of a few dB (~ 4-5 dB). The data sheets of the various components used in the design of this receiver are given in appendix F.

It can be observed that the front end gain is lower than the equalization range of the equalizer which is in opposition with a basic design rule that the signal should never be attenuated more than it is amplified. This decision was imposed by stability and dynamic range constraints of the devices available at the moment of the design, but it is important to notice that this noise trade-off only occurs for the first 100 MHz, which corresponds to 10% of the total bandwidth.

The higher stability and the greater tolerance to impedance mismatches of the MSA-model MMIC family, along with amplifier dynamic range considerations have led to the proposed block arrangement. This arrangement was not designed to minimize the noise figure of the receiver but simply to achieve the necessary bandwidth within space constraints that limited the number of gain blocks as well as the complexity of any stabilizing circuitry. The whole receiver circuit had to fit in a standard 1 3/4" X 3 3/4" box which limited the number of gain blocks.

## **5.2 RECEIVER LAYOUT**

In this section, a more detailed description of the construction of the receiver is given and the choice of individual components, based on experimental considerations, is discussed.

The receiver circuit diagram and the layout of the printed circuit board on which it is mounted are shown in figures 5.3(a) and 5.3(b). The circuit consists, first, of ten photoconductors that are directly mounted on the board and bonded to their respective biasing lines. This approach reduces the size taken by the photoconductors and the length of the wire bonds which limits parasitic



reactances in the circuit. The output of each chip is thereafter connected to a common DC coupled load resistor via a short transmission line. The choice of the DC load resistor was dictated by a trade-off between noise and power dissipation considerations. Figure 5.4 shows a photoconductor chip mounted on board and bonded directly with gold wires to the copper pads.

One difficulty that arises when bonding gold wires to copper pads is the rapid and severe oxidation of the copper pads that takes place if heat is used in the bonding process. The oxidation prevents wire bonding of the photoconductors to the pads and for this reason no heat sources were used, which led to weaker wire bonds. This copper oxidation problem could be solved in the future by coating the bonding pads with a gold layer.

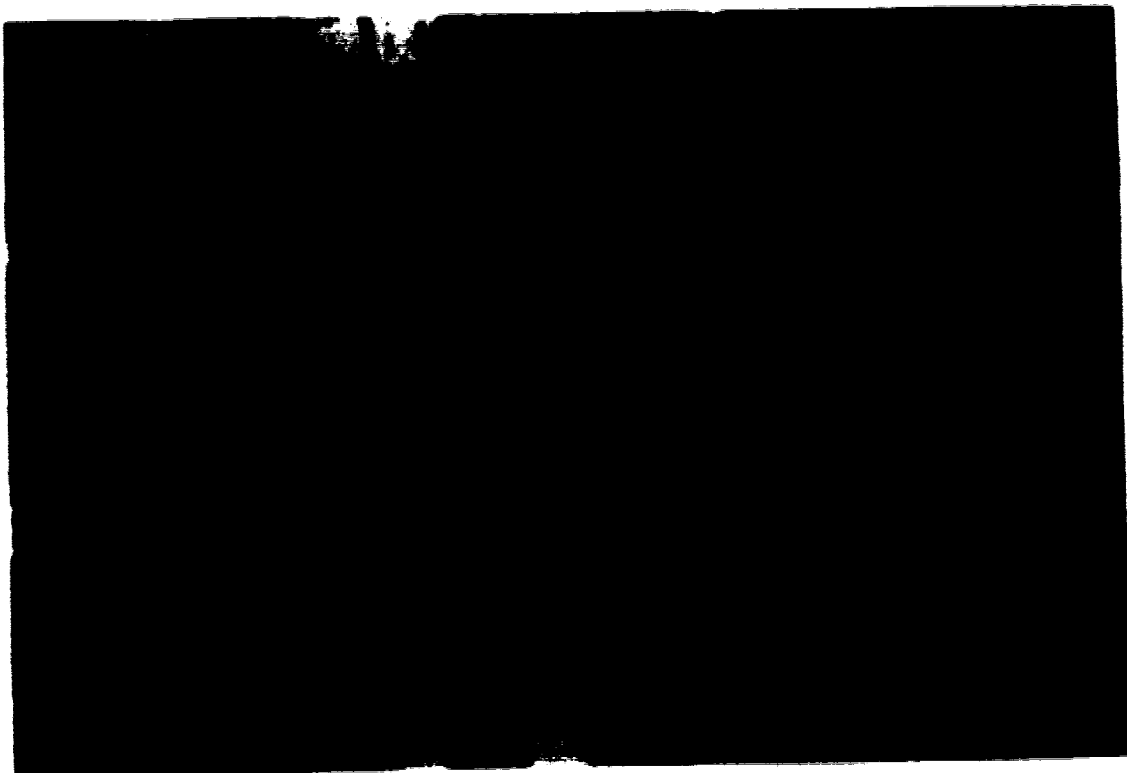


**Figure 5.4** Photoconductor chip mounted on board.

The DC current through a crosspoint in the on-state when illuminated by  $400 \mu\text{W}$  is typically between 1 and 2 mA. It was also found experimentally that 4 volts across the photoconductor constitutes a good biasing point. For TTL compatibility, the receiver was designed for five volt maximum biasing sources in the on-state. The off-state was achieved by opening the line between the source and the crosspoint. This choice of off-state configuration was selected to optimize the isolation level at the output. An off-state configuration where the source is shorted to ground could have also been used but it would have required a different arrangement at the load resistor to force the residual bias across the crosspoints to be close to zero.

A possible arrangement where the source is grounded in the off-state is proposed in figure 5.5 where the OP AMP forces the DC potential at the load resistor to be also grounded. The level of isolation obtained with this arrangement strongly depends on the offset voltage between the two OP AMP's inputs as well as the existence of ground loops. The off-state configuration where the source is open was therefore selected for its greater immunity to undesired crosstalk.

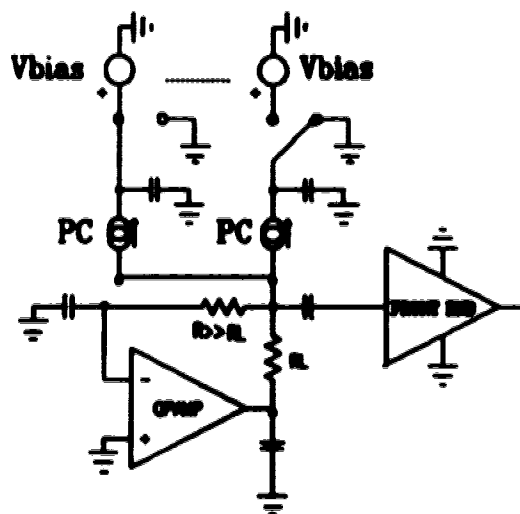


Figure 5.5 Photoconductor biasing circuit for grounded off-state.

It was intended in this project to design and build the receiver using components that are commercially available. The selected broadband gain blocks were chosen for some of their specific characteristics. The MSA-0435 was chosen for its relatively large output capability while the INA-03170 fulfilled the need for a large gain amplifier. The MSA-0335 was picked as a general purpose amplifier. The location of each gain block in the receiver layout is intended to take advantage as much as possible of these characteristics.

In the design of the front end, it is important to minimize the noise level generated by the preamplifier since it is the dominant noise source of the receiver. The INA-03170 and the MSA-0335 MMICs have 50  $\Omega$  noise figures of 3 dB and 6 dB respectively. This is equivalent to mean square noise currents at room temperature of  $i_{n,170}^2 = 3.2 \times 10^{-13} \text{ A}^2/\text{GHz}$  and  $i_{n,335}^2 = 9.6 \times 10^{-13} \text{ A}^2/\text{GHz}$ . If the thermal noise from the DC load resistor can be neglected, we observe that there is a 4.8 dB noise advantage in favor of the INA-03170. However, it was found experimentally that this type of amplifier is in practice only conditionally stable due to the emitter parasitic lead inductance that is very hard to minimize. This is a critical point since the following equalization stage does not constitute a 50  $\Omega$  function block. It would be possible to stabilize the amplifier but at the expense of the noise advantage. It was thus decided to use the MSA-0335 as the preamplifier to make the receiver design more resistant to instability.

The following stage constitutes the main differentiator equalization stage. The values of the equalizer components were found experimentally such that the best equalization in the 100 MHz - 1 GHz region was obtained. These values were mainly influenced by two factors, the source impedance of the front end amplifier and the use of the INA-03170 MMIC as a subsequent gain block. The gain of the INA-03170 MMIC increases by 2-3 dB between 1 GHz and 1.5 GHz if

the device is properly mounted and terminated. This allows for a smaller low frequency attenuation at the equalization stage.

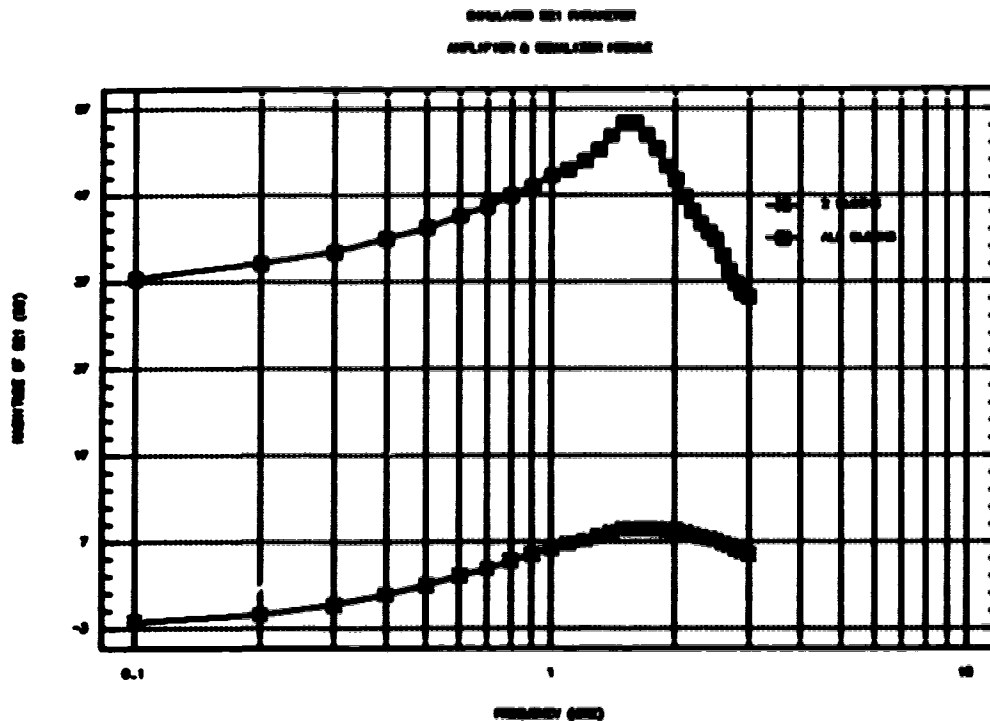


Figure 5.6 Simulated response of the S21 parameter of the amplifier & equalizer module's functional blocks terminated in a 50  $\Omega$  load driven by a flat broadband current source. Top curve: whole module; bottom curve: first 2 blocks.

Figure 5.6 illustrates the influence of the INA-03170 on the equalizer response. The bottom curve represents a simulated result of a flat wideband current source driving the first two function blocks of the amplifier & equalizer module terminated in a 50  $\Omega$  load. The top curve represents a simulated result of the whole amplifier & equalizer module driven by the same flat broadband current

source. The difference between the two equalization ranges is in the order of 8 dB. The simulation model for the amplifier & equalizer module can be found in appendix C.

The preamplifier's source reflection coefficient affects the output reflection coefficient of the device in the following manner [66]:

$$\Gamma_{out} = S_{22} + \frac{S_{12} * S_{21} \Gamma_s}{1 - S_{11} \Gamma_s} \quad \text{equation 5.1}$$

where

$\Gamma_{out}$  Output reflection coefficient

$\Gamma_s$  Source reflection coefficient

$S_{i,j}$  Scattering parameters of the amplifier

It can be seen that if the amplifier is not unilateral, i.e.  $S_{12} \neq 0$ , the output impedance, which is related to the output reflection coefficient, will be sensitive to different sources. Therefore, the equalizer response will be affected by the source impedance. This explains why the values found experimentally for the equalizer differ from the ones that would be calculated for a 50  $\Omega$  system.

The subsequent gain blocks in the receiver design were organized as shown in the circuit to take advantage of the large driving capability of the MSA-0435 and to isolate as much as possible the INA-03170 from non 50  $\Omega$  devices. The second equalizer stage was implemented to tailor the photoconductor response in the 10 - 100 MHz region and the values of the components were also found experimentally. Since its presence is only felt at low frequencies and over a very limited band of frequencies in comparison with the overall bandwidth, it does not seriously disturb the stable behavior of the INA-03170. The remaining

components in the circuits serve for biasing the receiver as well as bypassing any RF leakage from one gain stage to another such that oscillations are prevented.

Oscillations constitute a major problem in the design of high gain broadband amplifiers. Oscillations occur in a circuit when the unity loop gain condition  $-g\beta=1$  is met, where  $g$  is the gain and  $\beta$  is the feedback reverse transmission factor. This is known as the Barkhausen criterion [67]. There are two ways by which the Barkhausen criterion can be met in the receiver design presented in this section. The first one is through RF leakage via the biasing lines back into preceding gain blocks. This type of undesired feedback can be greatly reduced by efficient bypass and choke components as well as the utilization of more than one biasing line for the amplifiers.

Another way by which the Barkhausen criterion can be met is by radiation in the receiver box. The receiver box can be a resonant cavity when closed, and stationary waves associated with different modes are formed. However, the presence of the printed circuit board with metalization attached to it creates two parallel cavities whose modes are coupled. The analytical form for the resulting mode resonant frequencies in the receiver box is too complex to be solved and an experimental approach was preferred.

It was found experimentally that the minimum resonant frequency occurred at 1.2 GHz and 1.54 GHz for 5 inch and 4 inch cavities respectively. The second value corresponds approximately to the maximum gain frequency of the amplifier & equalizer module as seen from the simulated curve in figure 5.6. Oscillations could thus be maintained if a stationary wave is strongly coupled to the photoconductor wire bonds or the input of the front end amplifier.

To avoid oscillations due to coupling of radiation, the receiver box was divided into two independent chambers by a shielding wall. The circuitry was mounted on two boards interconnected with a 50  $\Omega$  mini coaxial cable mounted



through the shielding wall. It was important to seal the two chambers properly and to insure that the two boards and the mini coaxial cable were well grounded to the box, otherwise the receiver was unstable. The shielding wall was located after the second equalization stage such that the high gain part of the circuit would be housed in the smallest resonant cavity. The gains of the two sections are expected to be greatly reduced at the new minimum resonant frequencies and the risk of oscillation due to coupling of radiation is then eliminated.

The power dissipation of the final receiver is calculated to be  $15\text{ V} \times 155\text{ mA} = 2.3\text{ W}$  plus the power dissipated at the crosspoints. This last power term varies between 10 mW and 100 mW, depending on the number of array crosspoints that are biased at the same time, and is negligible compared to the power required to drive the gain blocks. Because the amplifier & equalizer module is independent of the number of rows in the matrix, the power dissipation increases only as  $N$  while the number of crosspoints increases as  $N^2$ . The linear growth of the power dissipation shows a major advantage of an OE switch matrix over other type of switching matrices.

The final version of receiver is illustrated in figure 5.7. Detailed drawings of the receiver box are presented in appendix D.

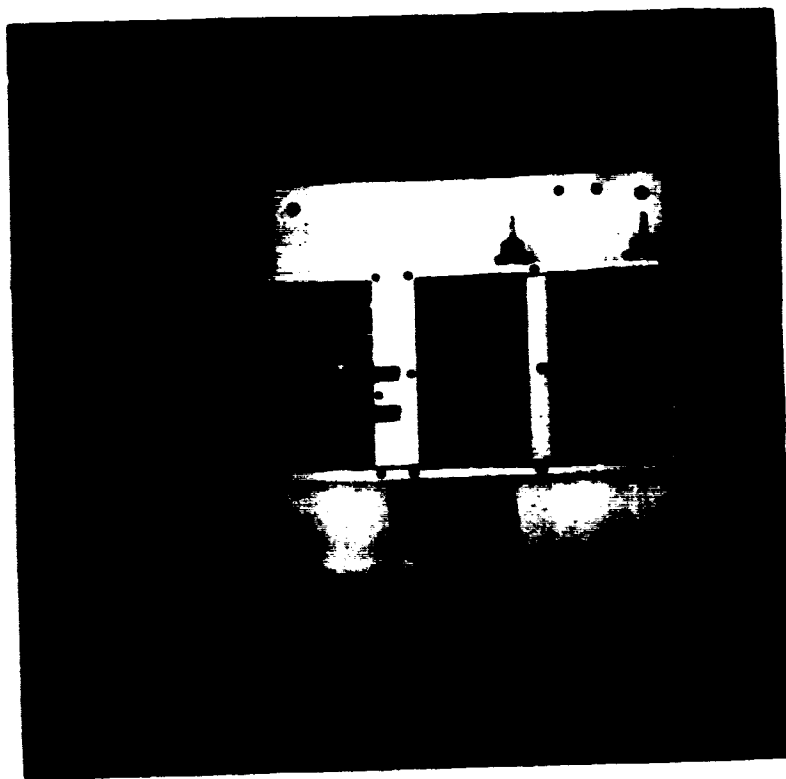


**Figure 5.7** Final OE line receiver. The two circuit boards and the shielding wall can be seen.

### **5.3 RECEIVER PERFORMANCE**

The overall frequency response from a laser transmitter to a receiver output with one crosspoint illuminated is shown in figure 5.8. The top curve illustrates the response of the equalized photoconductor in the on-state for a 400  $\mu$ W carrier modulated with a 7% modulation depth while the bottom curve is the response of the same arrangement in the off-state. This curve illustrates the efficiency of the receiver to equalize the photoconductor response and to bring the signal back to its original power level. Similar results to those shown in figure 5.8 were also obtained for an optical modulation depth of 22%. The uniformity in the response is within  $\pm 1$  dB with a gain after amplification in the order of 6 dB

rolling off at approximately 1.8 GHz. The effective responsivity of the equalized crosspoint is estimated at 0.2 A/W. The effective responsivity is calculated from the equalized signal level at the receiver's output divided by the maximum gain of the receiver.

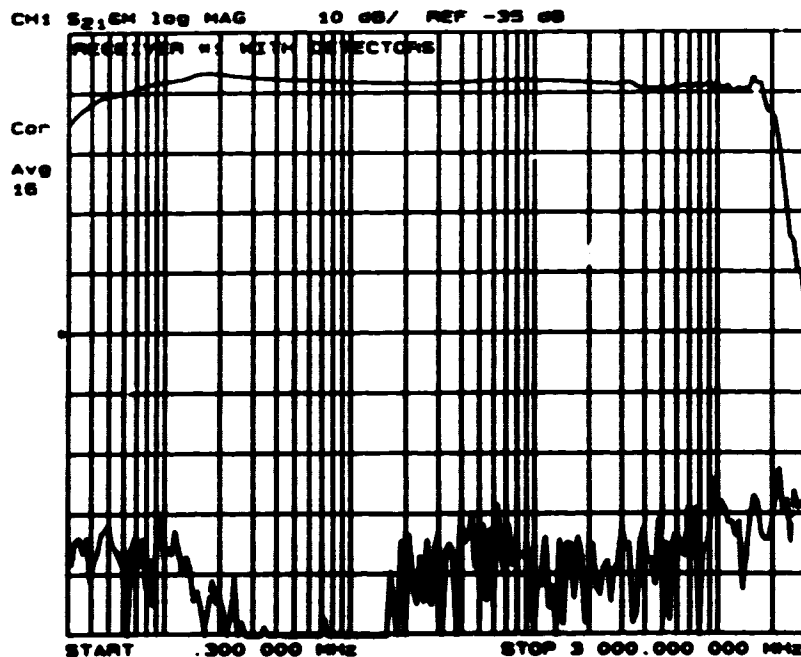


**Figure 5.8** Frequency response of an OE matrix channel with only one crosspoint illuminated.

The achieved isolation level surpasses 70 dB in the 1 MHz - 1 GHz frequency range as seen from the difference between the top and bottom curves. This level of isolation was obtained by grounding the crosspoint in the off-state. The same experiment was also done for an open off-state and the results were similar except for a slight degradation of the isolation level at low frequencies (<1 MHz).

Some peaking in the response can be noticed at 1.6 GHz. This effect is attributed to the presence of the INA-03170 gain block in the circuit (see previous

section), and its sensitivity to a proper connection of the mini coaxial cable to ground. If this connection is not properly done, strong peaking occurs which worsens the response of the system as well as its stability.

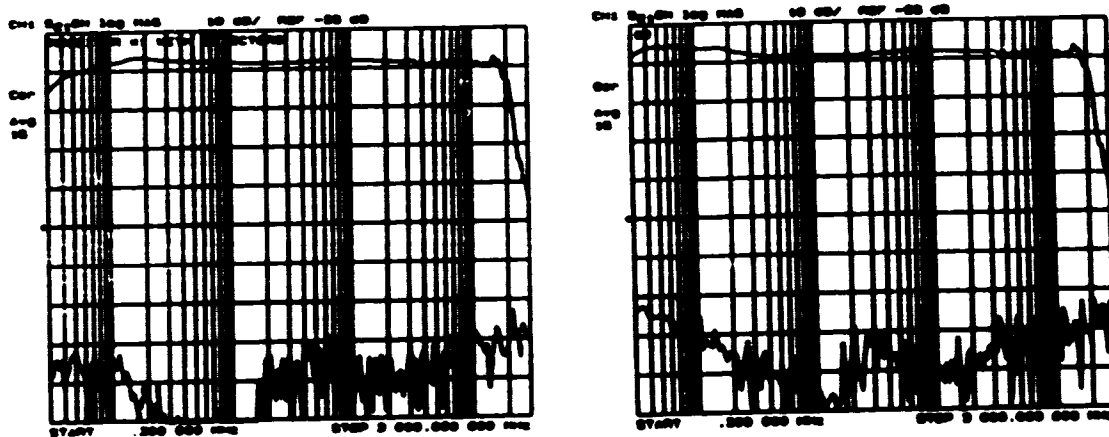


**Figure 5.9** Receiver response with one crosspoint illuminated measured at two different moments in time. The time dependence of the response at frequencies below 4 MHz can be observed.

There is a low frequency time dependent phenomenon in the photoconductor response for frequencies below  $\sim 4$  MHz that was discovered during the testing of the receivers. The response at these frequencies rises with time until it reaches a constant value and thereafter goes back down to its original value. This phenomenon can be seen in figure 5.9 where the response of the same crosspoint - amplifier & equalizer assembly is shown at two different moments in time. The phenomenon is not well understood. Traps in the photoconductive material are thought to be responsible for this peculiar behavior.

This behavior imposes the requirement that signals from the photoconductor at frequencies lower than 4 MHz be blocked by the front end so that the receiver does not saturate. The total bandwidth of the receiver with one crosspoint illuminated therefore covers the frequency range from 4 MHz to 1.8 GHz.

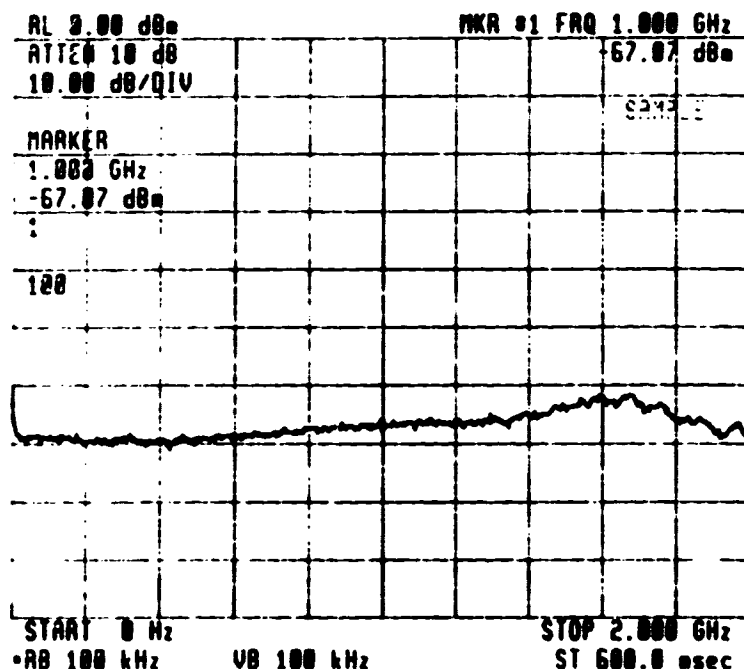
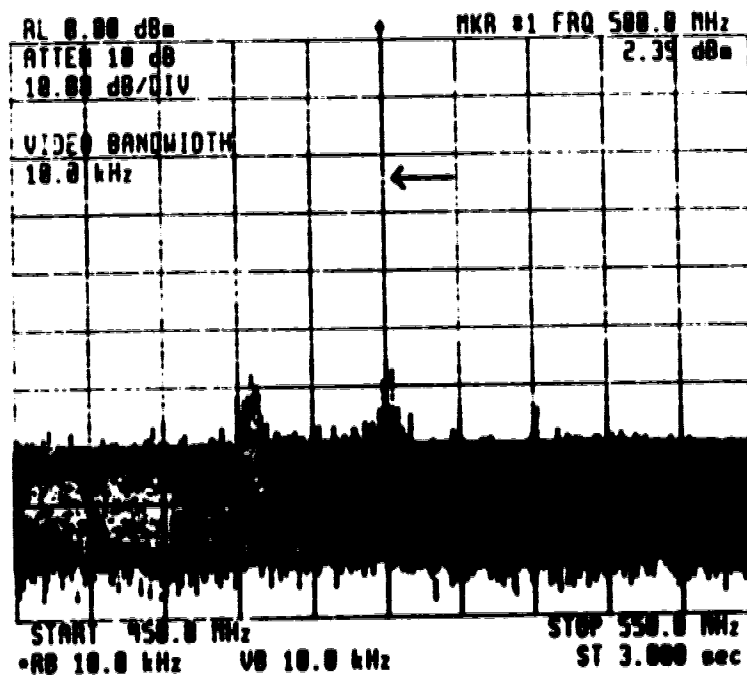


Figure 5.10 Receiver noise with one crosspoint illuminated as measured in a 100 kHz bandwidth.

The receiver noise level with one crosspoint illuminated is illustrated in figure 5.10 as measured by a spectrum analyzer using a 100 kHz filter. The flat region up to approximately 500 MHz shows that the noise in this frequency region is dominated by the equalized photoconductor shot noise. At higher frequencies, the noise is dominated by the receiver noise that increases with frequency because of the equalization stages. However, this increase is not as strong as predicted by the simulated curve presented in figure 5.6. This can be explained

by the use of a lossy cable in the experiment which was not considered in the simulation.

The signal to noise ratio obtained with a 400  $\mu$ W carrier modulated by a 500 MHz signal with an optical modulation depth of 22% is shown in figure 5.11. The figure indicates a SNR of approximately 82 dB at 500 MHz when measured in a 10 kHz bandwidth. This leads to a dynamic range of 120 dB/Hz at 1 GHz, which corresponds to a SNR of 30 dB in a 1 GHz bandwidth. The maximum SNR that can be achieved with this receiver will be limited by the signal level that will initiate saturation in the receiver.



**Figure 5.11 Receiver's SNR with one crosspoint illuminated. The optical modulation depth and the bandwidth are 22% and 10 kHz respectively.**

The receiver will saturate when the last stage (MSA-0435) must drive more than 12 dBm in a 50  $\Omega$  load, which corresponds to a rms current of 18 mA. If a maximum gain of 56 dB, as illustrated in the simulated receiver curve presented in

figure 5.6, and an effective responsivity of  $0.2 \text{ A/W}$  are assumed, this leads to a maximum modulation depth of 50%. This result is illustrated in figure 5.2 as well as the power levels at the output of each function block for two different frequency tones. With a modulation depth of 50%, the expected SNR obtained with the  $400 \mu\text{W}$  carrier should increase to approximately 38 dB. This value is higher than the one calculated in chapter 3. The discrepancy between the two results can be explained by the fact that the effective responsivity is calculated using the maximum receiver gain which occurs at 1.6 GHz while the experimental SNR was estimated at 1 GHz. The experimental SNR evaluated at 1.6 GHz can be estimated to be 28 dB which is the value calculated in chapter 3.

The receiver used in this project was designed for a specific optical power level incident at each crosspoint. As mentioned in chapter 3, the photoconductor response is strongly influenced by the amount of light that strikes the detector. It is therefore important to measure the receiver tolerance to variations in the optical power level. The receiver tolerance is displayed in figure 5.12 where the different curves represent the receiver response with one crosspoint illuminated by incident optical power levels of  $450 \mu\text{W}$ ,  $250 \mu\text{W}$ ,  $100 \mu\text{W}$ ,  $50 \mu\text{W}$  and  $30 \mu\text{W}$ . This figure shows that the designed receiver could work reasonably well for power levels as low as  $250 \mu\text{W}$  which corresponds to a 2 dB optical variation from the mean value. This represents the maximum tolerance in the optical uniformity that can be allowed while mounting the ten fibres in the receiver.

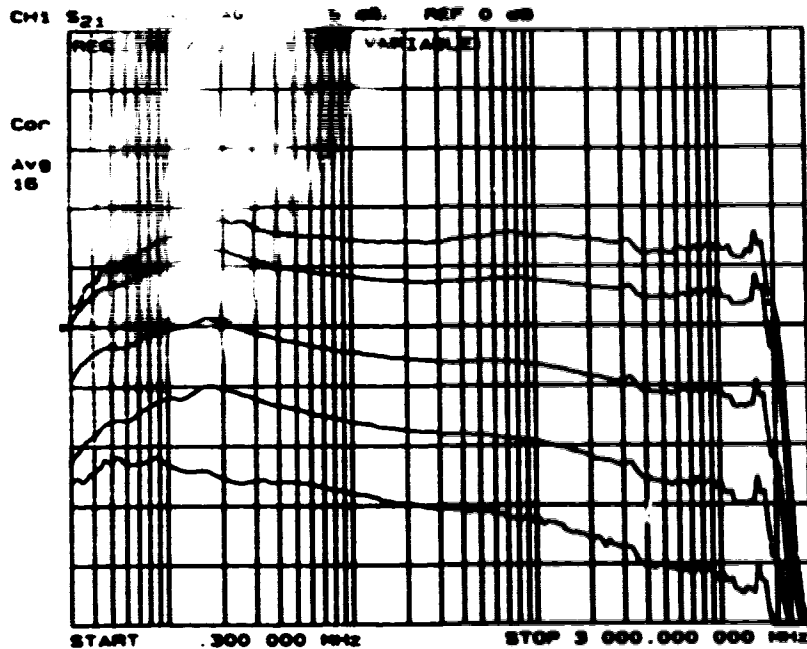


**Figure 5.12 Receiver frequency response with one crosspoint illuminated by different incident optical power levels ( $450 \mu\text{W}$ ,  $250 \mu\text{W}$ ,  $100 \mu\text{W}$ ,  $50 \mu\text{W}$ ,  $30 \mu\text{W}$ ).**

## **5.4 RECEIVER HOUSING**

The integration of the ten optical receivers into a receiver module is achieved by mounting the receiver boxes in pairs on a circuit board. The printed circuit board, which constitutes the mechanical support for the receivers, supply the power to the amplifiers and the bias to the crosspoints. A photograph of a receiver biasing card is shown in figure 5.13 and a detail schematic is presented in appendix D. The receiver biasing board, like the laser biasing board, was designed to slide and fit in a standard 6U card frame such that the whole receiver module would be composed of a standard 6U card frame and five boards. The receiver module was also designed to allow easy future connections to a backplane interfacing the matrix to a controller board that could automatically control the logical state of the crosspoints as well as the weight of the bias in the on-state.



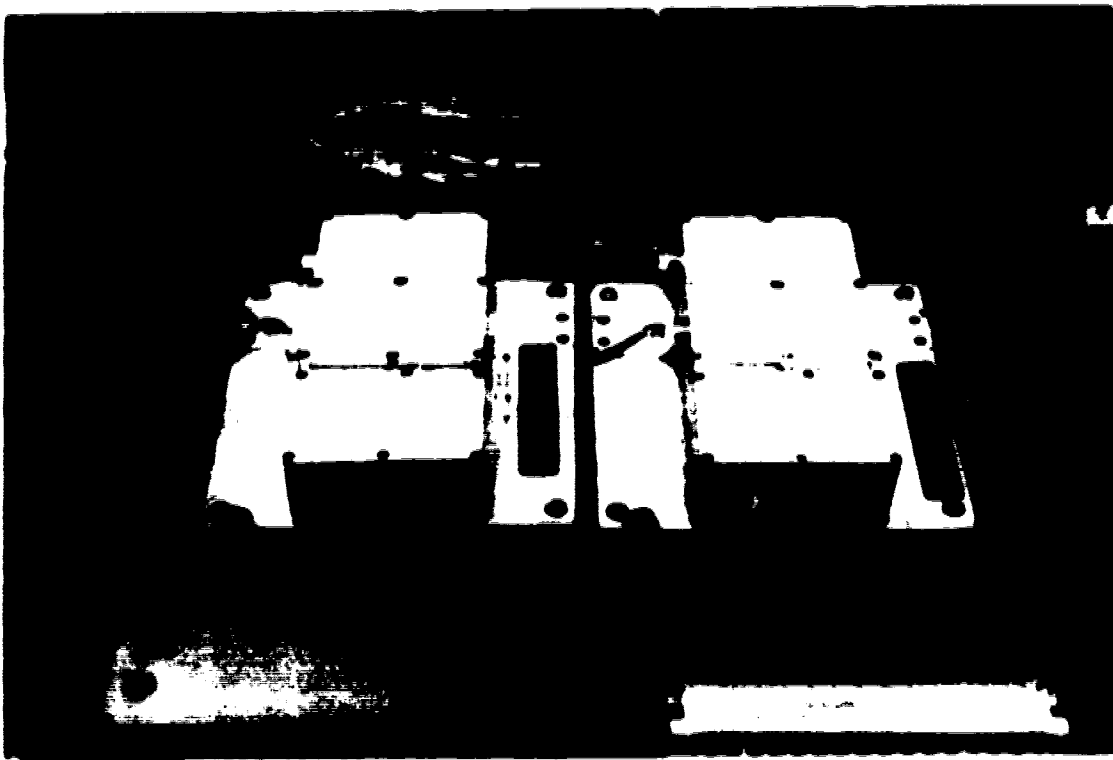


**Figure 5.13 Two receivers mounted on a receiver card.**

**CHAPTER 6**  
**INTEGRATION OF THE FUNCTIONAL MODULES**

**6.1 HOUSING OF THE FUNCTIONAL MODULES**

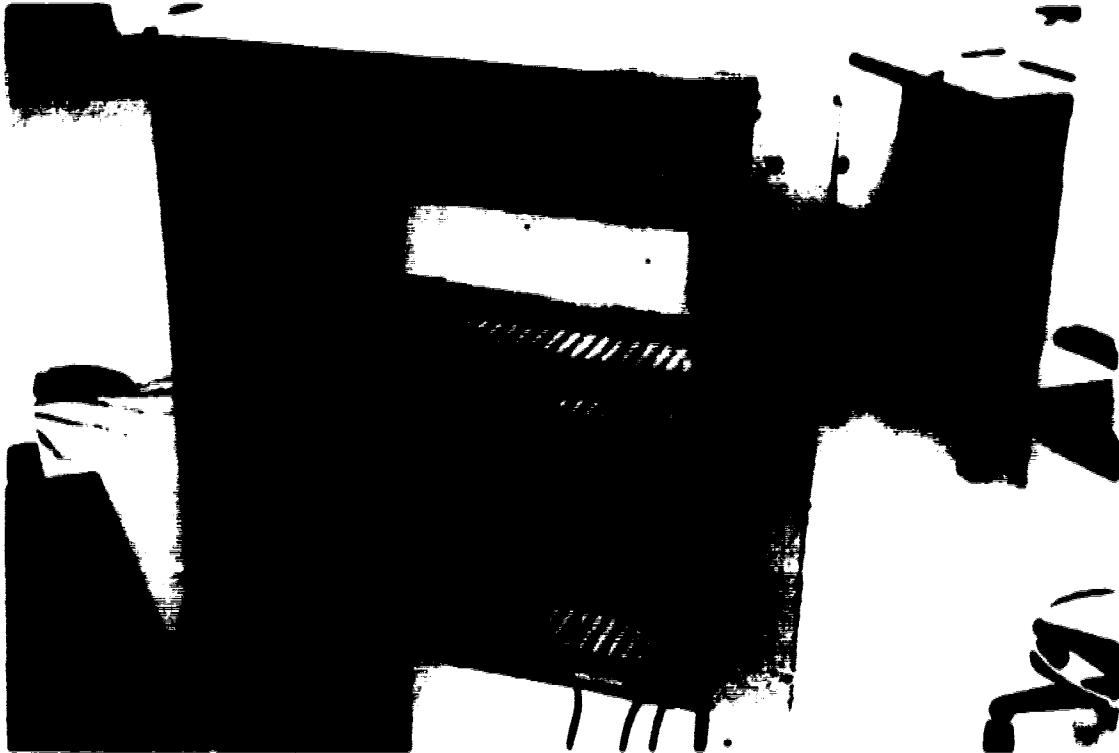


**Figure 6.1 Housing rack for an OE switching matrix.**

The final task consists in integrating the modules into a working unit and characterizing the matrix. The transmitter module and the biconical-taper star couplers as well as the receiver module are mounted in 6U card frames. The two card frames are installed in a rack that also contains the transmitter fan, the power supplies and room for a future control module. The control module will be interfaced to the matrix via a connecting backplane at the back of the receiver

card frame. This control module is presently at the development stage at the ATRC. The control module will be interfaced to a computer and the state selection of a crosspoint will be done via a mouse driven screen display.

The whole rack measures approximately 44" X 19" and is illustrated in figure 6.1. The detailed construction plan can also be found in appendix D.

The compactness in the design of the rack has imposed additional requirements on the receiver module. The small distance between the receiver cards creates short radius bends in the fibres which introduces significant stress at the fibre-crosspoint connections. This lateral stress is strong enough to break the epoxied connection between the fibre and the crosspoint if not relieved. For this purpose, two stress relief mechanisms were designed and added to the receiver boxes. A fibre support bar constitutes the first stress relief mechanism and is located exactly above the photoconductor chips. The stress is transferred from the fibres to the receiver box structure by an epoxied contact. A U shaped support bracket constitutes the second stress mechanism and is located 1 1/2" above the lid at the output end of the receiver box. The support bracket determines the fibre's radius of curvature and thus the stress applied to the fibre support bar. It also transfers the fibre's upstream stress to the receiver box via another epoxied contact.

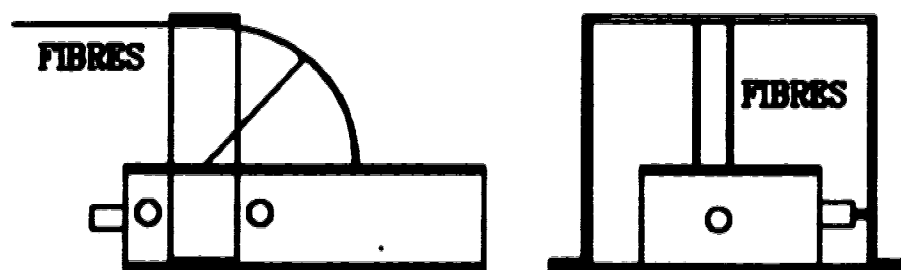


Figure 6.2 Receiver box with the U shaped bracket.

The fibre support bar can be seen in figure 5.7 and a schematic representation of the U shaped support bracket is illustrated in figure 6.2.

## 6.2 MODIFICATIONS TO THE RECEIVERS

The frequency response of the receiver presented in chapter 5 was measured with 10 active fibres mounted on the crosspoints and the result is presented in figure 6.3(a). The top curve in figure 6.3(a) represents the receiver response with one crosspoint in the on-state and all the others in an open circuit off-state, while the bottom curve was obtained with the off-state crosspoints grounded. The equalized response of the same receiver with only one crosspoint illuminated is presented in figure 6.3(b) as a reference. It can be seen from these figures that the equalization is not as accurate when the off-state crosspoints are illuminated. This loss of accuracy can be explained by the sensitivity of the first equalizer on the source impedance as expressed by equation 5.1.

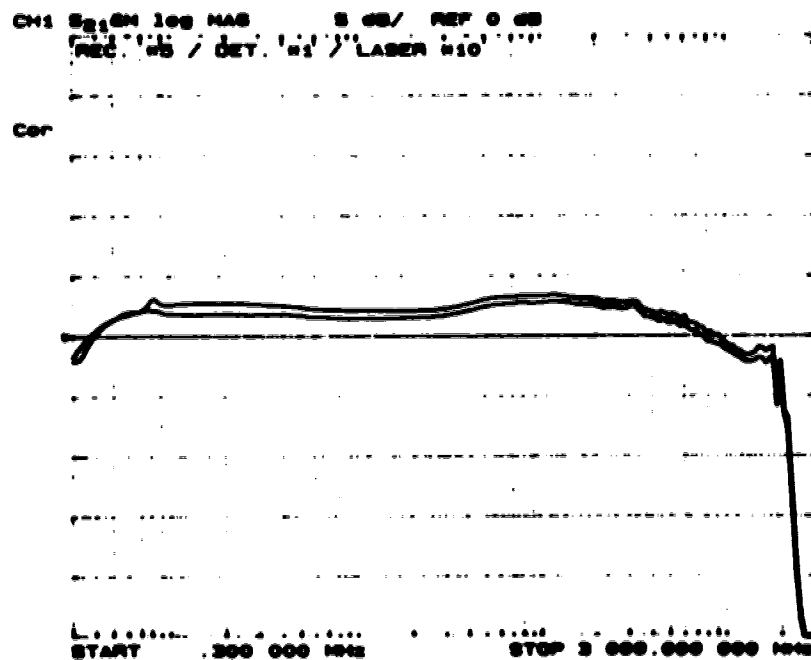


Figure 6.3 (a) Receiver frequency response with 10 fibres mounted.

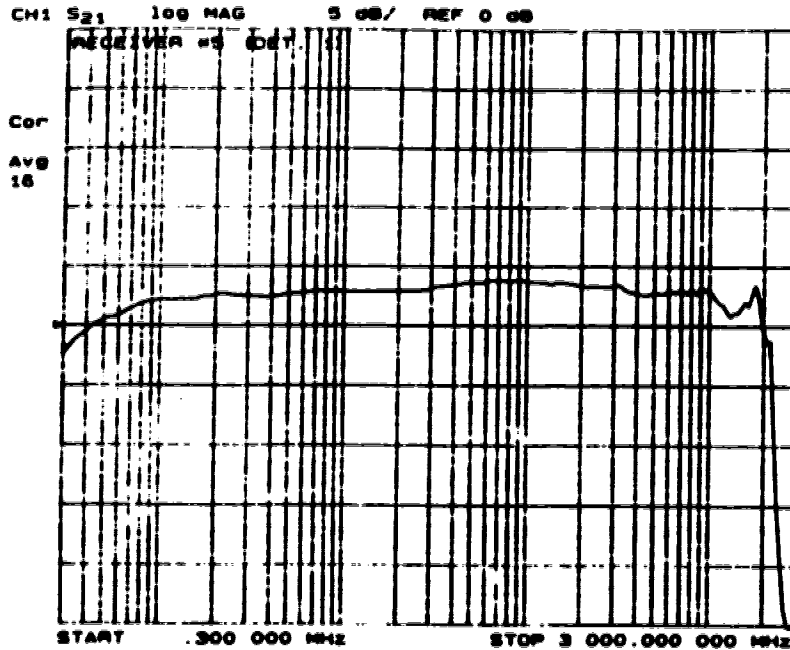


Figure 6.3 (b) Receiver frequency response with only one fibre mounted.

When in the off-state, the illuminated crosspoints have a dynamic resistance in the order of 1 k $\Omega$ , and their parallel combination results in an equivalent AC resistance of approximately 100  $\Omega$ . This reduces considerably the source impedance and may seriously affect the first equalizer's efficiency. It is also noteworthy that the dynamic resistance of the off-state crosspoints is independent of the presence of an electrical field across the device if this is smaller than the saturation field.

A third equalization stage was added to correct the small roll off between 400 MHz and 1 GHz. This equalizer follows the second one and consists of a ac differentiator whose values were found experimentally. Because of the third equalizer's small equalization range, its presence upstream of the INA-03170 amplifier does not disturb the stability of the whole modified receiver. The second and third equalizer can be seen as one function block and for this reason can be represented as one stage in the block diagram shown in figure 5.2.

Figure 6.4 shows simulated results of the amplifier & equalizer module driven by a flat broadband current source, with the photoconductor's equivalent dynamic resistance taken into account and assumed to be  $100 \Omega$ . For comparison purposes, the simulated result obtained with the amplifier & equalizer module proposed in chapter 5, where the dynamic resistance was assumed to be large, is also presented. It can be noticed that there is a reduction in the steepness of the response as well as in the equalization range when a lower source impedance is assumed. These changes in the response of the amplifier & equalizer module are enough to deteriorate the overall response of the receiver as measured in figure 6.3(a).

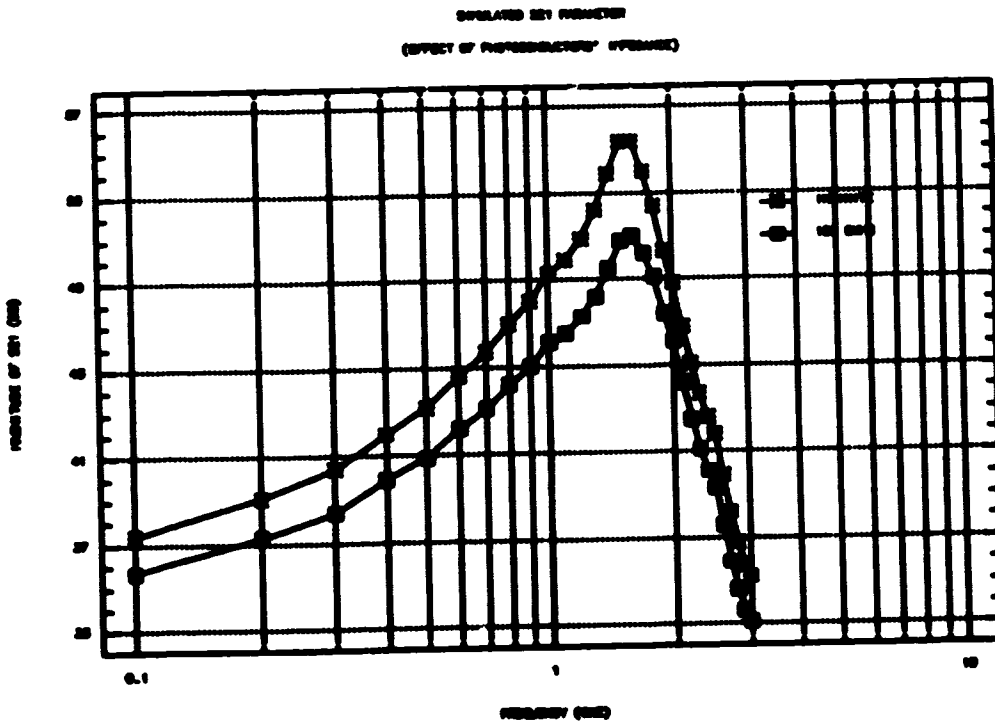
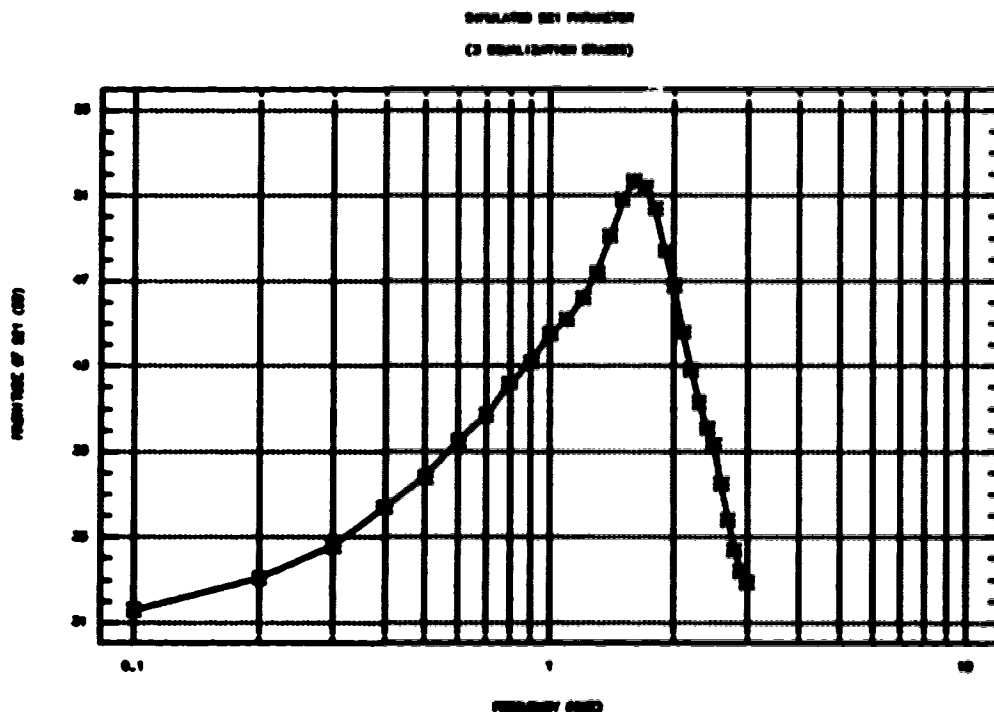


Figure 6.4 Simulated response of the amplifier & equalizer module driven by a flat broadband current source and considering the photoconductor's dynamic resistance.

The simulated response of the modified amplifier & equalizer module driven by a flat broadband current source and with the photoconductor's dynamic resistance taken into account is illustrated in figure 6.5(a). In figure 6.5(b), the photoconductor's response that needs to be equalized and amplified is once more shown and in figure 6.5(c) the actual response of a receiver with eight lasers in operation is presented . As can be observed, the implementation of a third equalizer flattens out accurately the overall receiver response past the 1 GHz mark. However due to mechanical and structural difficulties, the receiver could not be completed to accommodate ten transmitters. This point will be elaborated more thoroughly later in this chapter.



**Figure 6.5** (a) Simulated response of the modified amplifier & equalizer module driven by a flat broadband current source and considering the photoconductor's dynamic resistance.

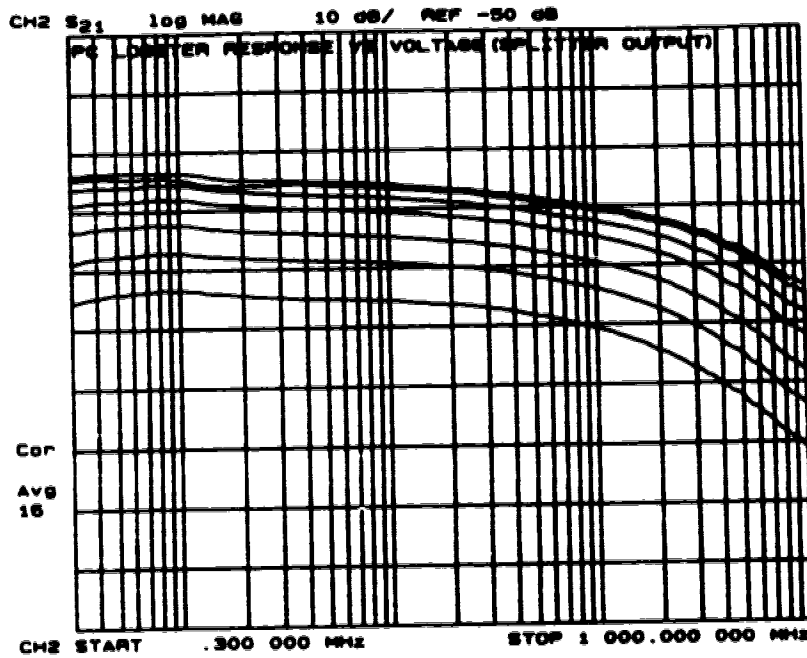


Figure 6.5 (b) Crosspoint frequency response illuminated with one output from a biconal-taper power splitter.

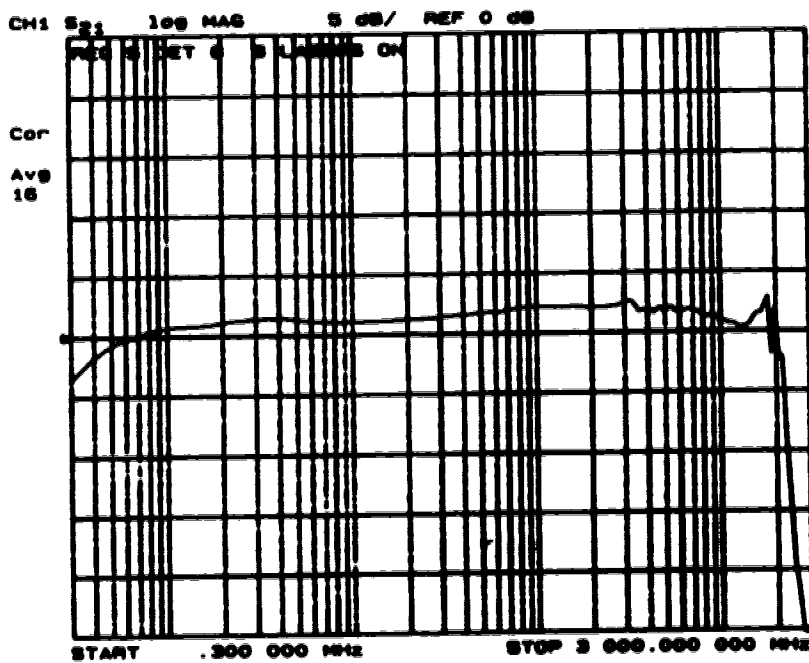


Figure 6.5 (c) Receiver frequency response using the modified amplifier & equalizer module. 8 crosspoints are illuminated.



### 6.3 PERFORMANCE OF A COMPLETE 10X1 RECEIVER

The frequency response of a complete 10X1 receiver with all the crosspoints illuminated is illustrated in figure 6.6. The top curve shows the response of an equalized photoconductor crosspoint in the on-state for a  $400 \mu\text{W}$  carrier modulated with a 7% modulation depth while the bottom curve is the response of the same crosspoint in the off-state. The off-state for all crosspoints was obtained in this experiment by opening the photoconductor biasing lines. The uniformity in the response is within  $\pm 1$  dB with a gain after amplification of approximately 2 dB rolling off at roughly 1.8 GHz. The effective responsivity of an equalized crosspoint in a complete 10X1 receiver is estimated at 0.10 A/W.

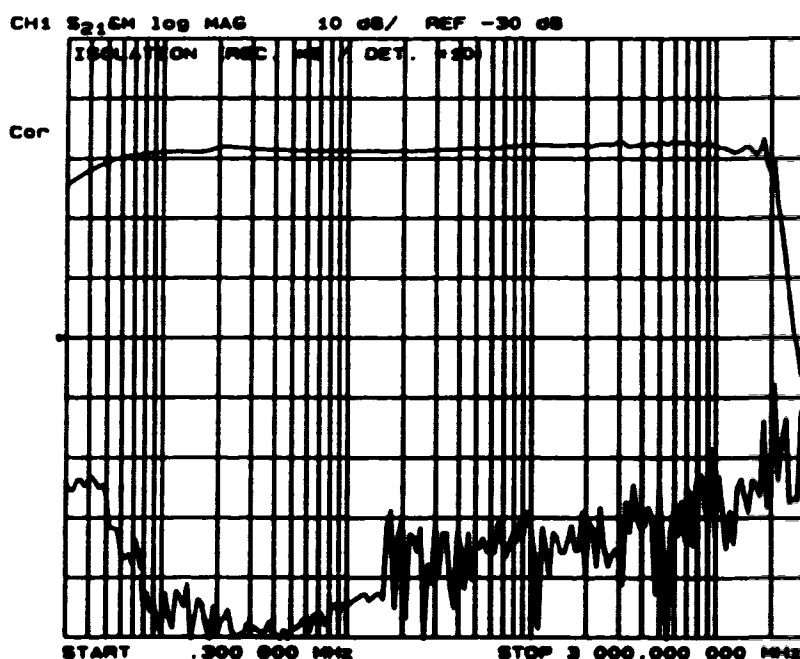


Figure 6.6 Frequency response of a complete 10X1 receiver with all the crosspoints illuminated. The two curves illustrate the isolation level.

The response level from the different crosspoints in the on-state varies from -5 dB to 2 dB. The variation could be mostly caused by a non-uniform

optical distribution since the efficiency of the equalization obtained with all the crosspoints was good. This indicates that the optical distribution was probably within the optical tolerance of 2 - 3 dB which corresponds to an electrical span of 4 - 6 dB. It was also found that the crosspoint responsivity vary from one photoconductor to the other by sometimes up to 1 dB. This difference in the response levels for various crosspoints demonstrates the requirement of the implementation of a compensation mechanism. This could be accomplished by an Automatic Gain Control (AGC) amplifier in the receiver circuit or by calibrating the on-state bias voltage of the crosspoints. The second option has the advantage that it does not depend on the crosspoint low frequency response which seems to vary with time.

The achieved isolation level for the complete receiver is over 60 dB within the 1 MHz - 1 GHz frequency range as seen from the difference between the two curves. The isolation level was degraded at certain crosspoints, but the degradation is believed to be caused by residual electric fields in the off-state. The optical crosstalk between adjacent crosspoints was also measured and the result is illustrated in figure 6.7 where the main peak corresponds to the response of an on-state crosspoint and where the other two marked peaks correspond to the response of adjacent crosspoints when in the off-state. It can be noticed that the level of crosstalk is roughly equal to the isolation level, which means that at 20 MHz the crosstalk is caused by the residual response of the off-state crosspoints and not by any optical cross-coupling. The optical cross-coupling being independent of the signal frequency, it can be concluded that the crosstalk between crosspoints of a single array is limited by the isolation level of the photoconductors.

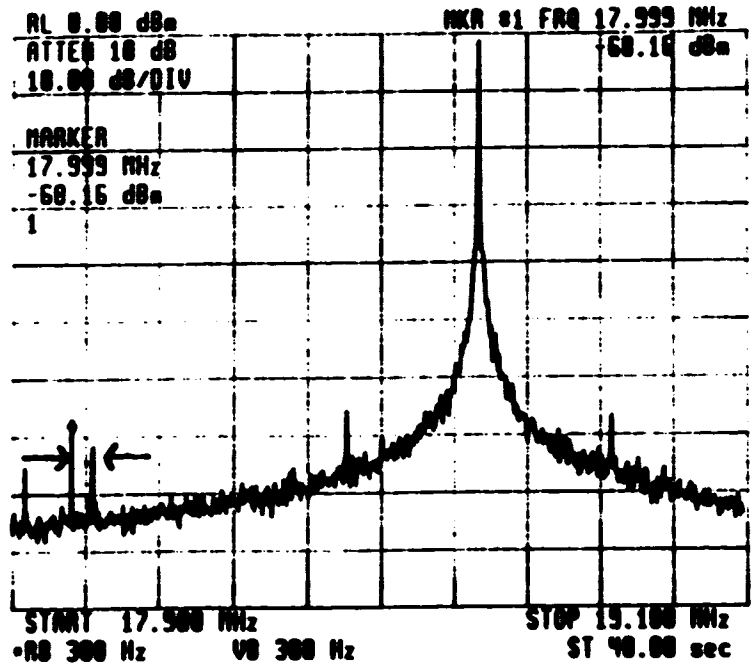


Figure 6.7 Optical crosstalk measurement between adjacent crosspoints. The crosstalk is lower than the photoconductor's isolation level.

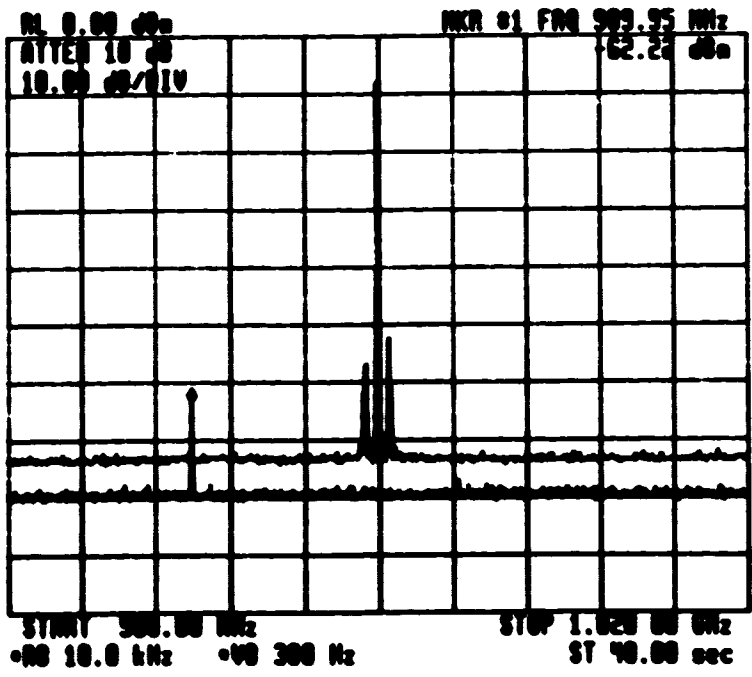
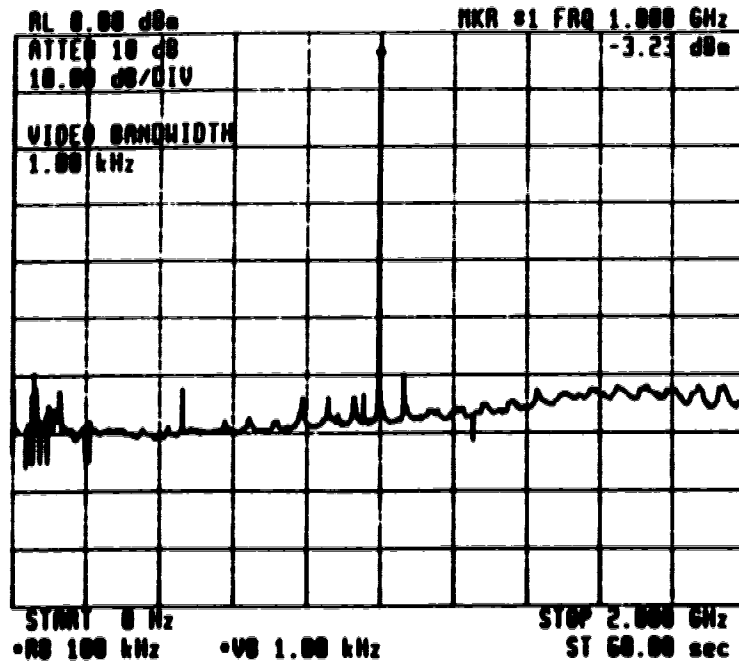


Figure 6.8 Crosstalk measurement between adjacent receivers.

The crosstalk between adjacent receivers mounted on the same printed board was measured at 1 GHz and is in the order of 55 dB as can be observed from figure 6.8. Unlike the crosstalk between crosspoints of a single array, this output side crosstalk is subject to electromagnetic coupling among the output lines. The main peak in figure 6.8 corresponds to the signal level at the output of one receiver while the weaker peak found on the lower curve is the signal picked up from the adjacent receiver. The level of crosstalk is dependent on the proximity of the two receivers and could therefore be improved.

Figure 6.9 presents the noise level of a complete receiver with all the crosspoints illuminated as measured by a spectrum analyser using a 100 kHz filter. It can be noticed that the SNR in this bandwidth is approximately equal to 65 dB for a signal whose optical modulation depth is 22%. For the same signal power, this leads to a dynamic range of 115 dB/Hz, which corresponds to a signal to noise ratio of 25 dB in a 1 GHz bandwidth. The maximum SNR that can be achieved with this complete receiver depends on the maximum modulation depth that will lead to the saturation of the amplifiers. If a maximum gain of 52 dB and an effective crosspoint responsivity of 0.10 A/W are assumed, this leads to a maximum modulation depth of 0.87. A maximum SNR of 37 dB in a 1 GHz bandwidth can therefore be achieved if the lasers are modulated with a very high modulation depth. However, harmonic distortions will start degrading the output optical signal if the laser is driven with an electrical signal whose power level is too high. To prevent signal degradation due to harmonic distortions and shortening of the laser lifetime due to overdrive, the transmitters were driven with a lower modulation depth. The signal to noise ratio of the complete OE switching matrix is thus limited by the transmitters and not by the receivers.



**Figure 6.9 Receiver noise level. The signal to noise ratio is approximately 65 dB for an optical modulation depth of 22%.**

The stability of the final receiver was predicted by simulations and confirmed experimentally. It was found that if the 50  $\Omega$  mini coaxial cable connecting the two receiver boards was properly mounted and grounded to the shielding well such that a good ground continuity was achieved, it was possible to obtain an unconditionally stable receiver.

The OE switching matrix built in this project was designed primarily to switch signals centrally so that the signal paths between the inputs and the outputs could be completed as requested. However, it is of interest to examine the behavior of the switch as a signal processing unit to confirm the foreseen potential of an OE switching matrix in this field of applications.

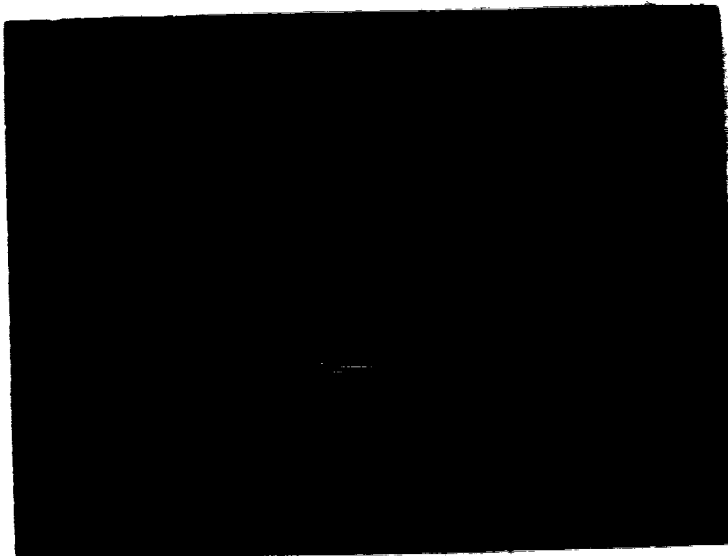


**Figure 6.10 Receiver response to a 10 kHz pulsed bias. The modulating optical signal is a tone at 100 MHz.**

The response of one photoconductive crosspoint biased by a 10 kHz train of square pulses and illuminated by a 100 MHz modulating optical signal is illustrated in figure 6.10. At this biasing rate, the presence of the crosspoint bypass capacitor can be seen in the long rise and fall time of the response which are approximately 10  $\mu$ s. A lack of isolation between the on-state and the off-state can also be observed and is probably caused by a residual electric field in the off-state, most likely due to a ground loop. Nevertheless, this experiment shows that if care is taken to avoid ground loops this OE matrix, designed to switch signals, could be used for signal processing applications where the biasing of the crosspoints could be reconfigured at a slower speed than 10  $\mu$ s.

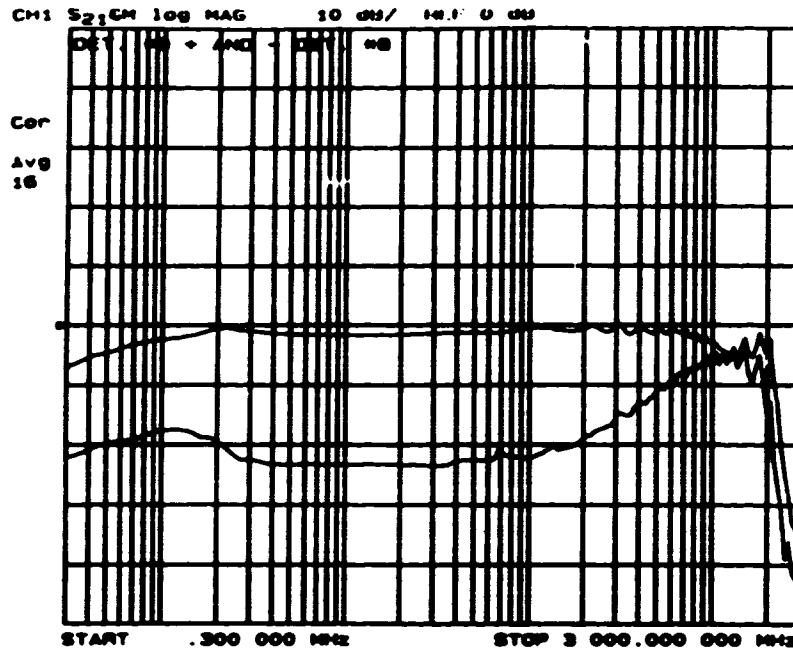


**Figure 6.11 Arithmetic functions generated by the receiver. The top curve is the summation of two signals and the bottom curve is their subtraction.**

Finally, an experiment to assess the capability of the crosspoints from a single array to accomplish arithmetic operations such as a summation and subtraction was conducted. The results of this experiment are presented in figure 6.11 where the top curve represents the response at the receiver output when two photoconductors are biased with the same polarity in the on-state, and illuminated by the same optical signal. The bottom curve was obtained using the same setup but with the crosspoints biased with opposite polarity. The delay difference between the optical signals illuminating the crosspoints can be seen from the rise in the subtraction response at approximately 100 MHz. This experiment shows that if attention is paid to minimize the delay difference between the optical signals, arithmetic operations like summation and subtraction could be accomplished with a dynamic range greater than 20 dB. This 20 dB value is

limited by the non-uniformity in the optical distribution to the crosspoints as well as the variation in the photoconductor responsivity.

The matrix capability to efficiently sum and subtract signals at the crosspoints of a single array could be useful in the fabrication of filters. The parallel combination of ring resonators in a ROSM, as presented in chapter 1, where the input signal is summed with its delayed self create a comb filter. The comb filter's Q factor depends on the ability of the crosspoints of a single array to evenly sum and subtract the delayed versions of a same signal [19]. The previous results, therefore, show that the OE switch matrix could be efficiently operated as a ROSM to create comb filters.

#### **6.4 PREMATURE BREAKDOWN OF OE RECEIVERS**

It was intended in this project to build a complete 10X10 OE switching matrix. During the integration of the various functional modules that compose the whole matrix, a severe and fatal packaging complication was encountered. A high failure rate (10 -20 %) of the photoconductive crosspoints was encountered after the fibres were pigtailed to them with epoxy. The failures were caused by a severe loss of static and dynamic resistance. Apparently the pigtailling operation affected the depletion of the channel. The lost of depletion in a crosspoint channel resulted in a very low impedance device which lead to two serious problems.

The first problem was the change in the source impedance which affected the first equalization stage as well as reducing the response level of the receiver due to larger leakage through the off-state crosspoints. The second problem that arose was the reduced electric field across the defective photoconductors in the on-state, caused by the larger dark current flowing through the DC load



resistance for a fixed bias voltage. This lower electric field across the device led to a lower response at the crosspoint.

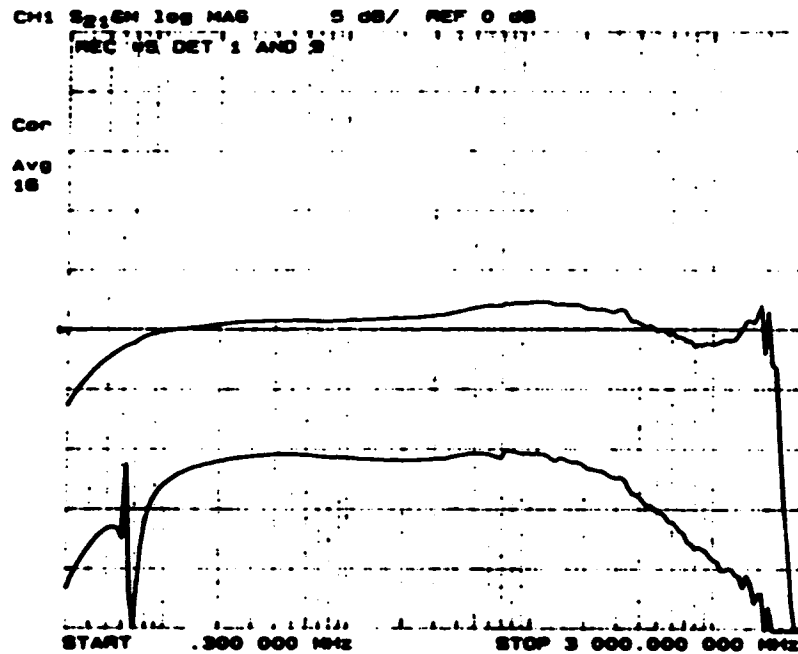


**Figure 6.12 Receiver response with a non depleted photoconductor. The defective crosspoint is in the on-state for the bottom curve and in the off-state for the top curve.**

These effects can be seen in figure 6.12 where the top curve represents a receiver response using a good crosspoint when the array contains a non-depleted crosspoint in the off-state, while the bottom curve corresponds to the same array response using the defective photoconductor in the on-state. The top curve can be compared to the curves presented in figure 6.3 and the change in the response level and the equalization accuracy can be observed. The severe decrease in the response level caused by the reduced electric field across the non-depleted photoconductor can be noted from the difference between the two curves in figure 6.12. It is also noteworthy that the shape of the frequency

response for the defective crosspoint has also been modified by the loss of the depleted channel. This might result from crystal defects caused by the presence of the fibre waveguides on the surface of the photoconductors. The curves presented in figure 6.12 demonstrate that the receiver becomes unoperational if the surface effects of one crosspoint in the array are altered.

This extreme sensitivity of the crosspoints to the presence of the fibres on their surface has prevented the completion of more than one array. At least one crosspoint per array has been structurally damaged during the integration of the various functional modules. The damage did not take place instantly but was time dependent and it always occurred after the biasing of the photoconductive crosspoint. This major problem could hopefully be corrected in the future by the deposition of a passivating layer such as  $\text{SiO}_2$  [51] or  $\text{SiN}$  on the detector surface. ATRC and CRC intend to investigate this approach in the future. However, this would introduce additional steps in the photodetector fabrication process.

Another problem that prevented the completion of the OE switching matrix was the brittleness of the fibres. Many fibres broke slightly above the Si V-grooves during the integration of the switch modules. It would be important in the future to protect the bared fibres such that the manipulation of the V-grooves during the optical coupling to the crosspoints does not lead to the fracturing of some of the waveguides.

## CHAPTER 7

### CONCLUSION

The goal of this project was to develop and build an optoelectronic switching matrix of dimension 10X10, designed for a bandwidth per channel greater than 1 GHz, isolation greater than 60 dB, throughput loss of 0 dB and a signal to noise ratio larger than 30 dB. The realization of this project required the construction of four functional modules, namely the transmitter module, the optical power distribution module, the switching module and the amplifier & equalizer module.

The transmitter module consisted of ten inexpensive compact disk type lasers mounted in two arrays of five optical sources. It was found that these 780 nm inexpensive lasers, if pigtailed to an optical fibre, met all the optical power and bandwidth requirements of this project. Shielded housing of the sources was necessary to allow for low levels of crosstalk between adjacent lasers. The enclosing of the lasers has imposed the use of a fan to prevent the overheating of the optical sources so that the laser biasing circuit could maintain a constant optical output. The two boards constituting the whole transmitter module fit in a standard 6U card frame.

The optical power distribution module consisted of ten 1X10 biconical-taper star couplers whose inputs were spliced to the pigtailed lasers' fibres. The use of the star couplers allowed for the utilization of standard commercial devices. However, the coupling of one hundred fibres to the photoconductor crosspoints was found to be an impractical task. The full potential of an optoelectronic switch matrix could only be attained in the future by the use of integrated optical waveguides to distribute the optical signals to the matrix crosspoints. It is

believed that a hybrid combination of integrated optical and electronic elements is the most promising avenue for the fabrication of large optoelectronic switching matrices.

In the light of this work, two optical distribution networks should be investigated in future, namely the use of ionic-exchange optical waveguides and the use of chemically grown optical waveguides. Such investigations are planned jointly by the Alberta Telecommunications Research Centre (ATRC) and the Alberta Microelectronic Centre (AMC). A first prototype of a chemically grown optical waveguide has already been obtained by using a Chemical Vapor Deposition (CVD) of  $\text{SiO}_2$  on a Si substrate. This prototype is presently being characterized.

The switching module was formed of an array of ten surface depleted photoconductors connected to a common load resistance. The surface depleted photoconductors were found to have a large dark resistance and an isolation level in excess of 60 dB. However, the photoconductors also had an excessive low frequency gain that was dependent on the optical power levels. The large gain mechanism is believed to be caused by trapping centers in the channel. This power dependent gain mechanism made the equalization of the photoconductive crosspoints harder to achieve. A better control over the energy state distribution in the material during the fabrication processes is required to achieve large size broadband optoelectronic matrices using photoconductive crosspoints. Studies have been undertaken at the Department of Communications (DOC) in collaboration with the ATRC to improve the fabrication steps of surface depleted photoconductors.

The amplifier & equalizer module was added to the switching module to form the receiver module. Due to the presence of the amplifier & equalizer module, an effective responsivity of 0.1 A/W from 4 MHz to 1.8 GHz was obtained

for the photoconductive crosspoints. However, it was discovered that the responsivity varies from one crosspoint to another in a single array which may lead to the implementation of a compensation mechanism in future receivers. The receiver module is composed of ten receiver boxes mounted in pairs on circuit boards that fit in a standard 6U card frame.

Severe and fatal packaging problems were encountered during the integration of the four matrix functional modules. It was discovered there was a high failure rate of the photoconductive crosspoints after the fibres were pigtailed to them with epoxy. Apparently, the pigtailling operation affected the depletion of the photoconductor's channel which led to the deterioration of the whole receiver performance. Therefore, due to their lack of reliability, the present surface depleted photoconductors can not be used as crosspoints in an optoelectronic switching matrix with epoxied fibres. Different options are presently investigated to correct the defective surface depleted crosspoints. The passivation of the photoconductor's surface by the deposition of a passivating layer such as  $\text{SiO}_2$  or  $\text{SiN}$  will be examined and the investigation will be jointly carried out by ATRC and DOC.

In the meantime, this project will be completed at the ATRC by replacing the surface depleted photoconductors by Metal-Semiconductor-Metal (MSM) photodetectors. Early measurements at the ATRC have shown that MSM photodetectors fabricated on the same wafer as the photoconductors can be used without equalization to frequencies up to approximately 1.2 GHz with a responsivity in the order of 0.07 A/W. Since the performance of these devices does not depend on surface effects, their performance should not be deteriorated during the pigtailling of the fibres to the crosspoints. On the other hand, the isolation of these devices was found to be between 45 dB and 50 dB. Therefore

the crosstalk between the detectors of a single array could decrease the noise performance of the matrix.

In this project, it was shown that signal processing applications involving arithmetic operation such as summation and subtraction are practical if due care is paid to the different delays of the signals. The feasibility of broadband optoelectronic switching as well as the relatively fast reconfiguration time of the crosspoints was also demonstrated in this project. For these reasons, further effort is justified in the development of optoelectronic switching matrices.

In conclusion, the functional modules for the construction of a 10X10 optoelectronic switching matrix designed for a bandwidth greater than 1 GHz, an isolation level in excess of 60 dB, a 0 dB throughput loss and a SNR larger than 30 dB were built and successfully demonstrated. The integration of the different modules into a complete working unit was delayed because of severe packaging difficulties.

## REFERENCES

- [1] Gigabit Logic, "1989 GaAs IC Data Book & Designer's Guide," 1989.
- [2] R.I. MacDonald, D.K.W. Lam, "Broadband matrix switches: electro-optic or optoelectronic?," *Optical and Quantum Electronics* 18, 1986, pp273-277.
- [3] R.I. MacDonald, E.H. Hara, "Optoelectronic Broadband Switching Array," *Electron. Lett.* 16, pp.502-503, 1978.
- [4] E.H. Hara, R.I. MacDonald, "Optoelectronic Cross-point Switch," U.S. patent 4,286,171, Aug. 1981.
- [5] R.I. MacDonald, D.K. Lam, "Optoelectronic Switch Matrices: Recent developments," *Optical Engineering*, Vol 24, No 2, p.220, 1985.
- [6] S.R. Forrest, G.L. Tangonan, V. Jones, "A Simple 8X8 Optoelectronic Crossbar Switch," *Journal of Lightwave Technology*, Vol. 7, No. 4, April 1989.
- [7] R.I. MacDonald, D.K.W. Lam, R.H. Hum, J. Noad, "Monolithic array of optoelectronic broadband switches," *IEEE J.Solid-State Circuits*, April 1984.
- [8] R.I. MacDonald, D.K.W. Lam, B.A. Syrett, "Hybrid optoelectronic integrated circuit," *Applied Optics*, Vol. 26, No.5, March 1987.
- [9] D.K.W. Lam, R.I. MacDonald, "Crosstalk measurements of monolithic GaAs photoconductive detector arrays in the GHz region," *App. Phys. Lett.* 46 (12), 15 June 1985.
- [10] R.I. MacDonald, D.K. Lam, "Optoelectronic Broadband Switching for Communications and Signal Processing," *AGARD 37<sup>th</sup> Specialists Meeting of the Electromagnetic Wave Propagation Panel*, Istanbul, September 1985.
- [11] E.H. Hara, R.I. MacDonald, "An Optoelectronic Crosspoints Switch for Centrally Switched Distribution of Television Signals," *Canadian Cable Television Association Symposium*, Toronto, 1979.
- [12] R.I. MacDonald, "Optoelectronic Switching in Digital Networks," *IEEE Journal of Selected Areas in Communications*, Vol SAC-3, No. 2, March 1985.
- [13] R.I. MacDonald, "Switched Optical Delay-Line Signal Processors," *Journal of Lightwave Technology*, Vol. LT-5, No. 6, June 1987.
- [14] D.K.W. Lam, B.A. Syrett, "GigaHertz Signal Processing Using Reflex Optoelectronic Switching Matrices," *Journal of Lightwave Technology*, Vol. LT-5, No.3, March 1987.

- [15] D.K.W. Lam, R.I MacDonald, "A Reflex Optoelectronic Switching Matrix," *Journal of Lightwave Technology*, Vol. Lt-2, No.2, April 1984.
- [16] R.I. MacDonald, D.K.W. Lam, R.W. Jenkins, "Reflex Optoelectronic Switching Matrix," U.S. patent 4,898,059, Sept. 1987.
- [17] K.P. Jackson, S.A. Newton, B. Moshhi, M. Tur, C. Cutler, J. Goodman, H. Shaw, "Optical fibre Delay-Line Signal Processing," *IEEE Trans. Microwave Theory and Techniques*, MTT-33, pp.193-210, 1985.
- [18] R.I. MacDonald, E.H. Hara, A.L. Poirier, "Optoelectronically Switched Phase Shifter for Radar and Satellite Phased Array Antennas," U.S. patent 4,886,533, Aug. 1987.
- [19] J.E. Bowers, S.A. Newton, W.S. Sorin, and H.J. Shaw, "Filter response of single mode fiber recirculating delay lines," *Electron. Lett.*, Vol. 18, pp.110-111, 1982.
- [20] A. Huang, Y. Tsunoda, J.W. Goodman, and S. Ishihara, "Optical Computation using residual arithmetic," *Appl. Opt.* 18, 149 (1979).
- [21] R.I. MacDonald, "Optoelectronic switch matrix as a look-up table for residue arithmetic," *Optics Letters*, Vol. 12, No. 10, Oct. 1987.
- [22] R.I. MacDonald, "Architecture of Optoelectronic Neural Networks," *submitted paper*.
- [23] D.K.W. Lam, R.I. MacDonald, "Fast Optoelectronic Crosspoint Electrical Switching of GaAs Photoconductors," *IEEE Electron Device Letters*, Vol. EDL-5, No. 1, 1984.
- [24] R.I. MacDonald, K.O. Hill, "Optoelectronic Compound Switching Matrix," U.S. patent 4,783,850, Nov. 1988.
- [25] J. Senior, "Optical Fiber Communications Principles and Practice," Prentice-Hall International Series in Optoelectronic, 1985.
- [26] J.P. Nérrou, "Les fibres optiques: Introduction aux télécommunications par fibre optique," édition Le Griffon d'argile, 1983.
- [27] *Sharp Laser Diode User's Manual*, 1986.
- [28] N. Bar-Chaim, S. Margalit, A. Yariv, I. Ury, "GaAs Integrated Optoelectronics," *IEEE Trans. on Electron devices*, Vol. ED-29, No. 9, Sept. 1982.
- [29] *Mitsubishi Optical Semiconductors manual*, 1986.
- [30] Y. Suematsu and T. Hong, "Suppression of relaxation oscillations in light output of injection lasers by electrical resonance circuit," *IEEE J. Quantum Electron.*, QE-13(6), pp.758-762, 1977.



- [31] K.Y. Lau, C. Harder, A. Yariv, "Longitudinal Mode Spectrum of Semiconductor Lasers Under High-Speed Modulation," *IEEE Journal of Quantum Electronics*, Vol. QE-20, No. 1, Jan. 1984.
- [32] D. Botsz and G.J. Harkskowitz, "Components for optical communications systems: a review", *Proc. IEEE*, 68(6), pp.699-730, 1980.
- [33] B. Swaida, *ATRC Summer Work Report*, Summer 1988.
- [34] J.M.N. Seto, "Optoelectronic Crosspoint Switching," *Summer work report*, University of Waterloo, Dept. of Elect. Eng., 13 September 1982.
- [35] R.I MacDonald, E.H. Hara, "Optoelectronic Switching Matrices break GHz barrier," *Microwave System News*, Nov. 1981, pp. 97-104.
- [36] R.I. MacDonald, E.H. Hara, "Switching with Photodiodes," *IEEE Journal of Quantum Electronics*, Vol. QE-16, No. 3, March 1980.
- [37] E.H. Hara, R.I. MacDonald, Y. Tremblay, "Optoelectronic Switching with Avalanche Photodiodes," *IEEE Topical Meeting on Optical Communication*, Washington, 1979.
- [38] E.H. Hara, "Optoelectronic Switching," *SPIE Vol. 517 Integrated Optical Circuit Engineering*, p.239, 1984.
- [39] E.H. Hara, S. Machida, M. Ikeda, H. Kanbe, T. Kimura, "A high speed Optoelectronic Matrix Switch using Heterojunction Switching Photodiodes," *IEEE Journal of Quantum Electronics*, Vol. QE-17, No. 8, pp. 1539-1546, Aug. 1981.
- [40] A. Rose, "Concepts in Photoconductivity and Allied Problems," Interscience Publishers, 1963.
- [41] M. Ito, O Wada, "Low Dark Current GaAs Metal-Semiconductor-Metal (MSM) Photodiodes Using WS<sub>2</sub> Contacts," *IEEE J. Quant. Elect.*, Vol. QE-22, No. 7, July 1986.
- [42] S.M. Sze, "Physics of Semiconductor Devices," 2nd ed., Wiley, 1981.
- [43] C. Kelly, "Planer Interdigitated Photodetectors," CTR 148-90, 1990.
- [44] S.M. Sze, D.J. Coleman Jr., A. Loya, "Current transport in metal-semiconductor-metal (MSM) structures," *Solid-State Electron.*, Vol. 14, pp.1209-1218, 1971.
- [45] M. DiDomenico Jr., O. Svelto, "Solid-State Photodetection: A Comparison between Photodiodes and Photoconductors," *Proc. IEEE*, 52, 136 (1964).
- [46] R.I. MacDonald, E.H. Hara, R.H. Hum, "Fast Photoconductive Optoelectronic Broadband Switch with Low Control Voltage," *Electron. Lett.* 17, pp611-612, 1981.

- [47] D.K. Lam, R.I. MacDonald, J. Noad, B. Syrett, "Surface-Depleted Photoconductors," *IEEE Trans. Elec. Dev.*, Vol. ED-34, No. 5, Part 1, May 1987.
- [48] R.I. MacDonald, D.K.W. Lam, J.P. Noad, "Depleted Channel Photoconductor," U.S. patent 4,727,349, Feb. 1988.
- [49] J.S. Blekernore, "Semiconducting and other major properties of Gallium arsenide," *J. Appl. Phys.* 53 (10), October 1982
- [50] R.J. Seymor, B.K. Garside, "Intrinsic and extrinsic factors limiting the time response of interdigitated photodetectors," 4<sup>th</sup> Canadian Semiconductor Technology Conference, Ottawa, Ontario, Aug. 1988.
- [51] H. Beneking, "On the Response Behavior of Fast Photoconductive Optical Planar and Coastal Semiconductor Detectors," *IEEE Transactions on Electron Devices*, Vol. ED-29, No. 9, September 1982.
- [52] A. Rose, "An outline of some photoconductive processes," *RCA Rev.*, Vol 12, pp.382-414, 1951.
- [53] R.A. Smith, "Semiconductors," Cambridge University Press, 1978.
- [54] L.K. Anderson, M. DiDomenico Jr., and M.B. Fisher, "High-Speed Photodetectors for Microwave Demodulation of Light," in L. Young, Ed., *Advances in Microwaves*, Vol. 5, Academic, New York, pp. 1-122, 1970.
- [55] S.R. Forrest, "The sensitivity of Photoconductor Receivers for Long-Wavelength Optical Communications," *JLT*, Vol. LT-3, No. 2., April 1985.
- [56] A. van der Ziel, "Fluctuation Phenomena in Semiconductors," Academic Press Inc., New York, 1969.
- [57] Y. Yamada, M. Yamada, H. Terui, M. Kobayashi, "Optical interconnections using a silica-based waveguide on a silicon substrate," *Optical Engineering*, December 1989, Vol. 28, No. 12.
- [58] G. Mak, D. Bruce, P. Jessop, "Waveguide-Detector Couplers for Integrated Optics and Monolithic Optoelectronic Switching Arrays," 4<sup>th</sup> Canadian Semiconductor Technology Conference, Ottawa, Ontario, 1988.
- [59] J. Soble, H. Schumacher, R. Esagui, M. Koza, R. Bhat, "Waveguide integrated MSM Photodetector on InP," *Electronics Letters*, Vol. 24, No. 24, November 1988.
- [60] R.I. MacDonald, D.K.W. Lam, B.A. Syrett, "Hybrid optoelectronic integrated circuit," *Applied Optics*, Vol. 26, No. 5, March 1987.
- [61] D.K.W. Lam, R.I. MacDonald, "Optoelectronic Assembly and Method of Making the Same," U.S. patent 4,699,449, Oct. 1987.
- [62] L.L. Blyler, G.J. Grimes, "Resin-filled mixing rod optical coupler," OFC'89, Houston 1989.

- [63] K.O. Hill, Y. Tremblay, B.S. Kawasaki, "Modal noise in multimode fiber links: theory and experiment," *Optics Letters*, Vol. 5, No. 6, June 1980.
- [64] B.S. Kawasaki, K.O. Hill, Y. Tremblay, "Modal-noise generation in biconical-taper couplers," *Optics Letters*, Vol. 6, No. 10, October 1981.
- [65] K. Peterman, G. Arnold, "Noise and Distortion Characteristics of Semiconductor Lasers in Optical Fiber Communication Systems," *IEEE Journal of Quantum Electronics*, Vol. Qe-18, No. 4, April 1982.
- [66] G. Gonzalez, "Microwave Transistor Amplifiers: Analysis and Design," Prentice Hall, 1984.
- [67] J. Millman, "Micro-Electronics: Digital and Analog Circuits and Systems," McGraw-Hill, 1979.

## APPENDIX A

### COMPONENT SELECTION FOR LASER BIAS CIRCUIT

This appendix contains guidelines for the component selection of the laser biasing circuit presented in chapter 2.

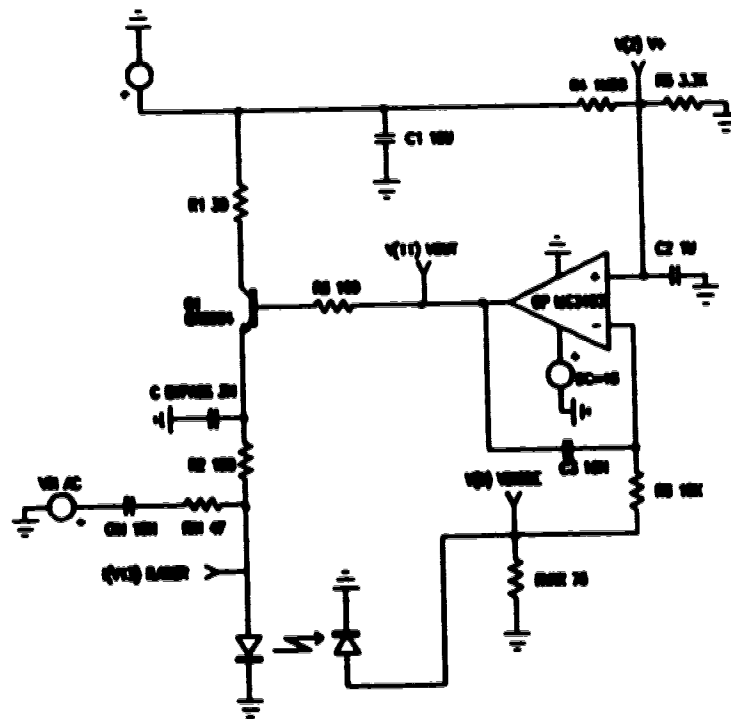


Figure A.1 Transmitter biasing circuit.

$R_1$  and  $R_2$  have to be chosen such that the maximum safe bias current would begin to saturate the transistor. This value is typically set at 72 mA for a ML60X1 laser.  $R_2$  should be significantly larger than  $R_1$  and placed as near to the RF input as possible in order to isolate the bias circuit.  $R_2$  also has to be large enough to protect the laser in case of a malfunction of the transistor. On the other

hand,  $R_2$  has an upper limit that is determined by the resistance value that will prevent the saturation of the operational amplifier before the saturation of the transistor.

$R_6$  and  $C_3$  determine the highest frequency perturbation that the feedback loop can attenuate.

$R_4$  and  $R_5$  determine the reference voltage which is compared to the voltage generated by the photodiode. The ratio  $R_4/R_5$  is chosen such that the forward voltage across the photodiode is kept to a low value. The  $R_5C_2$  network specifies the speed at which the reference voltage reaches equilibrium on start-up as well as it constitutes a low frequency noise filter. This ac network is designed to short to ground the power line's noise components above 50 Hz. The capacitor  $C_1$  constitutes, with the power supply's low output impedance, a high frequency noise filter.

$R_{1a}$  and  $C_{1a}$  match the driver input impedance to the characteristic impedance of the RF input line. The laser diode has, typically, a dynamic resistance of 3 ohms in series with a 3 nH inductance when above threshold. The time constant of this network determines the minimum frequency of the electrical signal that is passed to the laser. This frequency should be a lot higher than the maximum frequency that the feedback loop can track.

## APPENDIX B

### SI V-GROOVE FABRICATION STEPS (Courtesy of Y. Loke, AMC)

This appendix contains the steps required to the fabrication of Si V-grooves used in the fibre alignment, as described in chapter 4.

The starting material is a  $\langle 100 \rangle$  silicon wafer. A layer of thin oxide is grown thermally to act as a masking layer during the anisotropic etching of silicon. The wafer is first vapour primed with hexamethyldisilazane (HMDS) which acts as an adhesion promoter between the silicon dioxide and the photoresist, refer Fig. (a).

The wafer is then coated with positive photoresist, refer Fig. (b). Positive photoresist becomes vulnerable to the the developer after it has been exposed to ultraviolet light. Softbaking occurs right after. It is a process step wherein almost all of the solvents are removed from the resist coating, thereby rendering the coating photosensitive.

Since positive photoresist is applied, the mask must be of such that areas to be etched away are exposed to the ultraviolet light, refer Fig. (c). After exposing, the wafer is then developed (in sodium hydroxide) where previously exposed photoresist will be removed, see Fig. (d). Next process is hardbaking. Hardbaking is a process which increases the resistance of the resist to subsequent etching process.

The wafer is then dipped into 10:1 buffered oxide etchant (BOE) which is a combination of hydrofluoric acid and ammonium fluoride, refer Fig. (e). This process removes the silicon dioxide thus exposing the silicon. The photoresist is then stripped away, see Fig. (f).

The wafer is finally ready for anisotropic etching. The anisotropic etchant used is a combination of ethylenediamine, pyrocathocal and water which is commonly known as EDP. EDP attacks silicon dioxide at a very slow rate making silicon dioxide a very suitable masking layer. Photoresist cannot be used. EDP etches silicon 35X faster in the  $\langle 100 \rangle$  plane compared to the  $\langle 111 \rangle$  plane. The etching is discontinued once the  $\langle 111 \rangle$  planes meet. Further etching will result in wider V-grooves. The final step is to etch the silicon dioxide in 10:1 BOE, refer to Fig. (h).

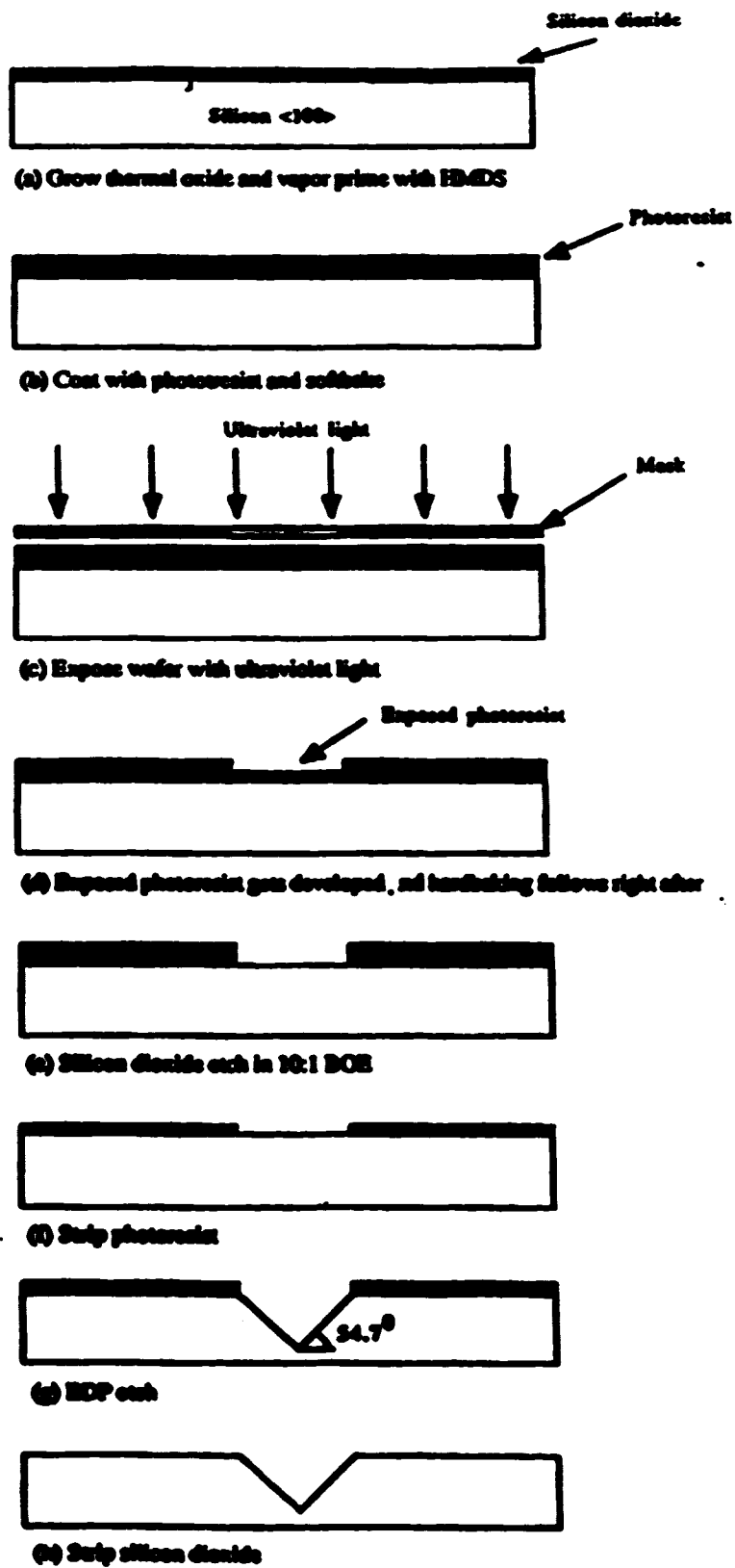


Figure B.1 Fabrication steps of Si V-grooves.

**APPENDIX C**  
**RECEIVER SIMULATION MODEL**

This appendix contains the model used and the CNL listing for the receiver simulations presented in chapters 6 and 7.

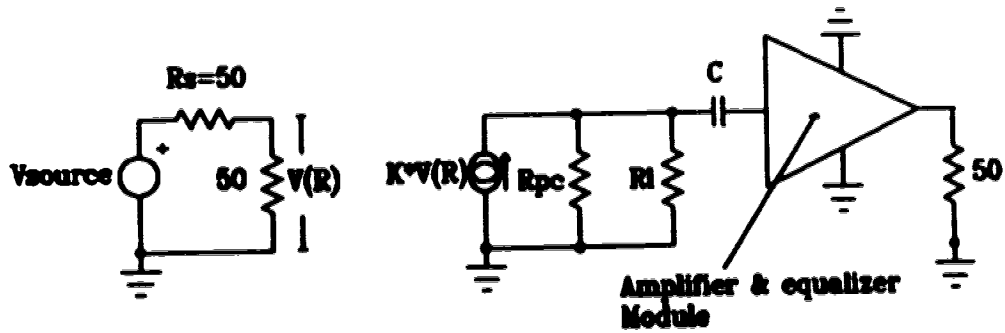


Figure C.1 Model circuit for receiver simulations.



FIRECSO.DAT

Tuesday, July 31, 1990 1:41 pm

```

varl rpc 50 100 1000
MSUB1 4.7 0.062 0.0015 0 0 1e9
FRBQS 1e08 3.0e09 1.0e08
CKT
  RS 1 0 50
  res 1 0 50
  vccs 1 0 2 0 0.02
  res 2 0 rpc
  RES 2 0 510
  CAP 2 3 1e-8
  NSLINE 3 4 SUB1 0.090 0.023
  SPAR 4 0 5 0 d:\marc\cml\MSA335.35M
  NSLINE 5 6 SUB1 0.140 0.023
  RES 6 7 375
  CAP 7 0 1E-8
  CAP 6 8 1.0e-8
  RES 8 9 300
  CAP 8 9 1.5e-12
  CAP 8 0 1e-13
  NSLINE 9 10 SUB1 0.090 0.023
  SPAR 10 0 11 0 d:\marc\cml\msa435.50m
  NSLINE 11 12 SUB1 0.140 0.110
  RES 12 13 210
  CAP 13 0 1e-8
  CAP 12 50 1e-8
  res 50 51 39
  cap 50 51 100e-12
  res 51 14 39
  cap 51 14 6.8e-12
  NSLINE 14 15 SUB1 0.090 0.110
  SPAR 15 60 16 60 d:\marc\cml\ina3170.12m
  ind 60 0 0.2e-9
  NSLINE 16 17 SUB1 0.140 0.023
  RES 17 18 360
  CAP 18 0 1e-8
  CAP 17 19 1e-8
  NSLINE 19 20 SUB1 0.090 0.023
  SPAR 20 0 21 0 d:\marc\cml\MSA435.50M
  NSLINE 21 22 SUB1 0.140 0.11
  RES 22 23 210
  CAP 23 0 1E-8
  CAP 22 24 1E-8
  NSLINE 24 25 SUB1 0.090 0.110
  RL 25 0 50
END

```

**APPENDIX D**  
**DRAWINGS**

**This appendix contains the detailed drawings of the various components forming the receiver boxes and the matrix rack.**

**OPTOELECTRONIC SWITCH RECEIVER ASSEMBLY MECHANICAL DESIGN**

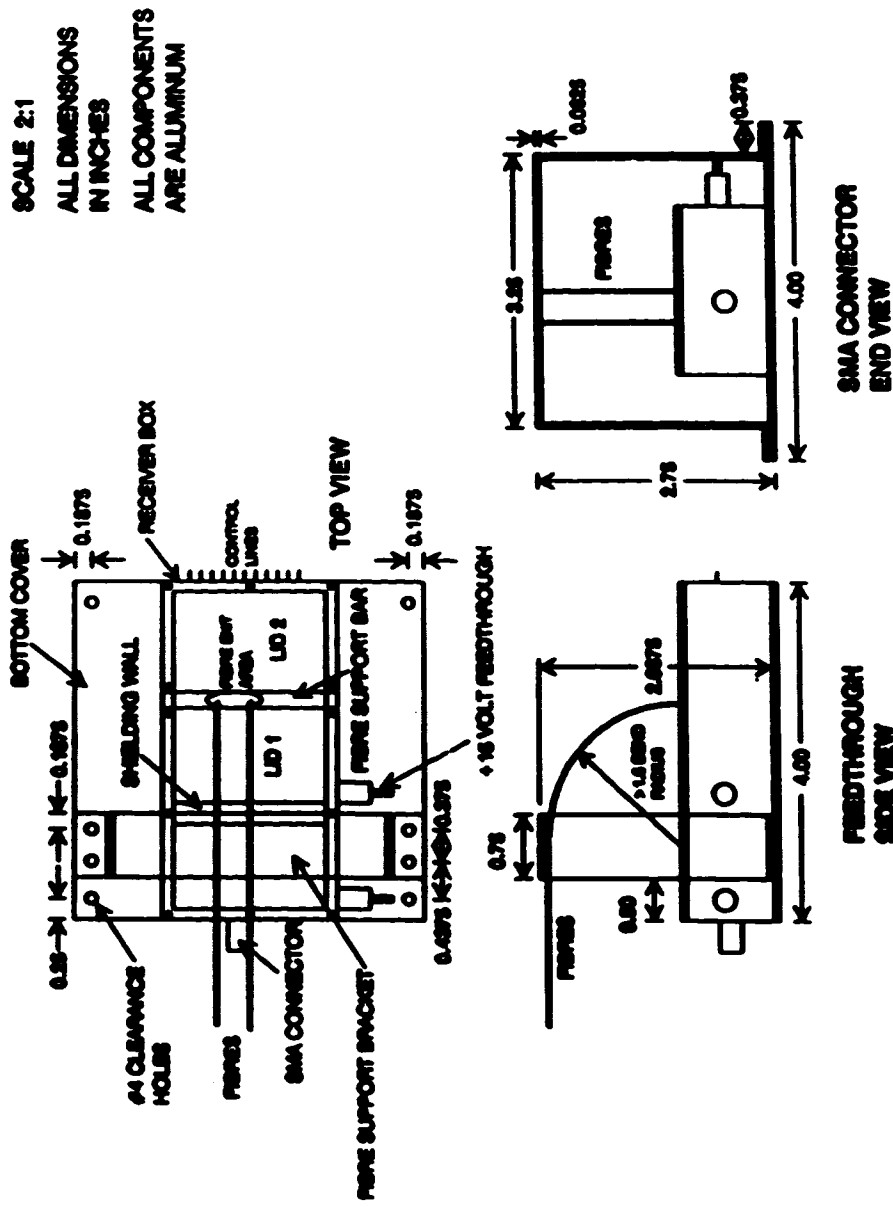


**Figure D.1 OE Switch Receiver Assembly Mechanical Design.**

000000-000000-000000-0



**OPTOELECTRONIC SWITCH RECEIVER BOX MECHANICAL DESIGN**

**SCALE 1:1**  
**ALL DIMENSIONS**  
**IN INCHES**

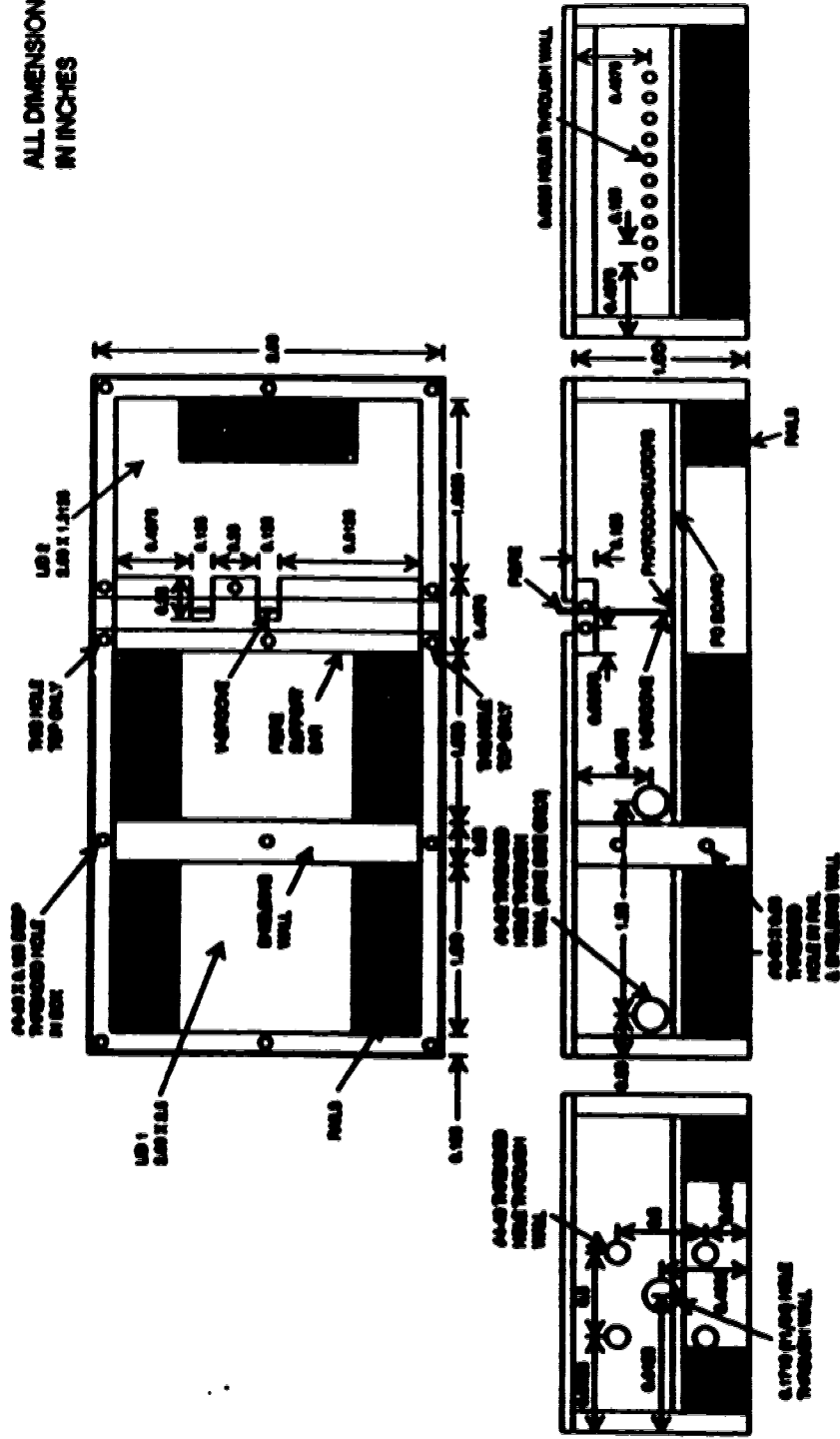


**Figure D.3 OE Switch Receiver Box Mechanical Design.**

000000-000000-1-001Rev. 1

**OPTOELECTRONIC SWITCH RECEIVER BOX MECHANICAL DESIGN**

**SCALE 1:1  
ALL DIMENSIONS  
IN INCHES**

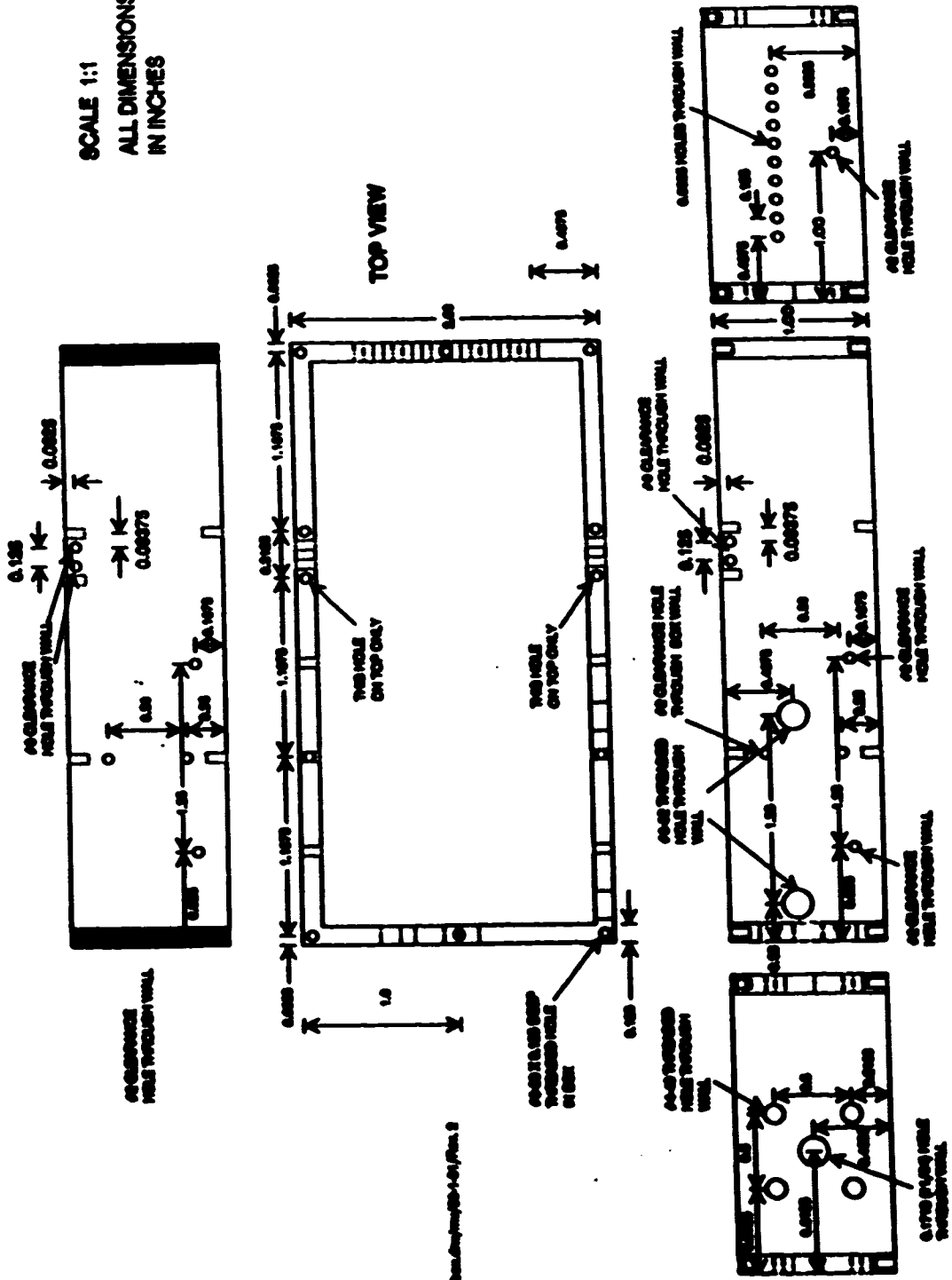


**Figure D.4 OE Switch Receiver Box.**

**OPTOELECTRONIC SWITCH RECEIVER BOX SHIELDING WALL**

**SCALE 1:1  
ALL DIMENSIONS  
IN INCHES**

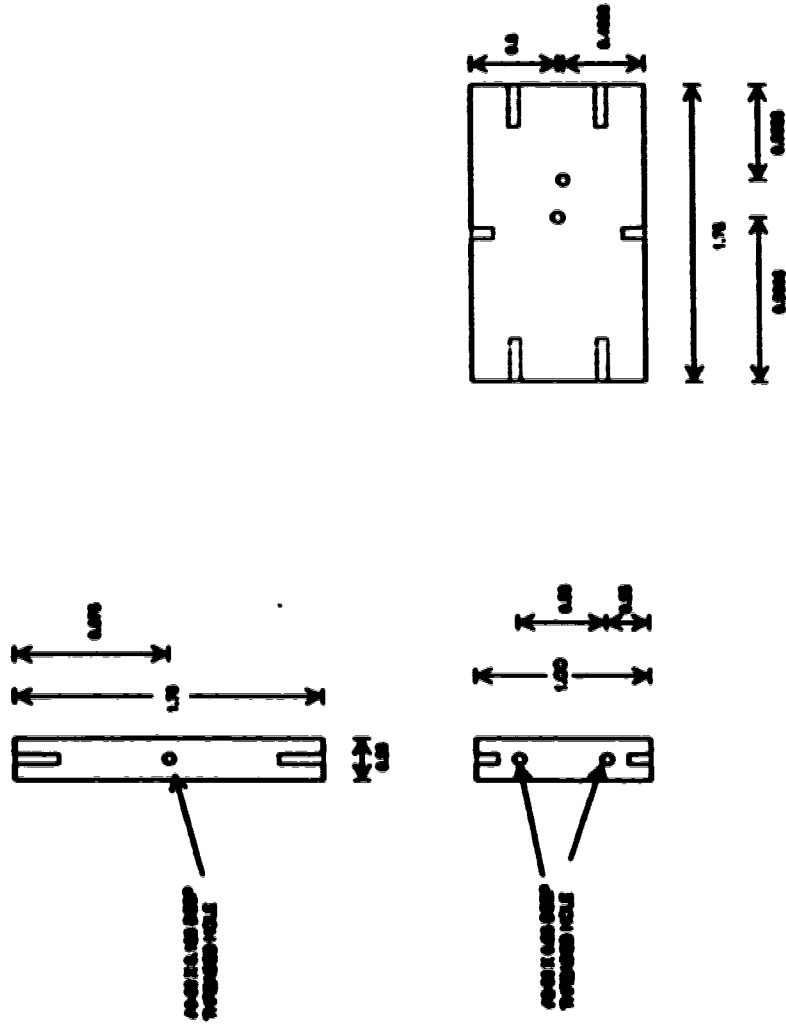


**Figure D.5 OE Switch Receiver Box Shielding Wall.**

continued on page 124

**OPTOELECTRONIC SWITCH RECEIVER BOX TOP LIDS**

**SCALE 1:1  
ALL DIMENSIONS  
IN INCHES**

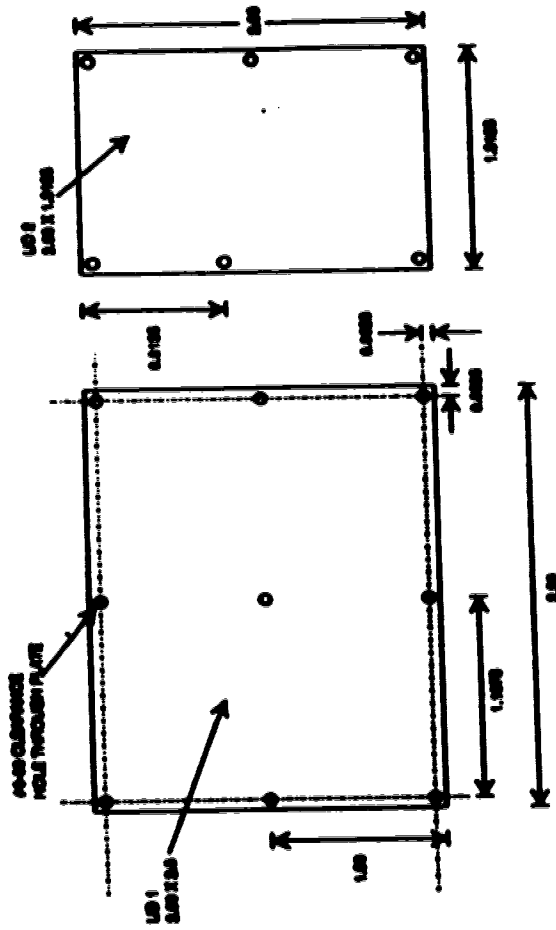
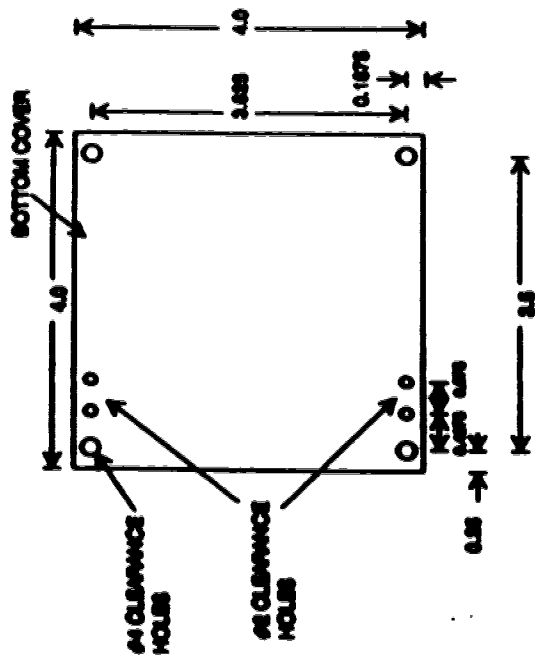


**Figure D.6 OE Switch Receiver Box Top Lids.**



**OPTOELECTRONIC SWITCH RECEIVER BOTTOM LID**



**SCALE 2:1**  
**ALL DIMENSIONS**  
**IN INCHES**  
**ALL COMPONENTS**  
**ARE ALUMINUM**

821-20-0000-00-00-00-00

**Figure D.7 OE Switch Receiver Bottom Lid.**

**OPTOELECTRONIC SWITCH RECEIVER BOX RAILS**

**SCALE 1:1  
ALL DIMENSIONS  
IN INCHES**

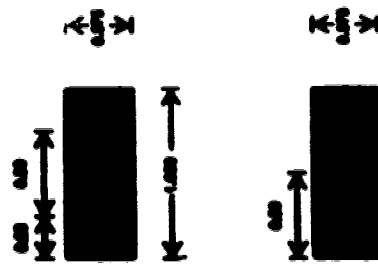
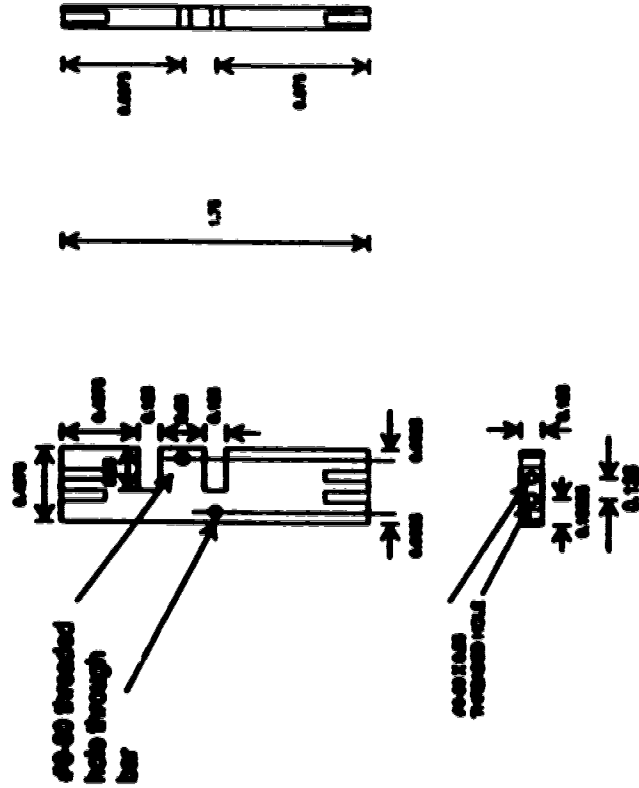


**Figure D.8 OE Switch Receiver Box Rails.**

www.mechassis.com

**OPTOELECTRONIC SWITCH RECEIVER BOX FIBRE SUPPORT BAR**

**SCALE 1:1**  
**ALL DIMENSIONS**  
**IN INCHES**



00-00 threaded hole through hole

**Figure D.9 OE Switch Receiver Box Fibre Support Bar.**

**OPTOELECTRONIC SWITCH RECEIVER FIBRE SUPPORT BRACKET**

**SCALE 2:1  
ALL DIMENSIONS  
IN INCHES  
ALL COMPONENTS  
ARE ALUMINUM**

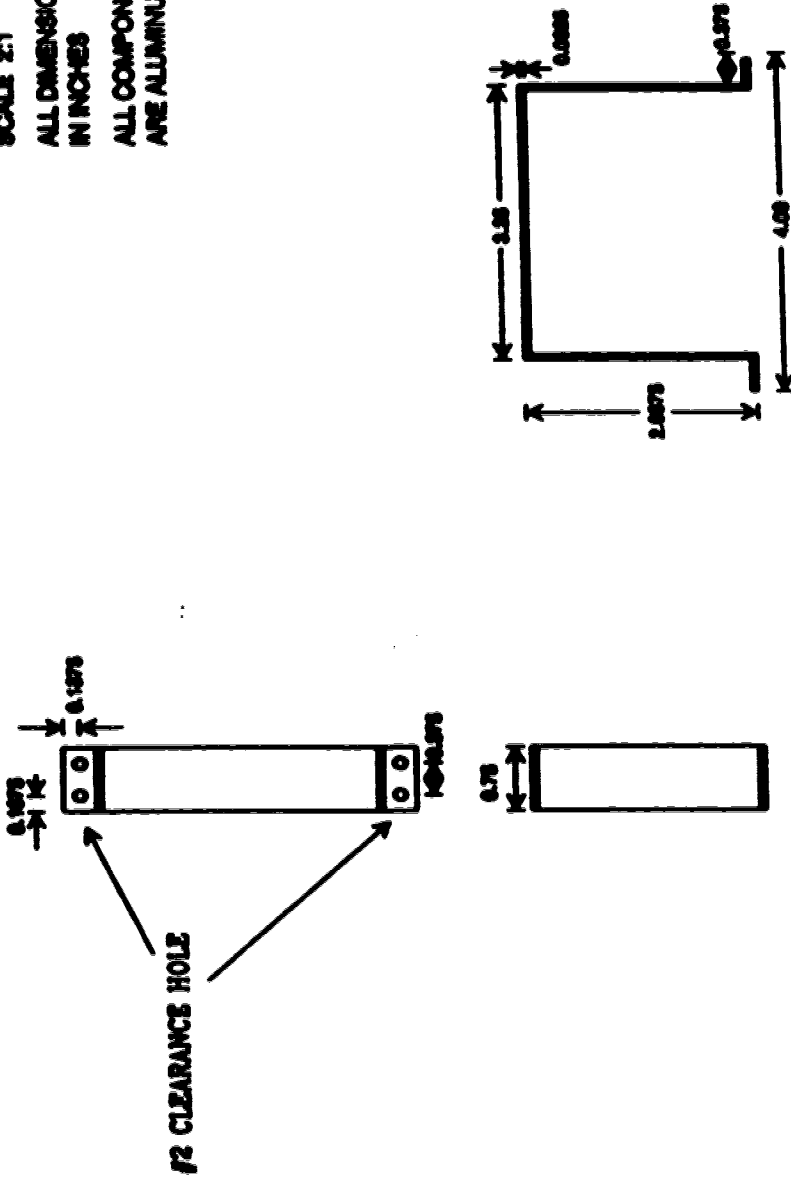


**Figure D.10 OE Switch Receiver Fibre Support Bracket.**





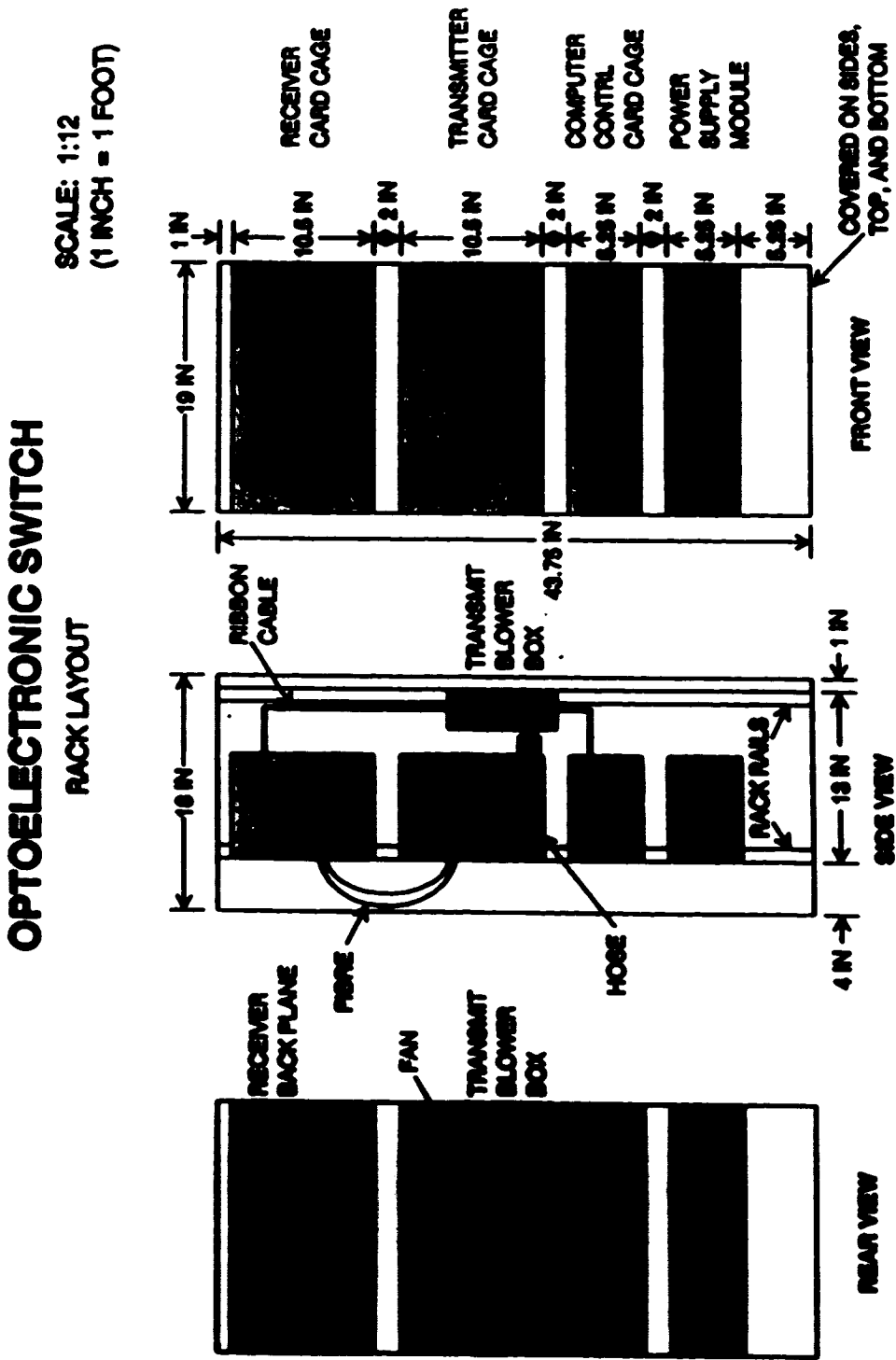


Figure D.19 OE Switch Rack Layout

continued on page 132

# OPTOELECTRONIC SWITCH

## RACK LAYOUT

SCALE: 1:12  
(1 INCH = 1 FOOT)

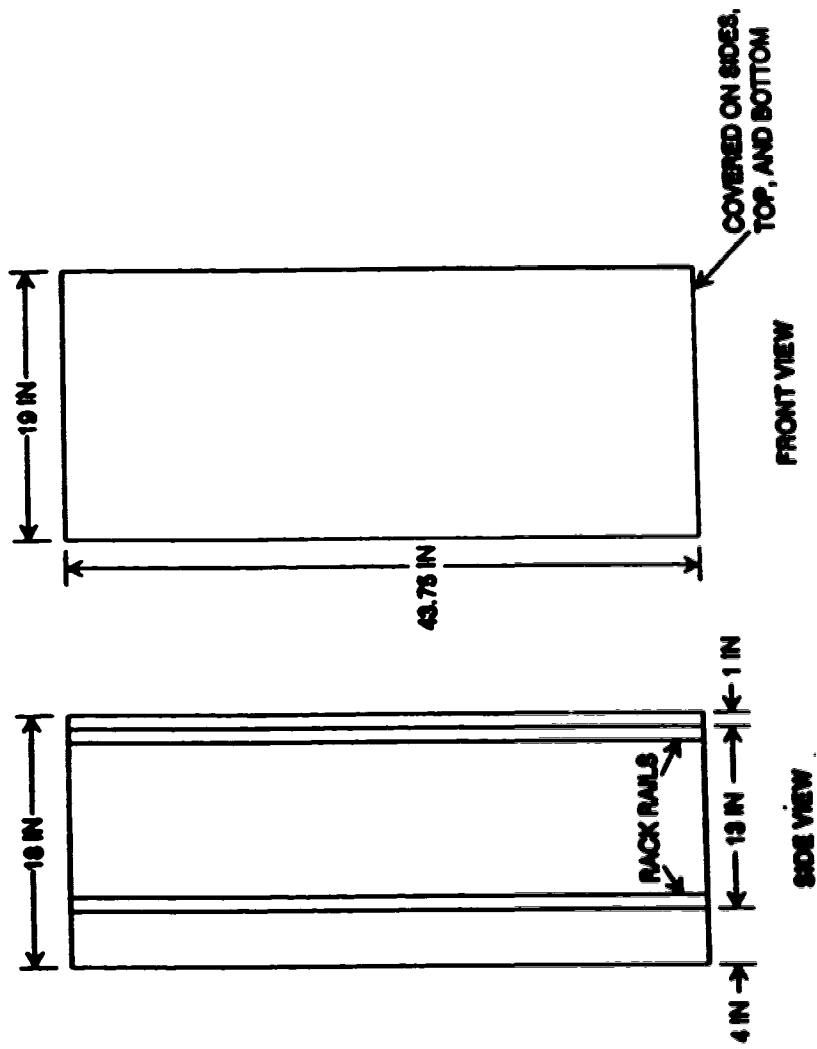


Figure D.14 OE Switch Rack Layout

continued on next page



**APPENDIX E**  
**PRINTED CIRCUIT BOARDS**

This appendix contains the printed circuit boards that were designed for the receiver circuits, the receiver module and the transmitter module.

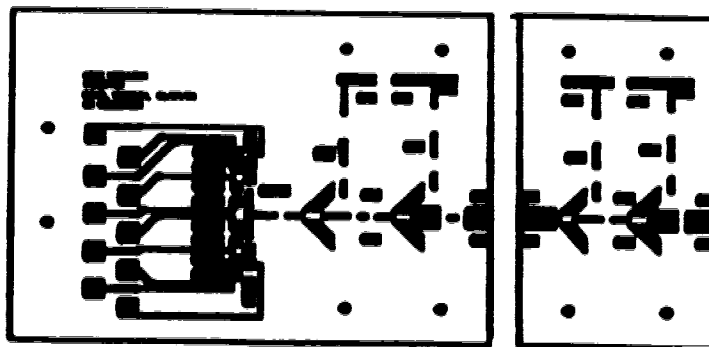


**Figure E.1 Receiver printed circuit board.**

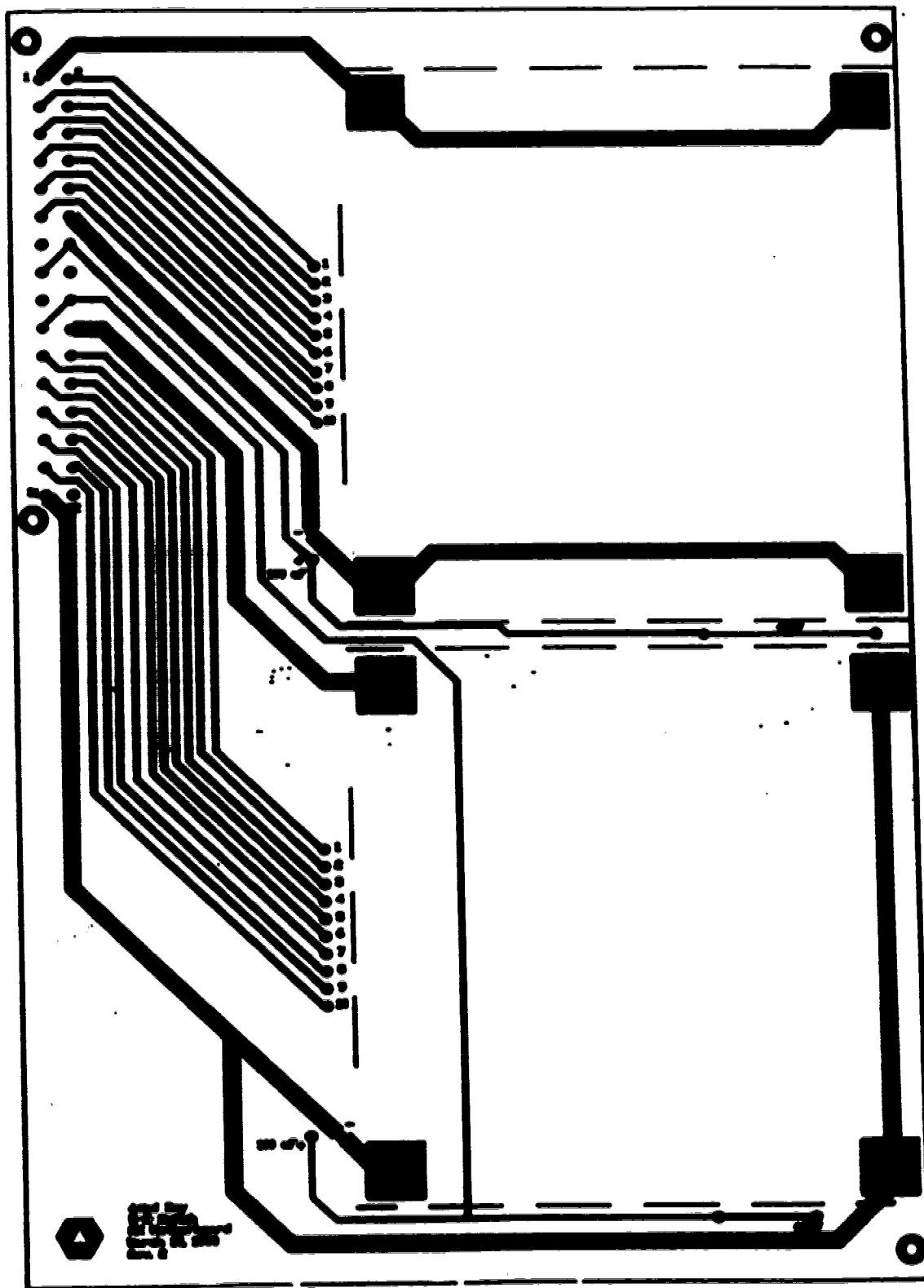


Figure E.2 Receiver module printed circuit board.

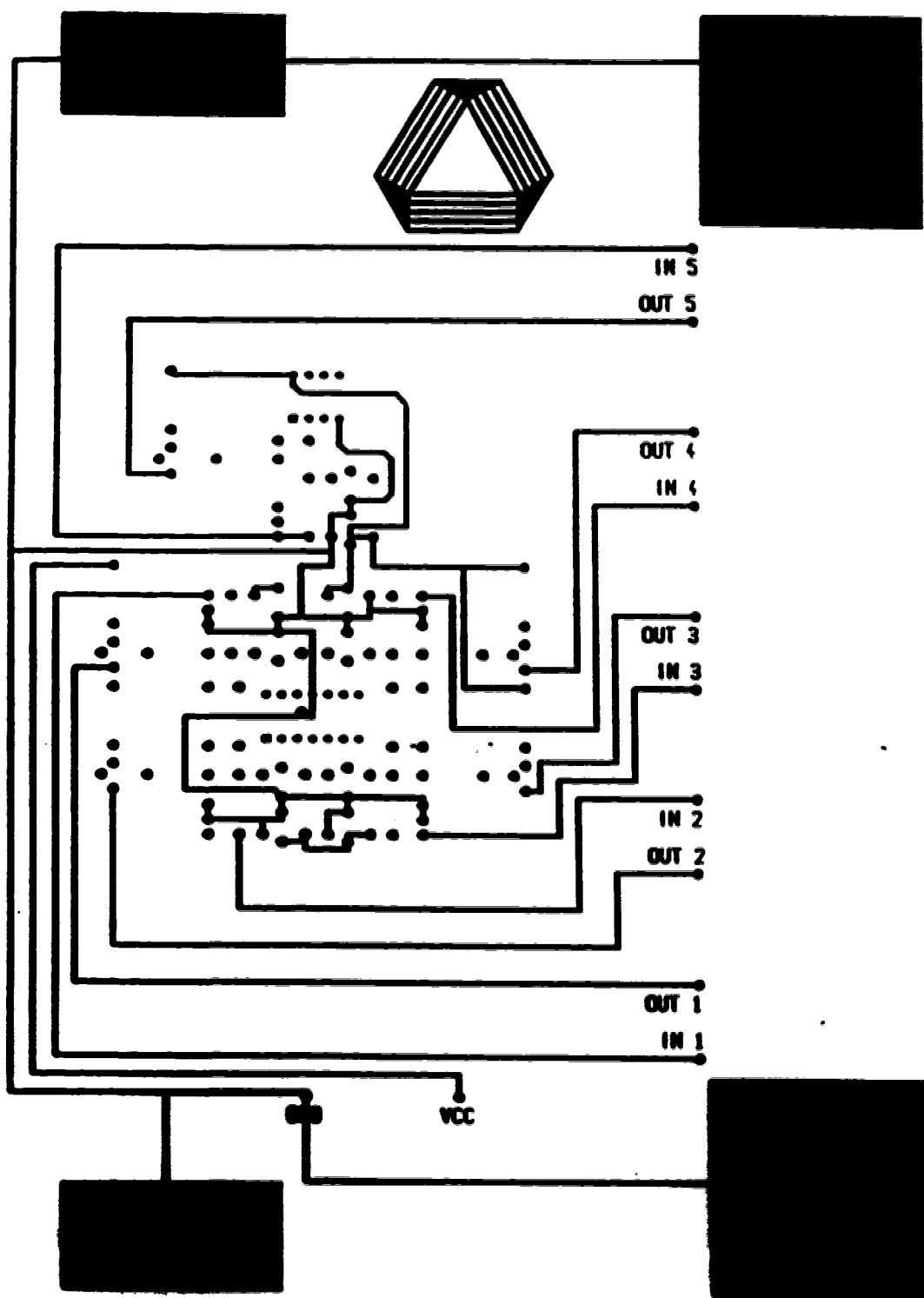


Figure E.3 Transmitter module printed circuit board (front plane).

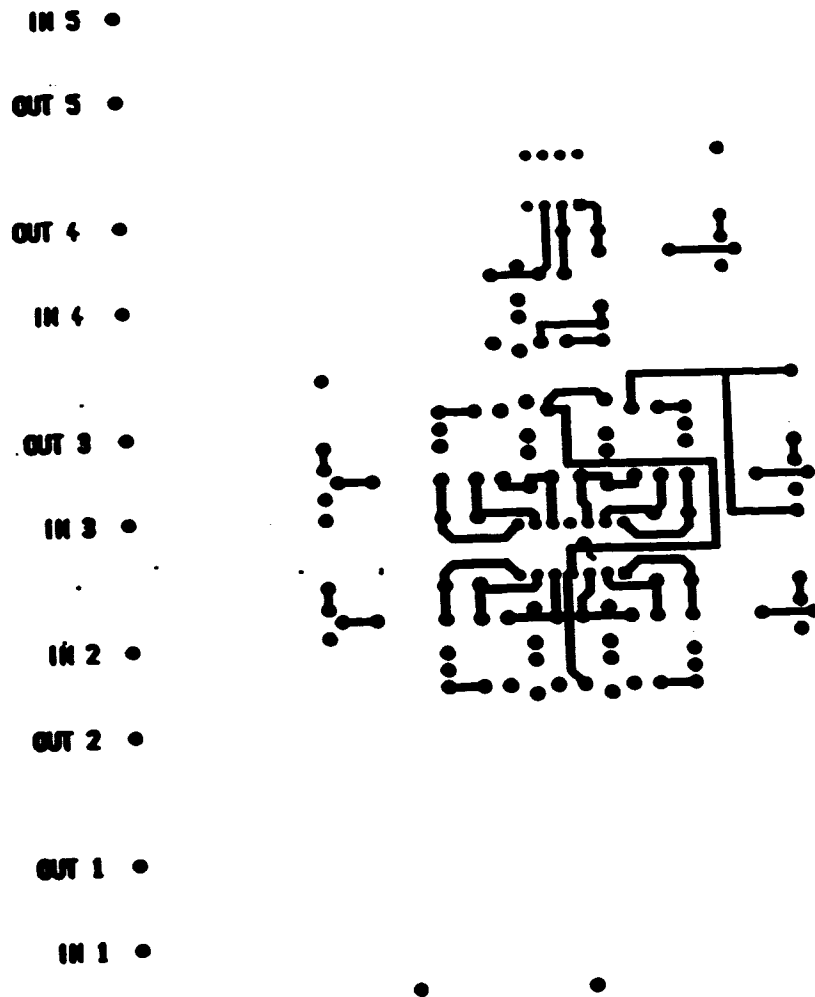


Figure E.4 Transmitter module printed circuit board (back plane).

**APPENDIX F**  
**DEVICE DATA SHEETS**

**This appendix contains the data sheets for the Mitsubishi ML6XX1 laser family, the Canstar 1X10 biconical-taper star couplers, and the Avantek MMIC gain blocks (MSA-0335, MSA-0435, INA-03170).**

**MITSUBISHI LASER DIODES**  
**ML6101A, ML6411A**  
**ML6701A**  
**FOR OPTICAL INFORMATION SYSTEMS**

**DESCRIPTION**

Mitsubishi ML6101A, ML6411A, ML6701A are AlGaAs high power laser diodes emitting light beams around 780 nm wavelength. They lase by applying forward current exceeding threshold values, and emit light power about 10 mW CW at operating current around 25 mA in excess of the threshold current. They operate under CW or pulse condition according to input current, at case temperature up to 60°C. Since they lase in a stable fundamental transverse mode, TE<sub>00</sub> and smooth, linear light vs. current characteristics, they are well suited for optical information processing systems, and other optical system.

**APPLICATION**

- Writing and reading memory discs
- Laser cards
- Laser printers

Under pulsed condition, such as disc memory writing, a peak light output of 25 mW can be obtained.

The ML6101A, ML6411A, ML6701A are hermetically sealed devices having a silicon photodiode for monitoring the light output.

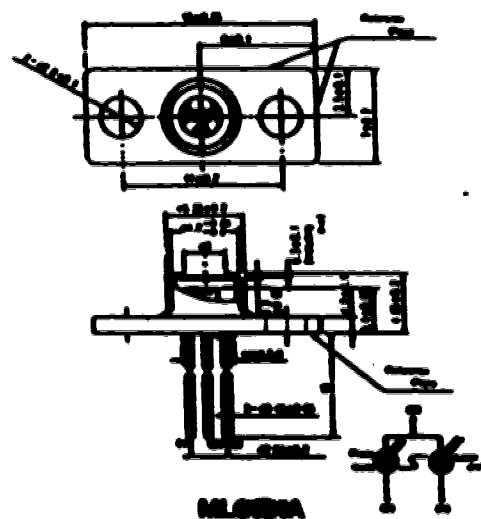
Output current of the photodiode can be used for automatic control of the operating currents or case temperature of the laser.

**FEATURES**

- Low threshold current, typical 40 mA
- CW or pulsed operation up to case temperature of 60°C
- Electrical monitoring (a photodiode is installed in the laser package)

**OUTLINE DRAWINGS**

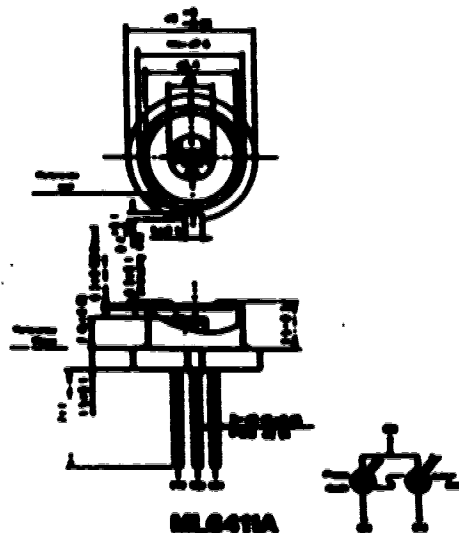
Dimensions in mm



ML6101A

**OUTLINE DRAWINGS**

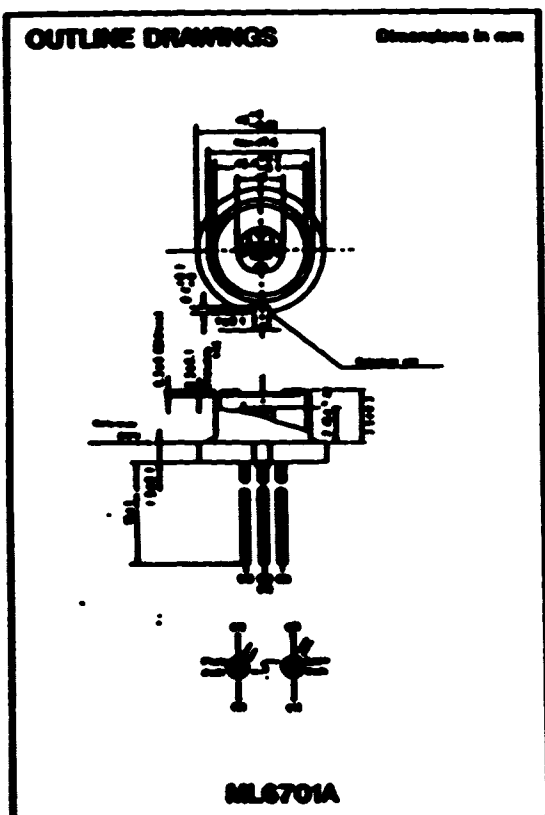
Dimensions in mm



ML6411A

**ML6101A,ML6411A  
ML6701A**

**FOR OPTICAL INFORMATION SYSTEMS**



**ABSOLUTE MAXIMUM RATINGS**

Symbol	Parameter	Conditions	Rating	Unit
$P_o$	Light output (avg)	ON	20	mW
		Pulse (Pulse)	25	
$V_{R1}$	Reverse voltage (Anode-cathode)	-	2	V
$V_{R2}$	Reverse voltage (Photodiode)	-	10	V
$I_F$	Forward current (Photodiode)	-	10	mA
$T_c$	Operating case temperature	-	-40-+60	°C
$T_{stg}$	Storage temperature	-	-55-+100	°C

Note: Duty less than 20%, pulse width less than 1ms.

MITSUBISHI LASER DIODES  
**MLG101A, MLG411A**  
**MLG701A**

FOR OPTICAL INFORMATION SYSTEMS

**ELECTRICAL/OPTICAL CHARACTERISTICS (T<sub>c</sub>=25°C)**

Symbol	Parameter	Test condition	Characteristics			Unit
			Min.	Typ.	Max.	
$I_{th}$	Threshold current	ON	10	40	60	mA
$I_{sp}$	Operating current	ON, $P_o = 10mW$	-	65	100	mA
$V_{sp}$	Operating voltage (Lower diode)	ON, $P_o = 10mW$	-	2.0	2.5	V
$I_{br}$	Dark current (Photodiode)	$V_{br} = 0V$	-	-	0.5	$\mu A$
$P_o$	Light output	ON, $I_f = I_{sp} + 25mA$	-	10	-	mW
$\lambda_p$	Leading wavelength	ON, $P_o = 10mW$	785	790	795	nm
$\theta_{1/2}$	Full angle at half maximum	ON, $P_o = 10mW$	10	12	17	deg
$\theta_{1/4}$			20	20	25	deg
$C_c$	Capacitance (Photodiode)	$V_{br} = 0V, f = 10kHz$	-	7	-	pF
$I_{max}$	Maximum output current	ON, $P_o = 10mW$ $I_f = 100 \text{ (Max)}$	0.3	0.6	1.7	mA

Note:  $I_{th}$  is test resistance of the photodiode.

**1. Light output vs forward current**

Typical light output vs forward current characteristics are shown in Fig. 1. The typical threshold current for lasing is 40mA at room temperature. Above the threshold, the light output increases linearly with current, and no kinks are observed in the curves. As can be seen in Fig. 1, the threshold current and slope efficiency ( $\eta_{sp}$ ,  $\eta_{ext}$ ) depends on case temperature of the laser.

This suggests that an automatic control of temperature or current is necessary to keep the light output constant since temperature variation is inevitable in practical systems. The automatic controls should be such that the maximum ratings of the light output and the case temperature are not exceeded. "OPERATING CONSIDERATIONS" gives an example of the automatic light output control circuit.

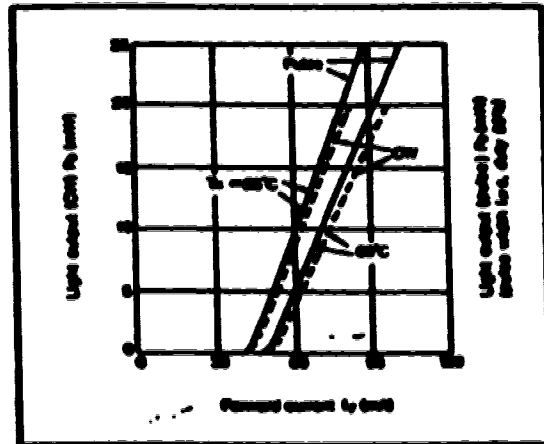


Fig. 1 Light output vs forward current



**MITSUBISHI LASER DIODES**  
**ML6101A, ML6411A**  
**ML6701A**

**FOR OPTICAL INFORMATION SYSTEMS**

**2. Temperature dependence of threshold current ( $I_{th}$ ), operating current ( $I_{op}$ ) and slope efficiency ( $\eta_s$ )**

A typical temperature dependence of the threshold current and the operating current at 10mW are shown in Fig. 2. The characteristic temperature  $T_0$  of the threshold current is typically 100K in  $T_c \leq 85^\circ\text{C}$  where the definition of  $T_0$  is  $I_{th} = \exp(T_c/T_0)$ .

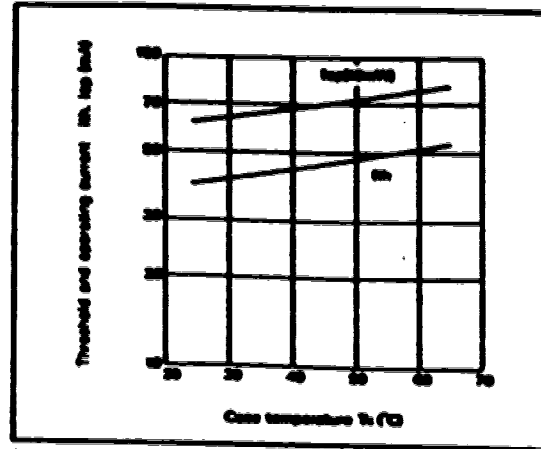


Fig. 2 Temperature dependence of threshold and operating currents

A typical temperature dependence of the slope efficiency  $\eta_s$  is shown in Fig. 3. The gradient is  $-0.002\text{mW/mA}^\circ\text{C}$  typ.

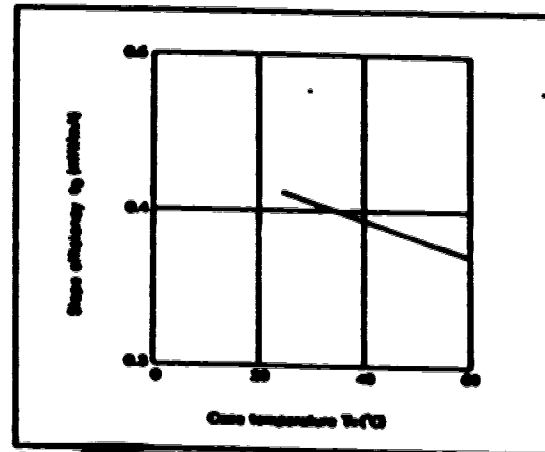


Fig. 3 Temperature dependence of slope efficiency

**3. Forward current vs voltage**

Typical forward current vs voltage characteristics are shown in Fig. 4. In general, as the case temperature rises, the forward voltage  $V_f$  decreases slightly at a constant current  $I_f$ .  $V_f$  varies typically at a rate of  $-20\text{mV}^\circ\text{C}$  at  $I_f = 1\text{mA}$ .

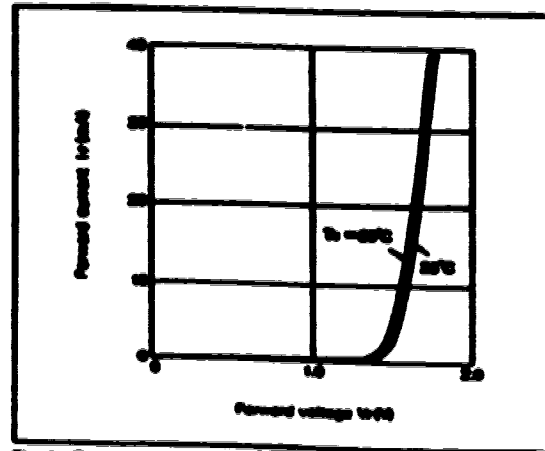


Fig. 4 Forward current vs voltage characteristics

**MITSUBISHI LASER DIODES**  
**MLG101A, MLG411A**  
**MLG701A**

**FOR OPTICAL INFORMATION SYSTEMS**

#### 4. Emission spectra

Typical emission spectra under CW operation are shown in Fig. 5. In general, at an output of 20mW, single mode is observed. The peak wavelength depends on the operating case temperature and the forward current (output level).

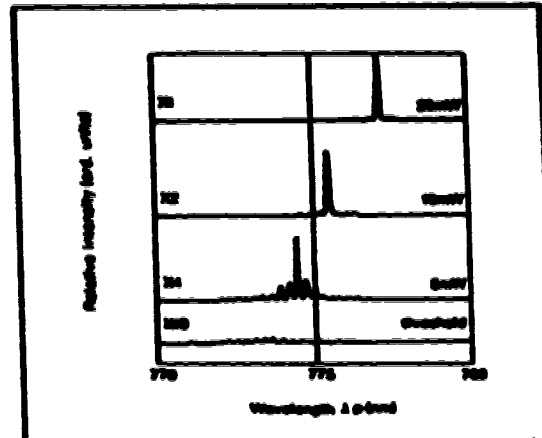


Fig. 5 Emission spectra under CW operating

A typical temperature dependence of the peak wavelength at an output of 10mW is shown in Fig. 6.

The peak wavelength of the beam shifts and jumps to adjacent longitudinal mode by variation of operating temperature. Averaged temperature coefficient which includes the shifts and jumps is about 0.35 nm/°C.

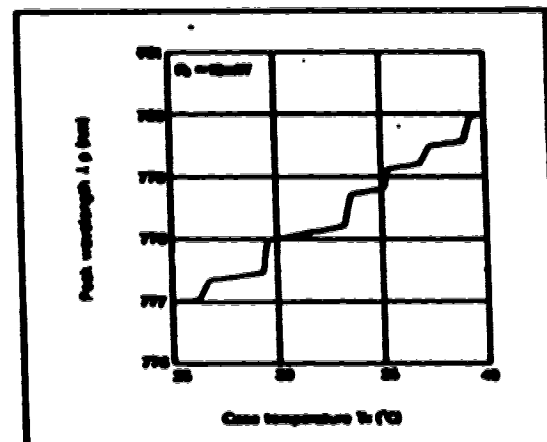


Fig. 6 Temperature dependence of peak wavelength

#### 5. Far-field radiation pattern

The MLG101A, MLG411A, MLG701A laser diodes lase in fundamental (transverse  $TE_{00}$ ) mode and the mode does not change with the current. They have a typical emitting area (size of near-field pattern) of  $0.7 \times 2.5 \mu\text{m}^2$ . Fig. 7 and Fig. 8 show typical far-field radiation patterns in "parallel" and "perpendicular" planes, respectively. The full angles at half maximum points (FWHM) are typically  $12^\circ$  and  $20^\circ$ , respectively.

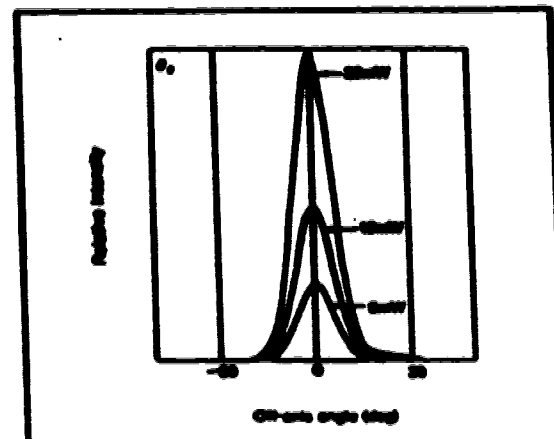


Fig. 7 Far-field patterns in plane parallel to heterojunction

**MITSUBISHI LASER DIODES  
ML6101A, ML6411A  
ML6701A**

**FOR OPTICAL INFORMATION SYSTEMS**

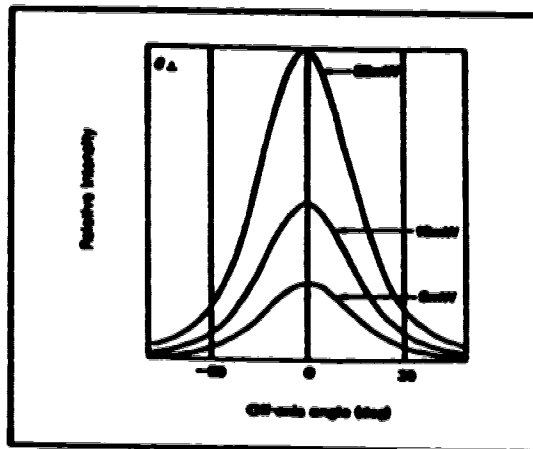


Fig. 8. Far field patterns in plane perpendicular to heterojunctions

**6. Pulse response**

In the digital optical transmission systems, the response waveform and speed of the light output against the input current pulse waveform (shown in Fig. 9) is one of main concerns. The speed depends on the oscillation delay time, rise and fall times. In order to shorten the oscillation delay time, the laser diode is usually biased above the threshold current since the delay time is a function of changing the junction up to the threshold. Fig. 9 shows the typical response waveform when rectangular pulse current is applied.

The rise and fall times are typically 0.2ns and 0.4ns, respectively. They are limited by response speed of the detector.

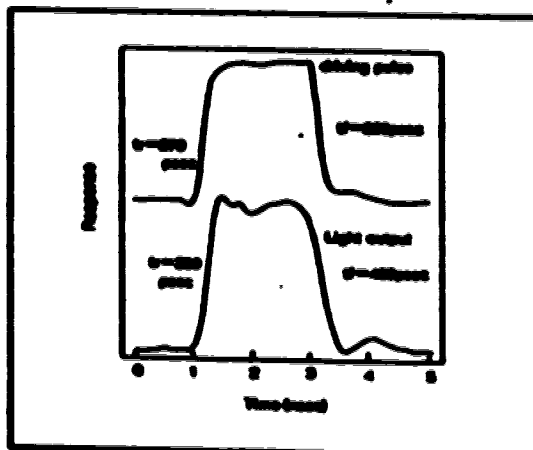


Fig. 9. Pulse response waveform

**7. Monitoring output**

The laser diode emit beams from both of their mirror surfaces, front and rear surfaces (see the outline drawing). The rear beam can be used for monitoring power of front beam since the rear beam is proportional to the front one. In the case of ML6101A, ML6411A, ML6701A lasers, the rear beam powers are changed into photocurrents by the monitoring photodiodes. Fig. 10 shows an example of light output vs monitoring photocurrent characteristics. Above the threshold, the monitored photocurrent linearly increases with the light output.

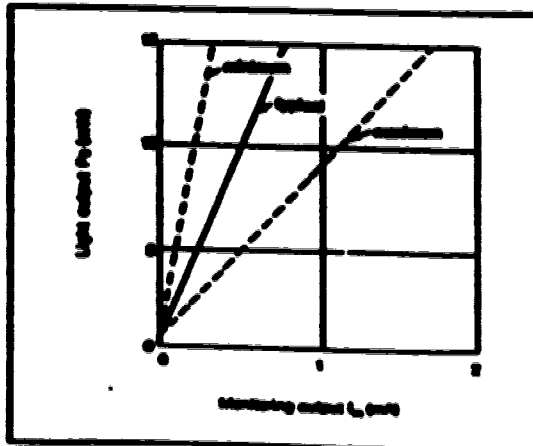


Fig. 10. Light output vs monitoring output current

MITSUBISHI LASER DIODES  
**ML6101A, ML6411A**  
**ML6701A**

FOR OPTICAL INFORMATION SYSTEMS

**8. Polarization ratio**

The polarization ratio ( $P_{\parallel}/P_{\perp}$ ), which is the ratio of the parallel polarized light output and the perpendicular polarized one, vs. total light output characteristics is shown in Fig. 11. The polarization ratio linearly increases with the light power.

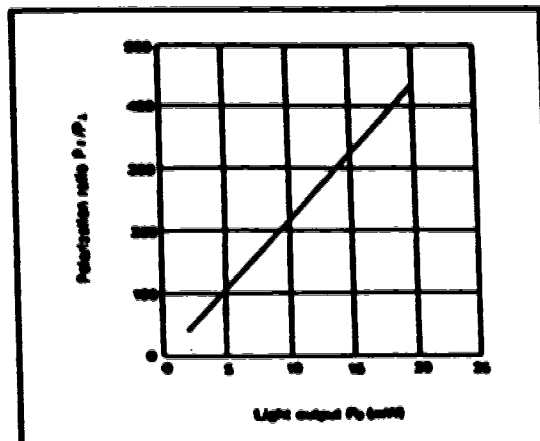


Fig. 11 Polarization ratio vs light output

**9. Impedance characteristics**

Typical impedance characteristics of the ML6101A, ML6411A, ML6701A lasers, with lead lengths of 2mm, is shown in Fig. 12 with the bias currents as the parameter. Test frequency is swept from 100MHz to 1000MHz with 100MHz step. Above the threshold, the impedance can be approximated by a series connection of a resistance of 3 ohm and an inductance of 2nH.

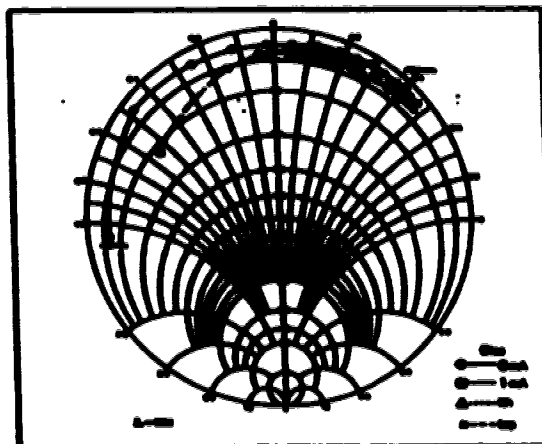


Fig. 12 Impedance characteristics

**10. S/N vs optical feedback ratio**

The signal to noise (S/N) of the laser beam is defined as the SC to noise electric power ratio after changing the laser beam to electric signal. Therefore, the defined S/N corresponds to square of the SC-to-noise optical power ratio.

Fig. 13 shows the S/N vs the optical feedback at the frequency of 10MHz and with the bandwidth of 200kHz.

Fig. 14 shows similar characteristics at a low frequency, 20MHz, and with the bandwidth of 200kHz.

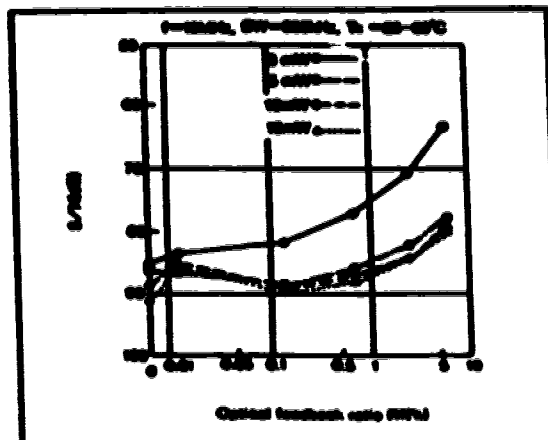


Fig. 13 S/N vs optical feedback ratio

MITSUBISHI LASER DIODES  
**ML6101A, ML6411A**  
**ML6701A**

FOR OPTICAL INFORMATION SYSTEMS

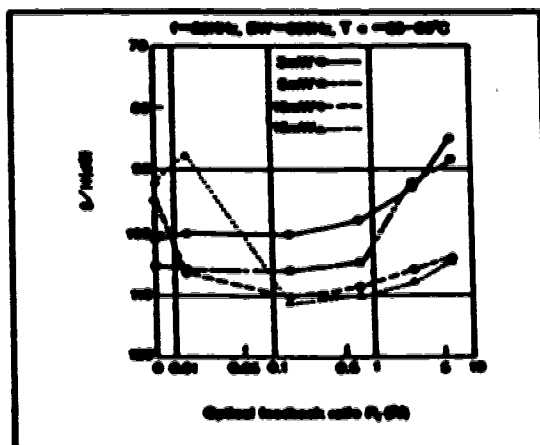


Fig. 10 S/N vs optical feedback ratio

# **C**omponents

**Fiber Optic Couplers  
Transmissive Star  
Type PCS MxN  
Multi-Mode**



Center fiber optic transmissive star couplers are designed for use in optical local area networks, industrial control, data acquisition and data dissemination systems. Standard couplers are available in any input/output configuration up to 64 x 64 ports. Optimum performance and reliability under adverse environmental conditions is achieved through a proprietary refinement of the fused biconical taper technique combined with tight quality control and testing.

The PCS 3x4 model is the preferred solution for applications requiring secure assembly and/or handling features.

#### **■ Features**

- Compact rugged package
- Completely non-metallic
- FC based or chassis mountable
- Bi-directional
- Low insertion loss
- High durability
- Uniform outputs
- Shielded input fibers
- Jacketed or bare fiber pigtail
- Optional connectorized pigtail
- Optional rack or table top enclosure with connector.



Canstar fiber optic couplers are passive devices usable at wavelengths between 400nm and 1600nm. Engineered to withstand industrial environments, the devices are enclosed in a flame resistant rugged housing. A variety of connectors and enclosures can be provided.

**Typical Characteristics**

**General:**

Temperature: - 55°C to +85°C  
 Humidity: to 95% @ +55°C

**Jacketing:**

- Up to 12x12 parts - 3mm PU reinforced jacketing
- Up to 20x20 parts - 0.5mm TFE buffer tube
- Over 20x20 parts - 250 micron coated fiber

**Fiber:**

Core	0.8 (um)	N.A.
80	125	0.200
62.5	125	0.275
65	125	0.200
100	140	0.200

Other fiber types are available on a custom basis.

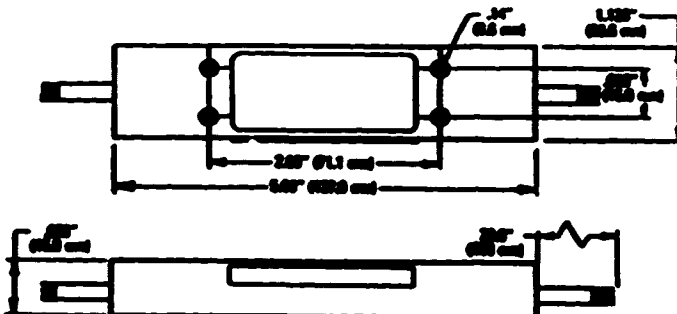
**Performance Specifications:**

Type	Maximum Insertion Loss Port to Port (dB)
FCS 3x3	0.0
FCS 4x4	0.0
FCS 6x6	0.5
FCS 8x8	1.0
FCS 12x12	13.0
FCS 16x16	15.0
FCS 22x22	16.0
FCS 34x34	23.0

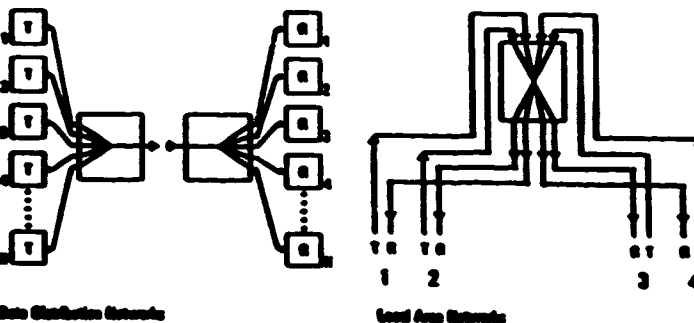
Characteristics of other types available upon request.

Note: 20x20 is a custom product in 0.5mm fiber.

**Dimensions**



**Applications**

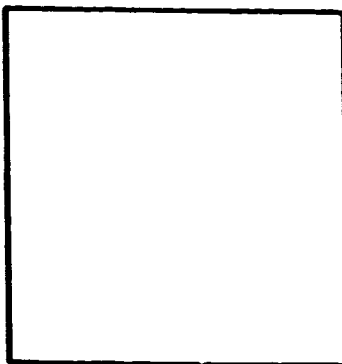


**Ordering Information**

- Specify:**
- Type FCS
  - No. of input and output ports
  - Fiber core size

**Example:**  
 FCS 16x16-100  
 A variety of connectors can be factory installed.

**Distributed by**



Head Office Toronto  
 2800 Victoria Park Ave.  
 North York, Ontario  
 M2H 3P7 Canada  
 Phone: 416-293-0100  
 Fax: 416-293-0500  
 Telex: 010-01-010



U.S.A. Plant  
 5 Wakeup Drive  
 Wakeborough, MA 01081  
 U.S.A.  
 Phone: 617-693-0400  
 Fax: 617-693-7000

CANSTAR  
5 Mainup Drive  
Westborough, MA 01581

MODEL NO FCB-1X10-30  
SN 103201

	2	4	6	8	10	12	14	16	18	20
1	11.0	11.0	10.9	11.3	11.0	11.2	11.2	11.2	11.1	11.2

MIN 10.9  
MAX 11.3  
RANGE 0.3

CANSTAR  
5 Mainup Drive  
Westborough, MA 01581

MODEL NO FCB-1X10-30  
SN 103202

	2	4	6	8	10	12	14	16	18	20
1	10.9	10.8	10.4	10.5	10.8	11.0	10.8	11.0	10.6	11.0

MIN 10.4  
MAX 11.0  
RANGE 0.6

CANSTAR  
5 Mainup Drive  
Westborough, MA 01581

MODEL NO FCB-1X10-30  
SN 103203

	2	4	6	8	10	12	14	16	18	20
1	10.6	10.8	10.9	10.7	10.8	10.7	10.8	10.6	10.8	10.6

MIN 10.6  
MAX 10.9  
RANGE 0.3

CANSTAR  
5 Mainup Drive  
Westborough, MA 01581

MODEL NO FCB-1X10-30  
SN 103204

	2	4	6	8	10	12	14	16	18	20
1	10.8	11.0	11.1	10.9	11.1	10.7	10.8	10.7	10.7	11.0

MIN 10.7  
MAX 11.1  
RANGE 0.4

CANSTAR  
5 Mainup Drive  
Westborough, MA 01581

MODEL NO FCB-1X10-30  
SN 103205

	2	4	6	8	10	12	14	16	18	20
1	11.2	11.3	11.3	11.2	11.1	11.1	11.3	11.2	11.2	11.2

MIN 11.1  
MAX 11.3  
RANGE 0.2



CANSTAR  
5 Mainup Drive  
Westborough, MA 01581

MODEL NO FCB-1X10-80  
SN 103206

	2	4	6	8	10	12	14	16	18	20
1	11.3	11.6	11.4	11.4	11.6	11.4	11.4	11.6	11.6	11.3

MIN 11.3  
MAX 11.6  
RANGE 0.3

CANSTAR  
5 Mainup Drive  
Westborough, MA 01581

MODEL NO FCB-1X10-80  
SN 103207

	2	4	6	8	10	12	14	16	18	20
1	11.3	11.2	11.3	11.7	11.2	11.6	11.4	11.4	11.4	11.3

MIN 11.2  
MAX 11.7  
RANGE 0.5

CANSTAR  
5 Mainup Drive  
Westborough, MA 01581

MODEL NO FCB-1X10-80  
SN 103208

	2	4	6	8	10	12	14	16	18	20
1	11.1	10.6	10.9	10.8	11.0	10.7	10.9	10.6	10.7	10.8

MIN 10.6  
MAX 11.1  
RANGE 0.5

CANSTAR  
5 Mainup Drive  
Westborough, MA 01581

MODEL NO FCB-1X10-80  
SN 103209

	2	4	6	8	10	12	14	16	18	20
1	10.3	10.6	10.7	10.8	10.5	10.7	11.0	10.9	10.7	10.5

MIN 10.5  
MAX 11.0  
RANGE 0.5

CANSTAR  
5 Mainup Drive  
Westborough, MA 01581

MODEL NO FCB-1X10-80  
SN 103210

	2	4	6	8	10	12	14	16	18	20
1	11.1	10.9	11.0	10.9	11.1	11.0	11.0	11.2	11.0	10.8

MIN 10.8  
MAX 11.2  
RANGE 0.3



**MSA-6335 MODAMP™ Cascodeable Silicon Bipolar Monolithic Microwave Integrated Circuit Amplifiers**

**Absolute Maximum Ratings**

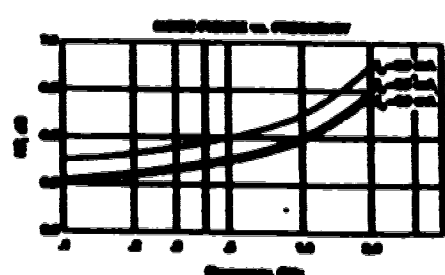
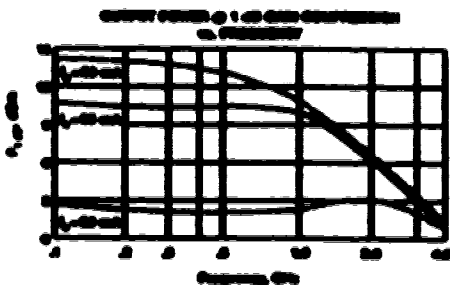
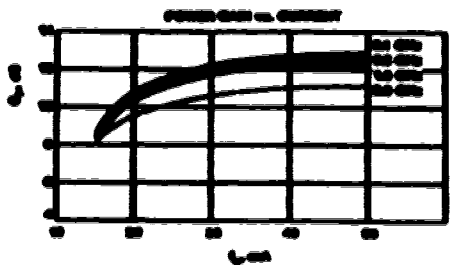
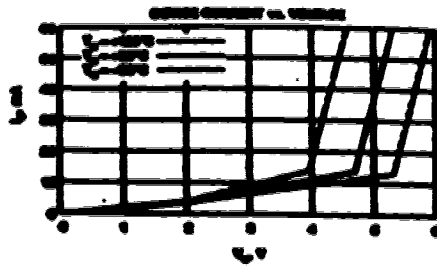
Parameter	Absolute Maximum
Output Current	60 mA
Power Dissipation	400 mW
DC Input Power	100 mW
Junction Temperature	200 °C
Storage Temperature	200 °C

Typical Package  $\theta_{JA} = 67^\circ\text{C/W}$

**Notes:**

1. Forward damage may occur if any of these limits are exceeded.
2. Limits at 100 MHz for  $T_A = 25^\circ\text{C}$ .
3. Storage above  $200^\circ\text{C}$  may require the back of this package cooling to allow for safe storage.

**Typical Performance,  $T_A = 25^\circ\text{C}$**   
(unless otherwise noted)



**Typical Scattering Parameters:  $Z_0 = 50\Omega$**

$T_A = 25^\circ\text{C}$ ,  $I_D = 65\text{ mA}$

f (GHz)	$S_{11}$		$S_{21}$		$S_{12}$		$S_{22}$	
	dB	deg	dB	deg	dB	deg	dB	deg
0.1	-26	177	18.6	4.58	-18.6	178	-17	-4
0.2	-24	181	18.5	4.58	-18.5	180	-17	-4
0.5	-24	183	18.2	4.58	-18.2	180	-17	-4
1.0	-23	184	17.1	4.62	-17.1	180	-16	-4
1.5	-23	184	15.6	4.70	-15.6	180	-15	-4
2.0	-23	185	13.6	4.78	-13.6	180	-14	-4
3.0	-21	187	10.8	4.91	-10.8	180	-13	-4
5.0	-19	190	7.3	5.05	-7.3	180	-12	-4
10.0	-17	193	4.6	5.28	-4.6	180	-11	-4
20.0	-15	197	2.5	5.58	-2.5	180	-10	-4



**MSA-0435**  
**MODAMP™ Crossover Silicon Bipolar**  
**Monolithic Microwave Integrated**  
**Circuit Amplifier**

**Features**

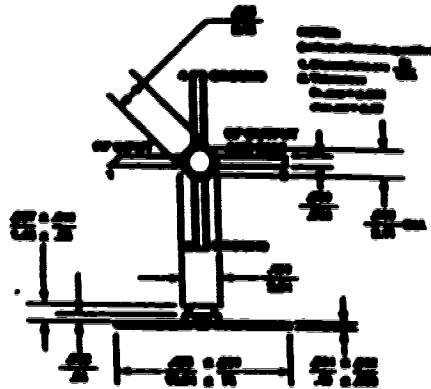
- Crossover 500 Gain Block
- 3 dB Bandwidth: 0.5 to 2.5 GHz
- 12.5 dBm typical  $P_{1dB}$  @ 1.0 GHz
- 0.5 dB typical Gain at 1.0 GHz
- Unusually Stable ( $\lambda > 3$ )
- Glass-coat Ceramic Mounting Package

**Description**

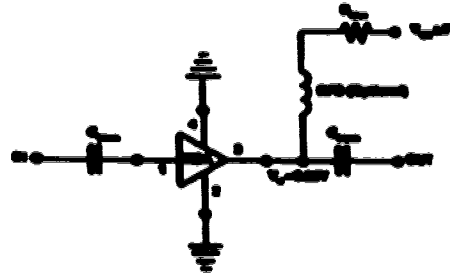
Avantek's MSA-0435 is a high performance silicon bipolar Monolithic Microwave Integrated Circuit (MMIC) housed in a cost effective, ceramic package. This MODAMP™ MMIC is designed for use as a general purpose 50 ohm gain block. Typical applications include narrow and broad band RF and IF amplifiers in industrial and military applications.

Excellent device uniformity and performance are produced by the ion implantation and self-alignment techniques used in the fabrication of these devices.

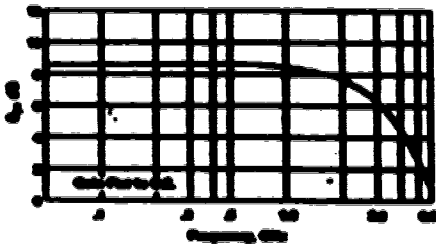
**Avantek micro-K Package**



**Typical Biasing Configuration**



**TYPICAL POWER GAIN vs. FREQUENCY**  
 $T_A = 25^\circ\text{C}$ ,  $I_C = 50 \text{ mA}$



**Electrical Specifications,  $T_A = 25^\circ\text{C}$**

Symbol	Parameter/Test Conditions ( $I_C = 50 \text{ mA}$ , $Z_L = 50\Omega$ )	Units	Min.	Typ.	Max.
$G_p$	Power Gain ( $S_{21}$ )	dB	12.0	12.5	13.0
$GB$	Gain Bandwidth	GHz	0.5		2.5
$GB$	3 dB Bandwidth	GHz		0.5	
VSWR	Input VSWR			1.5	
	Output VSWR			1.5	
$P_{1dB}$	Output Power @ 1 dB Gain Compression	dBm	12.5		
OP	OSR Noise Figure	dB	0.5		
$C_r$	Third Order Intercept Point	dBm	20		
$t_r$	Group Delay	ps	10		
$V_C$	Collector Voltage	V	4.5	5.0	5.5
$\alpha_{VT}$	Collector Voltage Temperature Coefficient	$^\circ\text{C}^{-1}$		-0.5	

The recommended operating conditions for this device is 0°C to 70°C. Typical performance is a function of manufacturing process and lot-to-lot variation.

**MSA-035 MODAM™ Cascadable Silicon Bipolar Monolithic Microwave Integrated Circuit Amplifiers**

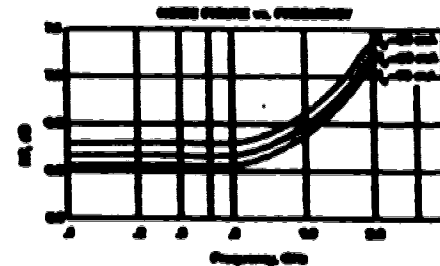
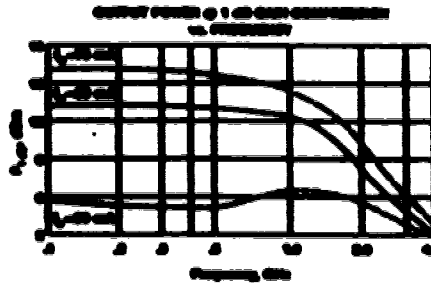
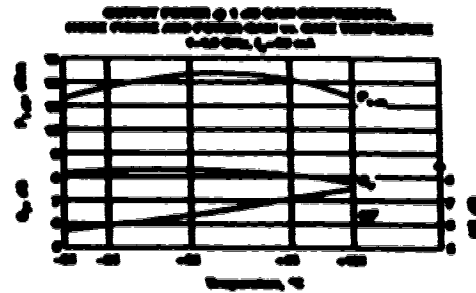
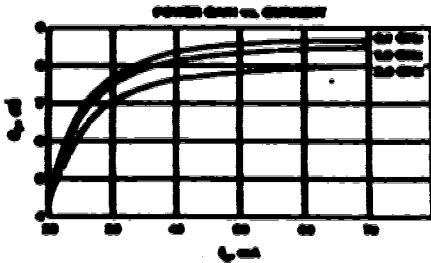
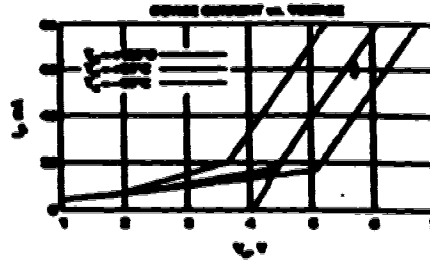
**Absolute Maximum Ratings**

Parameter	Absolute Maximum
Output Current	100 mA
Power Dissipation	600 mW
RF Input Power	+20 dBm
Junction Temperature	200°C
Storage Temperature	200°C

Thermal Resistance  $\theta_{j-c} = 10^\circ\text{C/W}$

- Notes:  
 1. Permanent damage may occur if any of these limits are exceeded.  
 2. Grade of 20 mW for  $T_A > 100^\circ\text{C}$ .  
 3. Storage above  $100^\circ\text{C}$  only within the limits of this package rating if allowed to enter into a shock.

**Typical Performance,  $T_A = 25^\circ\text{C}$**   
(unless otherwise noted)



**Typical Scattering Parameters,  $Z_0 = 50\Omega$**

$T_A = 25^\circ\text{C}$ ,  $I_o = 50\text{ mA}$

$f_{RF}$ GHz	$S_{11}$		$S_{21}$			$S_{12}$			$S_{22}$	
	Mag	Ang	Mag	Mag	Ang	Mag	Mag	Ang	Mag	Ang
0.1	.20	195	0.8	2.07	195	-0.4	.101	1	.20	-195
0.2	.20	192	0.8	2.09	194	-0.4	.101	2	.20	-195
0.5	.27	191	0.8	2.07	194	-0.4	.101	5	.20	-195
0.8	.27	190	0.8	2.08	194	-0.4	.101	6	.20	-195
1.0	.28	190	0.8	2.04	193	-0.4	.101	10	.20	-195
1.5	.34	-192	0.7	2.05	193	-0.4	.101	15	.20	-195
2.0	.39	-195	0.6	2.06	97	-0.4	.101	20	.20	-195
3.0	.51	-193	0.6	2.09	71	-0.4	.101	25	.20	-195
4.0	.58	-195	0.6	2.14	55	-0.4	.101	30	.20	-195
6.0	.70	-195	0.6	1.94	35	-0.4	.101	40	.20	-195
8.0	.77	-195	0.6	1.87	-1	-0.4	.101	50	.20	-195
10.0	.82	-195	0.6	1.81	-15	-0.4	.101	60	.20	-195



**01A-03170**  
**MagC™ Low Noise, Cancellable**  
**Silicon Bipolar MMIC Amplifier**  
 September, 1999

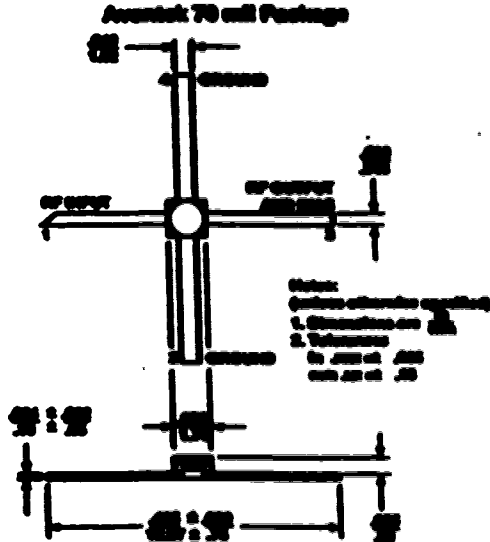
**Features**

- Cancellable 50 Ω Gain Block
- Low Noise Figure: 2.5 dB typical at 1.5 GHz
- High Gain: 25.0 dB typical at 1.5 GHz
- 3 dB Bandwidth: 50 to 2.5 GHz
- Unconditionally Stable (S>1)
- Low Power Dissipation
- Hermetic Gold-Ceramic Surface Mount Package

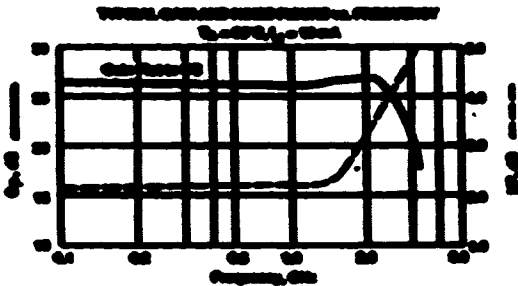
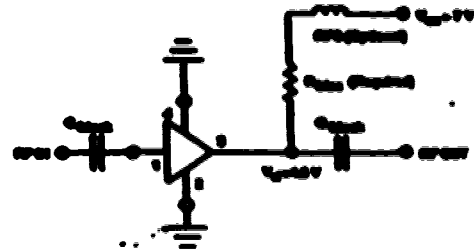
**Description**

Avantek's 01A-03170 is a low noise silicon bipolar Monolithic Microwave Integrated Circuit (MMIC) feedback amplifier housed in a hermetic, high reliability package. It is designed for narrow or wide bandwidth commercial, industrial and military applications that require high gain and low noise IP or OP amplification with minimum power consumption.

The MMIC core of 01A-03170 is fabricated using Avantek's 10 GHz (1.5B-GHz) SiGe™ silicon bipolar process with on-chip self-alignment, submicrometer lithography, trench isolation, low-impedance, gold metallization and polyimide inter-metal dielectrics and ceramic passivation to achieve excellent performance, uniformity and reliability.



**Typical Biasing Configuration**



**Electrical Specifications<sup>1</sup>, T<sub>a</sub> = 25°C**

Symbol	Parameter and Test Conditions (V <sub>CC</sub> = 5.0V, Z <sub>0</sub> = 50 Ω)	Min	Typ	Max	Units
S <sub>11</sub>	Input Reflection Coefficient	-1.0	-1.0	-1.0	dB
S <sub>22</sub>	Output Reflection Coefficient	-1.0	-1.0	-1.0	dB
S <sub>12</sub>	Reverse Isolation	-1.0	-1.0	-1.0	dB
S <sub>21</sub>	Forward Isolation	-1.0	-1.0	-1.0	dB
Gain	Gain	24.0	25.0	26.0	dB
NF	Noise Figure	2.5	2.5	2.5	dB
IP3	Third-Order Intercept Point	10	10	10	dBm
OP3	Third-Order Intercept Point	10	10	10	dBm
IP1dB	1 dB Compression Point	10	10	10	dBm
OP1dB	1 dB Compression Point	10	10	10	dBm
IP3dB	3 dB Compression Point	10	10	10	dBm
OP3dB	3 dB Compression Point	10	10	10	dBm

<sup>1</sup> Values are typical unless otherwise specified.  
<sup>2</sup> Values are typical unless otherwise specified.  
<sup>3</sup> Values are typical unless otherwise specified.

**MA-63170 Low Noise, Cascadable Silicon Bipolar MMIC Amplifier**

**Absolute Maximum Ratings**

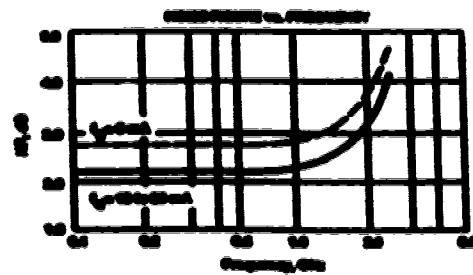
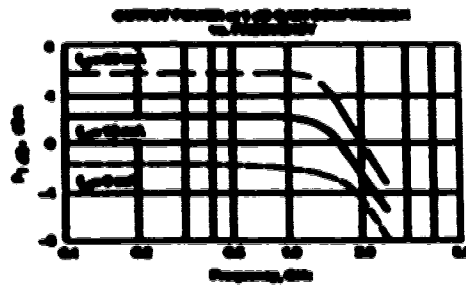
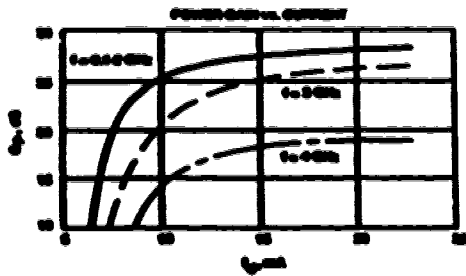
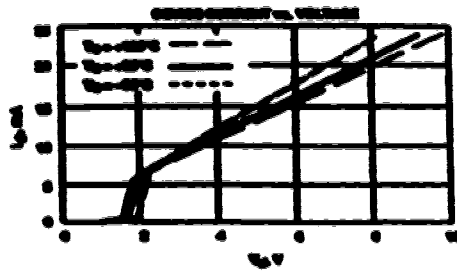
Parameter	Absolute Maximum
Output Current	25 mA
Power Dissipation <sup>1</sup>	200 mW
RF Input Power	+10 dBm
Storage Temperature	200°C
Range Temperature	-40°C to 200°C

<sup>1</sup>Maximum Value at  $T_C = 100^\circ\text{C}$

**Notes:**

1. Permanent damage may occur if any of these limits are exceeded.
2.  $T_{\text{case}} = 25^\circ\text{C}$
3. Derate at 0.7 mW/°C for  $T_C > 175^\circ\text{C}$ .

**Typical Performance,  $T_A = 25^\circ\text{C}$**   
(unless otherwise noted)



**Typical Scattering Parameters:  $Z_0 = 50 \Omega$**

GHz	$S_{11}$			$S_{22}$			$S_{21}$			$S_{12}$			dB
	Mag	Phase	Mag	Mag	Phase	Mag	Mag	Phase	Mag	Phase	Mag		
0.1	0.05	-180	0.05	0.05	-180	0.95	0.05	-180	0.05	-180	0.05	20	
0.2	0.05	-180	0.05	0.05	-180	0.95	0.05	-180	0.05	-180	0.05	20	
0.3	0.05	-180	0.05	0.05	-180	0.95	0.05	-180	0.05	-180	0.05	20	
0.4	0.05	-180	0.05	0.05	-180	0.95	0.05	-180	0.05	-180	0.05	20	
0.5	0.05	-180	0.05	0.05	-180	0.95	0.05	-180	0.05	-180	0.05	20	
0.6	0.05	-180	0.05	0.05	-180	0.95	0.05	-180	0.05	-180	0.05	20	
0.7	0.05	-180	0.05	0.05	-180	0.95	0.05	-180	0.05	-180	0.05	20	
0.8	0.05	-180	0.05	0.05	-180	0.95	0.05	-180	0.05	-180	0.05	20	
0.9	0.05	-180	0.05	0.05	-180	0.95	0.05	-180	0.05	-180	0.05	20	
1.0	0.05	-180	0.05	0.05	-180	0.95	0.05	-180	0.05	-180	0.05	20	
1.2	0.05	-180	0.05	0.05	-180	0.95	0.05	-180	0.05	-180	0.05	20	
1.4	0.05	-180	0.05	0.05	-180	0.95	0.05	-180	0.05	-180	0.05	20	
1.6	0.05	-180	0.05	0.05	-180	0.95	0.05	-180	0.05	-180	0.05	20	
1.8	0.05	-180	0.05	0.05	-180	0.95	0.05	-180	0.05	-180	0.05	20	
2.0	0.05	-180	0.05	0.05	-180	0.95	0.05	-180	0.05	-180	0.05	20	



3075 Stevens Avenue  
 Santa Clara, CA 95050-6022  
 (408) 253-6100  
 FAX: 408-253-6177; Cable: Avantek  
 Copyright © 1994